1-1-2014

Surface Plasmon Based Engineering of Semiconductor Nanowire Optics

Carlos Octavio Aspetti
University of Pennsylvania, carlos.aspetti@gmail.com

Surface Plasmon Based Engineering of Semiconductor Nanowire Optics

Abstract
Semiconductor nanowires combine the material properties of semiconductors, which are ubiquitous in modern technology, with nanoscale dimensions and as such, are firmly poised at the forefront of nanotechnology research. The rich physics of semiconductor nanowire optics, in particular, arises from the increased interaction between light and matter that occurs when light is confined to dimensions below the size of its wavelength, in other words, when the nanowire serves as a light trapping optical cavity, which itself is also a source of light. Light confinement is taken to new extremes by coupling to the surface plasmon modes of metallic nanostructures, where light acquires mixed photonic and electronic character, and which may focus light to deep-subwavelength regions amenable to the dimensions of the electron wave. This thesis examines how the integration of "plasmonic optical cavities" and semiconductor nanowires leads to substantial modification (and enhancement) of the optical properties of the same, resulting in orders-of-magnitude faster and more efficient light emission with colors that may be tuned as a function of optical cavity geometry. Furthermore, this method is applied to nanowires composed of both direct and indirect bandgap semiconductor materials resulting in applications such as light emission from high-energy states in light emitting materials, highly enhanced broadband light emission from nominally non-light emitting (dark) materials, and broadband (and anomalous) enhancement of light absorption in various materials, all the while maintaining the unifying theme of employing integrated plasmonic-semiconductor optical cavities to achieve tailored optical properties. We begin with a review of the electromagnetic properties of optical cavities, surface plasmon-enhanced light emission in semiconductors, and the key physical properties of semiconductor nanowires. It goes without saying that this thesis work resides at the interface between optical physics and materials science.

Degree Type
Dissertation

Degree Name
Doctor of Philosophy (PhD)

Graduate Group
Materials Science & Engineering

First Advisor
Ritesh Agarwal

Keywords
light-matter interaction, photonics, photon management, plasmonics, Purcell effect, semiconductors

Subject Categories
Mechanics of Materials | Optics | Physics

SURFACE PLASMON BASED ENGINEERING OF SEMICONDUCTOR NANOWIRE OPTICS

Carlos Octavio Aspetti

A DISSERTATION

in

Materials Science and Engineering

Presented to the Faculties of the University of Pennsylvania

in

Partial Fulfillment of the Requirements for the

Degree of Doctor of Philosophy

2014

Supervisor of Dissertation

_____

Ritesh Agarwal, PhD
Professor of Materials Science and Engineering

Graduate Group Chairperson

_____

Shu Yang, PhD, Professor of Materials Science and Engineering

Dissertation Committee

Russell Composto, PhD, Professor of Materials Science and Engineering

Nader Engheta, PhD, H. Nedwill Ramsey Professor of Electrical and Systems Engineering, Bioengineering, and Physics and Astronomy

Ertugrul Cubukcu, PhD, Assistant Professor of Materials Science and Engineering

SURFACE PLASMON BASED ENGINEERING OF SEMICONDUCTOR

NANOWIRE OPTICS

My dreams, now realized, are carved on the many sacrifices made by my mother and father, Nelly Aspetti and Herman Aspetti. This is for them.

ACKNOWLEDGEMENTS

I would like to thank the members (past and present) of the Agarwal group who have made these past five years, a transformative experience. My early mentors, Dr. Chang-Hee Cho, Dr. Lambert van Vugt and Dr. Brian Piccione, aided my study of optics while Dr. Sung-Wook Nam introduced me to microfabrication techniques. My many scientific discussions with Pavan Nukala (master of all) were invaluable. Rahul Agarwal and Pavan also provided top quality insight and support in materials characterization. I must also thank Jacob Berger, Joohee Park, Daksh Agarwal, Wenjing Liu, and Karthik Kumar whose capacity for research and success in the lab has been a constant source of inspiration. Dr. Moon-Hyung Jang, Dr. Bumsu Lee, Dr. Liaoxin Sun, Dr. Ming-Liang Ren, Dr. Sajal Dhara, and Dr. Chris Rodd have also provided valuable support in a variety of topics. Last, and certainly not least, I thank my advisor, Prof. Ritesh Agarwal, for believing that I could do this. He treated me as a colleague since day one and I have been hard pressed to find a more potent source of motivation. Everyone had the patience to field my never-ending questions with a smile. Thank you.

I must also thank my PhD cohort, Kate Murphy, Michael O'Reilly, Lisa Chen, Vicky Doan-Nguyen, Pavan Nukala, and Robert Ferrier who were all a constant source of support. Thank you Robert for a decade of camaraderie as we survived the first-ever Physics/Materials Science BS/MS program at Drexel, a PhD program at Penn, and the many trials and tribulations therein. You are my colleague, my friend, and I will not forget you. There are undoubtedly many others who aided in the production of this document and whom I have not named here for the sake of brevity. Know that you are in my thoughts.

ABSTRACT

SURFACE PLASMON BASED ENGINEERING OF SEMICONDUCTOR NANOWIRE OPTICS

Carlos Octavio Aspetti

Ritesh Agarwal, PhD

Semiconductor nanowires combine the material properties of semiconductors, which are ubiquitous in modern technology, with nanoscale dimensions and as such, are firmly poised at the forefront of nanotechnology research. The rich physics of semiconductor nanowire optics, in particular, arises from the increased interaction between light and matter that occurs when light is confined to dimensions below the size of its wavelength, in other words, when the nanowire serves as a light trapping optical cavity, which itself is also a source of light. Light confinement is taken to new extremes by coupling to the surface plasmon modes of metallic nanostructures, where light acquires mixed photonic and electronic character, and which may focus light to deep-subwavelength regions amenable to the dimensions of the electron wave. This thesis examines how the integration of "plasmonic optical cavities" and semiconductor nanowires leads to substantial modification (and enhancement) of the optical properties of the same, resulting in orders-of-magnitude faster and more efficient light emission with colors that may be tuned as a function of optical cavity geometry. Furthermore, this method is applied to nanowires composed of both direct and indirect bandgap semiconductor materials resulting in applications such as light emission from high-energy states in light emitting materials, highly enhanced broadband light emission from nominally non-light

emitting (dark) materials, and broadband (and anomalous) enhancement of light absorption in various materials, all the while maintaining the unifying theme of employing integrated plasmonic-semiconductor optical cavities to achieve tailored optical properties. We begin with a review of the electromagnetic properties of optical cavities, surface plasmon-enhanced light emission in semiconductors, and the key physical properties of semiconductor nanowires. It goes without saying that this thesis work resides at the interface between optical physics and materials science.

TABLE OF CONTENTS

LIST OF ILLUSTRATIONS

diameter demonstrating lasing in plasmonically-coupled CdS below the photonic lasing cutoff. d) Purcell enhancement for plasmonically-coupled CdS. [Adapted from Reference 30].

Figure 2.1 | Schematic of VLS process described in three steps. a) Precursor (PC) comes into contact with catalyst particle above the eutectic temperature. b) Fictitious binary phase diagram demonstrating supersaturation of catalyst with time. c) Solid precursor is precipitated at the catalyst-substrate interface leading to vertical nanowire growth.

Figure 2.2 | a) SEM micrograph of nanowire growth substrate (1 micron scale bar), (inset: tip of nanowire and catalyst particle, 100 nm scale bar). b) SEM micrograph of individual nanowire on substrate used for optical measurement. c) X-ray diffraction data for CdS nanowire growth substrate in (a).

Figure 2.3 | a) Schematic of experimental setup involving pumping of CdS nanowire above the band-gap and both body and end-emission. b) Optical image of nanowire on measurement substrate. c) Same nanowire as (a) under laser excitation.

Figure 2.4 | Optical and morphological properties of VLS grown CdS nanowires. a) Photoluminescence spectrum of unpassivated CdS nanowire (red curve) and SiO_2-passivated CdS nanowire (blue curve). b) Transmission electron microscope micrograph of CdS nanowire coated with 5 nm of SiO_2 (top panel) and FTIR spectrum of uncoated CdS nanowire (bottom panel, black curve) and passivated nanowire (bottom panel, blue curve).

Figure 3.1 | Schematic of E vs. k dispersion relation for an exciton in CdS, depicting the exciton generation, relaxation, and emission process (dark blue curve). E_L denotes the laser excitation energy.

Figure 3.2 | Characterization of core-shell; CdS-SiO_2-Ag nanowire. a) Schematic of core-shell structure. b) TEM micrograph of ALD deposited SiO_2 passivation layer. c) TEM micrograph of 15 nm polycrystalline Ag coating. d) EDX elemental maps demonstrating conformal coatings of all species.

Figure 3.3 | a) Photoluminescence measurements at 77 K for metal-coated (magenta) and bare (blue) nanowires. b) Photoluminescence for metal-coated nanowires with different core diameters (legend: core nanowire diameter).

Figure 3.4 | Comparison between photoluminescence spectra of bare and passivated CdS nanowire (blue curve) and metal-coated CdS nanowire (red curve), both with diameter, d=60 nm. In order to provide a fair comparison of the photoluminescence intensities, we take into account both in-coupling and out-coupling through the thin silver film with respect to the bare nanowire. These were calculated to be 280% (enhancement) of the in-coupling and 5% (reduction) in out-coupling using Lumerical, a commercial Finite Difference Time Domain solver. Overall, a significant (~10x) increase in photon counts is observed for the metal-coated nanowire. The in-coupling enhancement is due to antenna effects whereas the decrease in out-coupling is due to ohmic losses.

Figure 3.5 | a) Schematic of exciton generation, relaxation, and emission process for a thermalized exciton (blue curve, left) and non-thermalized (hot)-exciton (green curve, right) in CdS. E_L denotes the laser excitation energy. b) Photoluminescence spectra associated with the diagram in (a) (also plotted in figure 3.4) and following the same color code for a bare CdS nanowire (blue curve, bottom) and plasmonic-core shell CdS nanowire (green curve, top). The bare CdS nanowire shows emission from thermalized excitons while the metal-coated CdS nanowire cavity shows emission peaks corresponding to non-thermalized (hot) excitons.

Figure 3.6 | Polarization dependence of the photoluminescence intensity as function of angle, θ, from nanowire long-axis, taken by placing a linear polarizer in front of the spectrometer for a) bare nanowire and b) metal-coated nanowire. From the polarization of the A-exciton in figure 3.6a (which is polarized perpendicular to the c-axis of CdS) it is determined that this batch of nanowires is grown with c-axis ~55° (dashed line at bottom of polar plots) from the nanowire long axis (horizontal purple line at bottom of polar plots).

Figure 3.7 | Schematic of naming convention for semiconductor nanowire electromagnetic modes. The black arrows correspond to the electric field polarization with reference to the nanowire below (colored red).

Figure 3.8 | Calculated magnetic field intensity at 2.556 eV (4-LO hot excition/B-exciton energy) for a) d=140 nm plasmonically-coupled nanowire and b) d=140 nm bare nanowire. No electromagnetic mode is observed in the bare nanowire in this energy range. White lines denote material boundaries.

Figure 3.9 | Size-dependent photoluminescence spectra and simulation from plasmonically-coupled core-shell CdS nanowires. a) Size-dependent enhancement of 4-LO hot photoluminescence peak (open circles) and calculated field intensity per unit area (red curve) as a function of nanowire diameter. b-d) Simulated magnetic field (H^2) and electric field (E^2) intensity profiles, as a function of nanowire diameter for three resonant sizes b) *d*=60 nm (azimuthal mode number, m=2) c) *d*=100 nm (m=3), and d) *d*=135 nm (m=4).

Figure 3.10 | a) Time resolved PL spectral map from ensemble of 300-500 nanowires with average diameter 140 ± 50 nm at room temperature (300 K). b) Time-resolved integrated emission intensity for plasmonic (upper) and photonic (lower) nanowires. Solid lines are an exponential fit to the data. Resulting radiative recombination lifetimes of 7 ps and 1600 ps for plasmonically-coupled and bare nanowires respectively are included next to the fitted curves.

Figure 3.11 | Experimentally obtained refractive index values for a) CdSe and b) Ge. The real part of the refractive index (blue curves) and imaginary part (magenta curves) are listed for the wavelength range over which absorption spectra were computed.

Figure 3.12 | Enhanced absorption with anomalous polarization dependence (with respect to a bare CdSe nanowire) in a plasmonically-coupled CdSe nanowire. a, b) Absorption

to dimensions that are resonant with the cavity modes (blue curve). The high efficiency emission channels are labeled A, B, and C from high to low energy. b) Size-dependent photoluminescence spectra of Ω-cavity Si. The white dash lines represent selected off-resonance simulated cavity spectra taken from (c). The yellow dash lines represent resonant simulated cavity spectra corresponding to the experimentally measured size (d=70 and d=55 nm) and are also plotted in (c). c) Simulated spectra of cavity modes at various nanowire diameters in the range d=40 nm-80 nm. The white dash lines correspond to locations of the hot photoluminescence bands.

Figure 4.6 | Simulated cavity mode spectra of resonant-sized cavity (d=70 nm). a-c) Frequency domain profiles of the electric field intensity (log scale) of resonant peaks at a) 2.505 eV, b) 2.342 eV, and c) 2.179 eV respectively. d) Simulated field profile along the Si wire axis (corresponding to 2.505 eV, m=5 mode). The field profile is taken 15 nm below the top surface in the antinode regions of the electric field. The decay length is estimated to be ~200 nm.

Figure 4.7 | a) Photoluminescence spectrum of resonant (d=70 nm) Ω-cavity Si for perpendicular and parallel polarizations (with respect to the nanowire long axis). Numbers 1-5 represent different phonon-mediated hot photoluminescence events. b) Photoluminescence spectrum for non-resonant (d=50 nm) cavity also for perpendicular and parallel polarizations. The perpendicular polarization reveals both cavity, "C", modes and hot photoluminescence, "P", modes. The cavity modes are confirmed by the simulated spectrum of the cavity electromagnetic modes.

Figure 4.8 | a) Phonon dispersion of crystalline Si (adapted from Wei et.al.[20]) The dashed vertical lines indicate phonon modes in high density-of-states (~zero slope) regions. Electronic dispersion of Si (adapted from Chelikowsky et. al.[22]), where dashed lines demonstrate the corresponding electronic states at the same momentum values as high-DOS phonons from a). a) and b) are used to explain the hot photoluminescence bands.

Figure 4.9 | Spontaneous emission enhancement as function energy mismatch between Ω-cavity mode and phonon-mediated hot photoluminescence state for a) resonant size nanowire (d=70 nm) and b) non-resonant size nanowire (d=50 nm). The vertical dash lines represent the positions of the hot photoluminescence bands reported in Figure 4.7a and intersect with the curve corresponding to spontaneous emission enhancement of those states.

Figure 5.1 | a) Schematic of silicon nanowire integrated with a 300 nm thick silver film to form a plasmonic nanocavity (drawn to scale). The native oxide of silicon (SiO_x) is used to separate the active silicon core from the silver shell. b) Scanning electron microscope (SEM) of silver coated silicon nanowire. c) Transmission electron microscope (TEM) image of a representative bare silicon nanowire demonstrating 1.5-2.5 nm of native oxide (denoted by dashed white lines) on the nanowire surface. d) Frequency domain spatial distribution of the electric field intensity in Ω-cavity Si (d=150 nm) demonstrating high order (m=9) mode (obtained via FDTD simulation) and e) corresponding magnetic field intensity.

Figure 5.2 | Photoluminescence spectrum of plasmonically-coupled silicon nanowire (*d*=150 nm) plotted vs. a) absolute emission energy and b) energy shift from the laser line for various excitation energies in the range 1.959 eV-2.708 eV. Spectra in (b) are plotted with a constant offset of 2×10^3 counts for clarity. The dashed boxes labeled A and B denote high-intensity emission bands. c) Schematic of the electronic dispersion of silicon featuring carrier excitation (magenta arrows), intra-band relaxation and hot-luminescence (green arrows) and radiative recombination from thermalized carriers (blue arrows). This process is examined for relaxation towards the selected conduction band minima at both the X-points (1.12 eV) and L-points (~2.1 eV).

Figure 5.3 | a) Magnified photoluminescence spectra of *d*=150 nm plasmonically-coupled silicon nanowire in low energy region demonstrating emission below the silicon bandgap at the L-point. (b-e) Variation in spectral positions of subpeaks in photoluminescence spectrum of plasmonically-coupled silicon nanowire. b) variation in band A and c) band B as a function of excitation energy for a single silicon nanowire size (*d*=150 nm). d) variation in spectral positions of band A and e) band B for several nanowire sizes as a function of excitation energy. Black arrows denotes location of first high intensity peak.

Figure 5.4 | Electromagnetic mode properties of plasmonically-coupled silicon analyzed via FDTD simulations and photoluminescence spectroscopy. a) nomenclature convention for modes polarized parallel (TM) and perpendicular (TE) to the nanowire long-axis. b) Variable-energy excitation photoluminescence spectra of *d*=150 nm Ω-cavity silicon nanowire juxtaposed with simulated cavity mode spectrum (orange curve). c-f) frequency domain profiles of the electric intensity (log scale) for cavity modes ordered from highest to lowest energy. g) Plot of quality factor versus azimuthal index (m), for TE modes in (b) and represented by the field profiles in (d-f).

Figure 5.5 | a-c) Photoluminescence spectra of plasmonically-coupled nanowires excited at various laser energies in the range 1.959 eV – 2.708 eV for nanowires of size a) d=151 nm, b) d=153 nm, and c) d=156 nm (all spectra are offset by 25,000 counts for clarity). The cavity mode spectrum of the *d*=151 nm nanowire is plotted on top of the photoluminescence spectra (high in red to low in blue) using the same energy scale. The variable energy excitation photoluminescence spectra demonstrate the role of mode structure in modulating high intensity subpeaks. In addition to size-dependent peak modulation, the modes, which red-shift with increasing size, also enable hot luminescence at lower energies for larger nanowires. d) Photoluminescence spectrum in low energy region (excited with 633 nm, He-Ne laser) for samples (a-c). e) Simulated cavity mode spectra of plasmonically-coupled silicon nanowires with diameters in the range *d*=150 nm to 160 nm as a function of energy.

Figure 5.6 | a) Temperature dependent photoluminescence spectra of plasmonically-coupled silicon (for two different samples) in the range 77 K-300 K. Increase in overall emission intensity with temperature follows expected trend for hot-luminescence from an indirect bandgap material as the phonon population increases with increasing temperature. b) Plot of total integrated counts as a function of temperature for samples shown in (a).

Figure 5.7 | Difference between the average emission energy and exciting laser energy (i.e. the mean emission shift) plotted against excitation energy. The variation in mean emission energy as function of size and excitation energy highlight the role of both cavity modes and electronic structure in modulating the emission spectrum.

Figure 6.1 | Model of optical refrigeration for a 4-level system. $|0\rangle$ and $|1\rangle$ comprise the electronic states of the ground state manifold separated by energy δE_g. $|2\rangle$ and $|3\rangle$ comprise the excited state manifold separated by energy δE_u. W_{rad} and W_{nr} are the radiative and non-radiative decay rates respectively, while w_1 and w_2 correspond to the phonon-mediated thermalization rate of the ground state and excited state manifolds respectively. [Adapted from reference 10]

Figure 6.2 | Stokes and anti-Stokes Raman scattering for bare CdS nanowire (d~200 nm) with 5 nm conformal SiO_2 coating. a) Raman spectrum featuring broad photoluminescence peak centered at ~1157 cm-1 (2.474 eV) which is attributed to excitonic emission from CdS. b) Magnified view of region near 2LO Raman peaks in both the Stokes and anti Stokes region. Spectra have been baseline corrected to eliminate the photoluminescence background and provide accurate values of the Raman intensity.

Figure 6.3 | Stokes and anti-Stokes Raman scattering for metal coated CdS nanowire with 5 nm conformal SiO_2 coating and 300 nm Ag metal shell (green curves). a) Raman spectrum featuring broad photoluminescence peak centered at ~980 cm^{-1} (2.452 eV) which is attributed to excitonic emission from CdS. The spectrum of a bare (non-metal coated) CdS nanowire is also plotted for comparison (black curve). b) Magnified view of region near 2LO Raman peaks in both the Stokes and anti Stokes region. Spectra have been baseline corrected to eliminate the photoluminescence background and provide accurate values of the Raman intensity.

Figure 6.4 | Atomic force microscopy of CdS nanobelts. a) AFM image of typical thick CdS nanobelt with thickness of ~240 nm. b) AFM profiles of typical thick and thin CdS nanobelts as discussed in section 6.2.

Figure 6.5 | Differential Luminescence Thermometry temperature calibration curve and schematic of measurement scheme. a) Photoluminescence at several times in the range 0-18 minutes for a CdS sample at a fixed temperature of 268 K. The photoluminescence peak position reaches a steady state within ten minutes of stabilization of the sample stage temperature. b) Photoluminescence spectra for a representative CdS samples at various temperatures in the range 268 K to 312 K (plotted at 8 K intervals for clarity). c) Plot of change in temperature, ΔT, vs. change in spectral peak position, ΔE, obtained from the photoluminescence data in (b). The blue line represents a linear fit to the data. d) schematic of measurement process using a pump laser (514.5 nm) for cooling and a low power probe laser (473 nm) for monitoring the shift in the photoluminescence spectrum.

Figure 6.6 | Optical image of CdS nanobelt suspended over PMMA boxes (~9 μm x 9 μm) with a ~4 μm separation. The bright emission from the nanobelt is anti-Stokes photoluminescence resulting from excitation below the bandgap at (with the 514.5 nm pump laser).

Figure 6.7 | Anti Stokes photoluminescence in bare CdS nanobelts with thickness *d*~200-300 nm. a) Photoluminescence in CdS nanobelt excited with the 514.5 nm line of a CW laser (inset: optical image of anti Stokes photoluminescence excited with pump laser). b) Magnified view of anti Stokes photoluminescence spectrum in CdS nanobelt featuring a blue shift of ~1.74 meV (~0.3 nm), which reaches a steady state after 15 minutes of excitation with the pump laser. c) Magnified view of anti Stokes photoluminescence spectrum in CdS nanobelt featuring a blue shift of 2.6 meV (~0.5 nm) after 1 hour of excitation with pump laser.

Figure 6.8 | Pump-probe differential luminescence thermometry of bare and passivated CdS nanobelts. a) Stokes Photoluminescence spectra of a CdS nanobelt featuring the spectrum at time t=0 (black curve) and t=15 min (after pump excitation; red curve). The difference spectrum (DLT curve) is plotted in magenta. c) Stokes Photoluminescence spectra of a CdS nanobelt passivated with SiO_2 featuring the spectrum at time t=0 (black curve) and t=10 min (red curve). The difference spectrum (DLT curve) is also plotted in magenta.

Figure 6.9 | Probe photoluminescence peak position and sample stage temperature vs. time for two bare CdS nanobelt samples in the temperature range a) 307 K-311 K and b) 311 K-316K.

Figure 6.10 | Laser cooling of plasmonically-coupled CdS in geometry optimized for top-down excitation and measurement. a) Schematic of CdS integrated with a 15 nm thick Ag film. Excitation is performed through the Ag film as denoted by the dark green and purple arrows. Emission is also measured through the substrate (bright green arrow). b) Stokes Photoluminescence spectra of a CdS nanobelt featuring the spectrum at time t=0 (black curve) and t=15 min (after pump excitation; red curve). The difference spectrum (DLT curve) is plotted in magenta. c) Magnified view of anti-Stokes photoluminescence (excited with probe laser) of data presented in (b).

Figure 6.11 | Laser cooling of plasmonically-coupled CdS using inverted geometry. a) Schematic of CdS integrated with a 300 nm thick silver film. Excitation is performed through the substrate as denoted by the dark green and purple arrows. Emission is also measured through the substrate (bright green arrow). b-d) Magnified view of Anti-Stokes photoluminescence (excited with probe laser) b) after 10 minutes of cooling, c) after 2 minutes of warm up time (after excitation with pump laser has ceased) and d) 5 minutes of warm up time. The original probe photoluminescence spectrum at t=0 is plotted in black in all three plots as a reference point.

Figure 7.1 | Photoluminescence of plasmonically-coupled Si nanowire (*d*~150 nm) excited with the 457.8 nm laser line of an Argon-ion laser (continuous wave, blue curve) and Ti:Sapphire laser (pulse width 140 fs, 80 MHz repetition rate) tuned to 458 nm (magenta curve).

Chapter 1. Introduction

1.1: Cavity Electromagnetics Primer: Light Emission in Optical Cavities

When we think of optics of materials, we typically recall phenomena such as reflection and refraction, i.e. geometric optics. This is an example of the interaction between light and matter, where light moves the free and bound charges in a material giving rise to all the optical phenomena.[1] Yet, some of the most interesting effects arise when (i) light interacts with active media, that is materials which have electronic resonances in the same spectral range of the incoming light, and (ii) when that light is placed in a light-trapping box. In 1946, Edward Purcell was the first to realize that the rate of light emission from a radiating dipole (such as the electron-hole pair in a semiconductor) is a function of the surroundings of that optical emitter.

Originally developed for radio-frequency operation, the enhanced spontaneous emission rate of the emitter may be expressed as:

$$\gamma = \frac{3Q}{4\pi^2}\left(\frac{\lambda^3}{V_m}\right)\gamma_0 \qquad \text{Eq. 1.1}$$

where γ_0 is the spontaneous emission rate in free space, λ is the wavelength of the emitted radiation in the host medium, Q is the quality factor of the electromagnetic mode that couples to the optical emitter, and V_m is the mode volume of the same.[2] The quality

factor is a measure of the optical cavity to store electromagnetic energy; analogous to how a capacitor stores electrical energy. It can also be considered as a measure of how long light is confined to the optical cavity before leaking into the vacuum. In the denominator we find the mode volume, which can be expressed as:

$$V_m = \frac{\int \varepsilon(r)E^2(r)d^3r}{(\varepsilon(r)E^2(r))_{max}} \qquad \text{Eq. 1.2}$$

where $\varepsilon(r)$ is the dielectric constant of the material and $E^2(r)$ the electric field intensity. This is a measure of the confinement of the electromagnetic field. It has the units of volume and, in fact, is often quoted with respect to the volume taken up by light in free space, λ^3. The enhancement in the spontaneous emission rate, γ/γ_0, is known as the Purcell factor, and depends on the ratio Q/V_m. In other words, in order to obtain highly enhanced spontaneous emission rates, we should place optical emitters in environments that have long lived modes (high Q) and where the optical modes are also highly confined (low V_m). As expected, these two quantities are typically anti-correlated. The smaller the mode volume, the more likely it is that light will leak out (lower Q) and vice versa. Furthermore, there is a fundamental limit on the mode volume of light, known as the diffraction limit, where for example in the case of waveguided modes, light may not be confined to dimensions much smaller than one-half its wavelength in the host medium (this is also known as the "cutoff energy" in the waveguide literature).[3] For completeness's sake, we note that the above expression assumes perfect spectral matching between the emitter and the optical cavity mode. In reality, both spectral overlap as well as spatial and polarization overlap between the optical emitter and

electromagnetic mode must be taken into account for accurate computation of the Purcell factor[4] (see section 4.6). The physical origin of the Purcell effect is rooted in Fermi's golden rule, where the spontaneous emission rate of an optical emitter may be computed as:

$$\gamma = \frac{2\pi}{\hbar} \left| \langle f \left| \vec{d} \cdot \vec{E}(\vec{r}) \right| i \rangle \right|^2 \rho(\hbar\omega) \qquad \text{Eq. 1.3}$$

and where $\langle f \left| \vec{d} \cdot \vec{E}(\vec{r}) \right| i \rangle$ is the transition dipole matrix element for the transition between state *f* and state *i*, and $\rho(\hbar\omega)$ is the photon density of states. Here, the Q/V_m ratio from the Purcell factor in classical terms may be related to the density of photon states, ρ, in the quantum electrodynamics picture. For an insightful derivation of the Purcell effect in terms of classical parameters (as expressed above), but beginning with Fermi's golden rule, the reader is referred to a recent review by Maier et al.[5]

Though it was initially developed for radio-frequency operation, the Purcell effect is a general principle that can be applied across the electromagnetic spectrum. Advances in nanofabrication have enabled the engineering of optical cavities with nanoscale dimensions, thus tuning their resonances to the nanoscale portion of the electromagnetic spectrum (in terms of wavelength), or in other words, the UV-visible-near IR frequencies. This is a boon from the perspective of semiconductor technology as many relevant elemental and compound semiconductors (Ge, Si, InP, GaAs, etc.) feature band gaps and light emission in this spectral range.[6] Implicit here is the fact that the electron-hole pairs of semiconductors may function as optical emitters, the light emission of which may be

tuned as a function of the surroundings. As mentioned above, due to the fundamental limit on the mode volume, and thus the size of the optical cavity, research has focused on optimizing the quality factor of optical cavities.[7,8] Figure 1.1 is a summary of conventional optical cavities, where the light source is a semiconductor quantum dot that is embedded in an optical cavity fabricated via top-down methods.[8] Optical cavities in the Whispering Gallery Mode resonator geometry (where light is confined to the circumference of a circular cavity) excel at hosting high Q modes; 125 being one of the highest Purcell factors achieved at optical frequency with a corresponding quality factor of 12,000.[9] Quality factors as high as 10^8 have been achieved at IR frequency. [10]

Such Purcell enhancement schemes suffer from three main drawbacks. First, as can be observed in figure 1.1, high Q cavities feature large spatial footprints generally of several microns limiting their applicability in nanotechnology. Secondly, in these cases the optical emitter and optical cavity are two separate entities which must be properly aligned to achieve the desired results, and which adds another level of difficulty to their fabrication. Finally, perhaps the most fundamental limitation on these high Q cavities is their limited operational bandwidth. A high quality factor, or long-lived mode in time domain, equates to a narrow peak in frequency space, where the peak width, Δf, is related to the quality factor at the resonance frequency, f_0, as $\Delta f = f_0/Q$. For the previously mentioned high-Q resonator (Q=12,000), this equates to a mode width <1 meV, thereby placing a significant constraint on the operation of this hybrid optical cavity-semiconductor device. If we are only interested in enhancing spontaneous emission, then the best systems would be monolithically integrated optical cavity-

semiconductor hybrid structures, which optimize Q/V_m not just through high Q and low V_m but rather through low Q, which equates to operation over a broad frequency range, and ultralow mode volumes, significantly below the diffraction limit, thereby maintaining the high Q/V_m ratio. Metals excel at confining light into deep-subwavelength dimensions, where light couples to surface modes on the metal surface and acquires both photonic and electronic character. This type of optical mode is termed the "surface plasmon" and will be the focus of the next subsection.

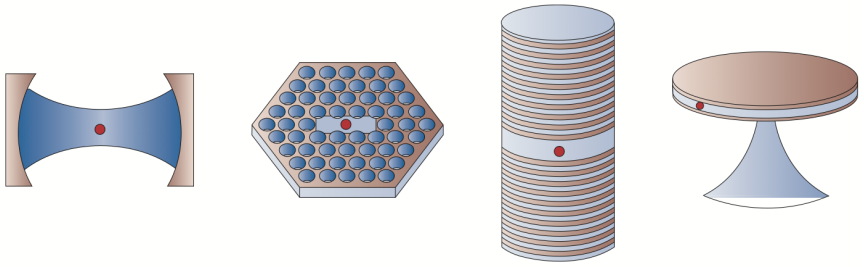

Cavity	Length = 42.2 μm: Width = 23.4 μm:	Photonic crystal slab	Micropillar	Microdisk
λ (nm); E (eV)	852.4; 1.45	1,182; 1.32	937; 1.32	744; 1.66
Q	4.4×10^7	6,000	7,350	12,000
V (μm^3)	$18{,}148 = 3 \times 10^4(\lambda/n)^3$	$0.04 = (\lambda/n)^3$	$0.3 = 16(\lambda/n)^3$	$0.07 = 8(\lambda/n)^3$
$F_P = \frac{3Q\lambda^3}{4\pi^2 n^3 V}$	114	441	36	125
$\kappa/2\pi$ (GHz)	0.008	42	44	34

Figure 1.1 | Different all-dielectric cavity paradigms and corresponding cavity Quantum Electrodynamics parameters. The red dot corresponds to the position of the optical emitter (quantum dot). For the full figure (including Rabi Splitting magnitude, etc.) please refer to the original review article by Khitrova et. al.[10] [Adapted from Reference 10]

1.2: Surface Plasmons and their Role as Optical Cavities and Antennas

Metals excel at confining light into deep-subwavelength dimensions. When light (photon) is incident on the surface of a metal (in the spectral region where the metal has negative values of permittivity), the surface electrons and photon may form a strongly coupled system, also known as the surface plasmon polariton (SPP).[11] The surface electrons serve to "anchor" the light to the surface of the metal resulting in an electromagnetic mode that may only propagate on the surface of the metal. The SPP features a dispersion relation that is similar in form to that of other strongly coupled systems (such as the exciton-polariton in semiconductors[1]) and which dictates its physical properties. For a detailed description of SPPs the reader is referred to section 1.2.1. In a similar fashion, localized surface plasmons (LSPs) are non-propagating modes, which may be excited in deep-subwavelength structures where the light-matter interaction may be treated quasistatically.[12] Physically speaking, the key difference between SPPs and LSPs is that LSPs are not bound to the same dispersion relation as SPPs, which facilitates their excitation from the far-field[12] (see section 1.2.1). Both are surface plasmon (SP) resonances. Given that ratio of surface to volume increases as the dimensions of the system shrink, at the nanoscale, the optical properties of metals are dominated by SP resonances.

---

[1] For a general overview of strong light-matter coupling and its observation in semiconductors, the reader is referred to C. F. Klinghshirn's "Semiconductor Optics", 3rd ed., Chapters 5 and 6.

Though the exact form of the surface plasmon resonance frequency depends on the dispersion relation, which itself will be a function of geometry (i.e. boundary conditions) and material properties, it will generally scale with charge carrier concentration. Metals with high free electron densities, such as Ag and Au, posses SP resonances in the visible regime. Au nanostructures, for example, interact with light with wavelengths on the order of a micrometer and confine it to dimensions of a few nanometers, ~100 times smaller, far below the diffraction limit[13-15] and vice-versa. In other words, these metal nanostructures function as antennas, which operate at optical frequency. Moreover, the ultra-low mode volumes associated with sub-diffraction limited confinement enable truly nanoscale photonics.

SP-based devices, where the exciting source is light from the far field and where the only spectrally-matched material resonance is that of the plasmonically-active medium, have enabled applications such as single-molecule detection,[16,17] targeted cancer therapy[18], more efficient solar cells[19], and even optical cloaking.[20] Moreover, the ability to transmit information at both fiber optic speeds and at truly nanoscopic length scales[21] has spurred research on the unique properties of sub-diffraction limited SP-based optics such as propagation, confinement and local field enhancement in nanostructured systems.[22-25] The physics of these devices is certainly interesting in its own right, but yet another level of complexity (and potential applications) arises when SPs are interfaced with active materials, that is materials with electronic resonances (and associated spontaneous light emission) that are spectrally matched to the SP resonance. It should be noted that the term “active plasmonics” has also been used to label systems where the

propagation of SPPs is controlled via passive means, for example by changing the dielectric environment.[26] In this thesis, the term active refers to the active media that is interfaced with SP resonances**.** Tailoring of the light emission properties of active materials is one such application, which has received significant attention in recent years and is largely based on the interaction between optical antennas and active media.[15 27-31] Section 1.3 provides an overview of SP-enhanced light emission and examines the effect of length scales on light-matter interaction. First, the reader is provided with a more detailed description of surface plasmons.

1.2.1: Surface Plasmon Polaritons: a Formal Description

The optical properties of non-magnetic materials are dictated exclusively by the complex dielectric function of the material, $\varepsilon(\omega, k)$ which may be a function of both frequency and wavevector (or time and space in the Fourier domain). If we assume that the wavelength of the electromagnetic radiation is much larger than dimensions over which there is a gradient in material properties, such as the unit cell spacing (on the order of Angstroms) or electron mean free path (on the order of tens of nanometers), then the dielectric function may be considered to be a function of energy only, which is in general still accurate for metal structures up to UV frequencies.[12]

By treating the highly mobile electrons of a metal as a free electron gas and employing a driven oscillator model (where the incident electromagnetic radiation is the driving term), we arrive at a free-electron model for the metal dielectric function.

[2]Barring interband transitions the dielectric function, ε, of metals may be readily described by the free electron model (also known as the Drude model):

$$\varepsilon(\omega) = \varepsilon_\infty - \frac{\omega_p^2}{\omega^2 + i\omega\gamma} \qquad \text{Eq. 1.4}$$

where ε_∞, ω_p, and γ are the static permittivity, electron plasma frequency, and damping coefficient.[32] [3]In general, materials with highly mobile electrons such as metals, doped semiconductors, or complex oxides, may undergo collective oscillations of their electrons in the bulk, where these behave as a plasma, the quanta of which is called the *plasmon*.[33] Boundary conditions at the material's surface, on the other hand, lead to *surface plasmons* (described below), which, due to high surface-to-volume ratios, dominate the optical properties of plasmonically-active structures (such as metals at optical frequency) at the nanoscale.

As discussed in section 1.2, light that is incident on a metal surface may couple strongly to the electrons on the surface resulting in a polariton, namely the *surface plasmon polariton* (SPP). Surface plasmon polaritons are a class of propagating modes at the interface of metals and dielectrics, thus, in order to arrive at SPPs we must apply the

---

[2] The interested reader may refer to derivations of the free electron model by Pedrotti et. al. "Introduction to Optics", 3rd ed., Chapter 25 and Maier et. al. "Plasmonics: Fundamentals and Applications", Chapter 1.

[3] For further discussion of optical properties due to bulk plasmons refer to Charles Kittel's "Introduction to Solid State Physics", 8th ed., Chapter 14.

appropriate boundary conditions to Maxwell's equations (Figure 1.2). [4]The resulting solutions demonstrate evanescently decaying fields in the direction perpendicular to propagation and have both TM (only E_x, E_z, and H_y non-zero components) and TE (only H_x, H_z, and E_y non-zero components) polarization, of which only the TM solution satisfies continuity at the interface[38]. In other words, SPPs must have electric field components in the direction of propagation (i.e. the plane of incidence) and magnetic field components perpendicular to the direction of propagation. Furthermore, continuity at the interface,

$$\frac{k_d}{k_m} = -\frac{\varepsilon_d}{\varepsilon_m} \qquad \text{Eq. 1.5}$$

where k_d, k_m, ε_d, and ε_m are the wavevectors and permittivities perpendicular to the interface in the dielectric and metals respectively, demands that $\varepsilon_m < 0$, or that plasmonically-active materials have negative values of permittivity. To summarize, SPPs are TM polarized surface modes, which demonstrate evanescent decay (exponential decay as function of distance) of the electric field perpendicular to the interface and may only occur when the permittivity (or real part of the dielectric function) of either media is negative (Figure 1.3).

[4] For a detailed derivation of propagating surface plasmon modes, refer to Stefan Maier's "Plasmonics: Fundamentals and Applications", Chapter 2.

In order to simplify examination of the free electron dielectric function, we may use the high frequency approximation where ω is close to (but less than) ω_p. The dielectric function then simplies to,

$$\varepsilon(\omega) = 1 - \frac{\omega_p^2}{\omega^2} \qquad \text{Eq. 1.6}$$

Thus, even at high frequencies close to the plasma frequency the real part of the dielectric function is negative and satisfies one the requirements for SPP excitation. Another important result is the dispersion relation of SPPs, which for the flat metal-dielectric interface is expressed as,

$$k_x = \frac{\omega}{c}\left(\frac{\varepsilon_d \varepsilon_m}{\varepsilon_d + \varepsilon_m}\right)^{\frac{1}{2}} \qquad \text{Eq. 1.7}$$

Figure 1.4 depicts the above dispersion for light and SPP in different media. There are two important conclusions we may draw from this diagram. The first, is that the SPPs cannot be excited directly from incident light in air, or in any medium which simultaneously hosts the incident light and interfaces with the metal. The reason is that SPPs have higher momentum values than freely propagating light, which makes sense from a physical picture perspective as SPPs are composed not only of moving mass-less particles (photons) but also electrons. Thus in order to excite SPPs, we must either couple light from an external higher-dielectric medium (i.e. via prism coupling) or use a grating. It should be noted that excitation of SPs is facilitated by coupling to active structures such as light emitting semiconductors, which enables near-field excitation. In other

words, SPPs may also be excited in the near-field via dipolar light emission from semiconductors placed in the evanescent tail of the SPP mode in both planar[31,34-39] and curved metal optical cavity geometries.[28,29]

Secondly, close to the surface plasmon frequency (discussed below) the energy dispersion becomes flat over a large energy range. The photon density of states is proportional to $\left(\frac{\partial E}{\partial k}\right)^{-1}$ thus, SPPs exhibit very high density of photon states close to the surface plasmon resonance, an essential attribute which forms the basis for much of the work presented in this thesis (see section 1.2 on the relation between photon density of states and enhanced light emission and section 1.3 on SP enhanced emission of light). It should be noted that the SP resonance frequency is different, but closely related to the bulk plasma frequency, ω_p and dielectric environment. For this idealized case, the SP resonance frequency maybe expressed as:

$$\omega_{sp} = \frac{\omega_p}{(1+\varepsilon_d)^{1/2}} \qquad \text{Eq. 1.8}$$

Furthermore the plasma frequency is related to the free electron density via:

$$\omega_p = \frac{ne^2}{\varepsilon_0 m} \qquad \text{Eq. 1.9}$$

where *n* is the free electron density*, and e,* ε_0 and *m* are the electron charge, permittivity of free space and effective electron mass respectively. This relation accounts for the fact the SP resonance of metals with high a high density of conduction electrons such as Au or Ag is typically found in the visible regime.

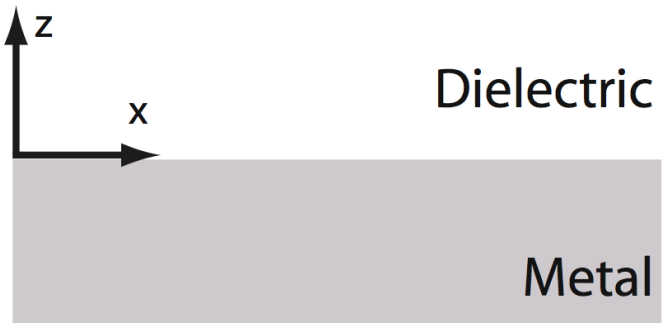

Figure 1.2 | Boundary conditions for derivation of SPPs propagating in the x-direction. The dielectric function varies in the z-direction only.[12] [Adapted from Reference 12]

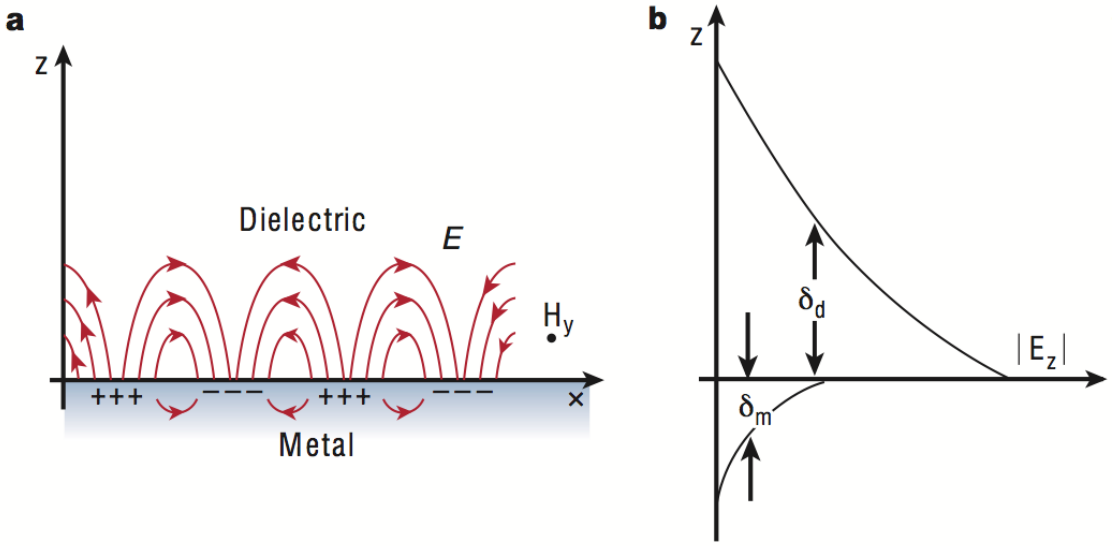

Figure 1.3 | a) Schematic of SPP propagating in x-direction showing coupled electron and electromagnetic field oscillation. b) Evanescent decay of same SPP as a function of distance into metal and dielectric. The SPP is highly confined to the interface and demonstrates faster decay into the metal due to their lossy nature.[40] [Adapted from Reference 39]

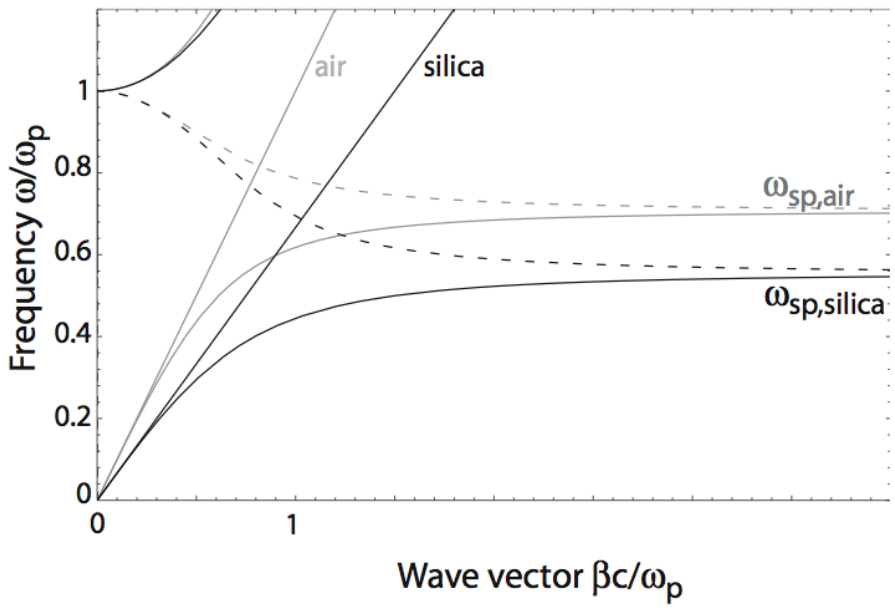

Figure 1.4 | E vs. k diagram (dispersion) of SPPs at a flat metal-dielectric interface. The metal is described by the dielectric function and has negligible damping ($\gamma = 0$ and therefore $Im(\varepsilon) = 0$). The solid lines describe the real part of the wavevector denoting propagating waves and the dotted lines correspond to the imaginary part denoting loss.[12] [Adapted from Reference 12]

1.3 Surface Plasmon Enhanced Light Emitters

Yet another way to examine the potential of plasmonically active metallic nanostructures (i.e. optical antennas) to enhance light emission is to examine the effect of length scales. Electronic transitions of a single optical emitter (i.e. organic dye molecule or quantum well) which lead to spontaneous emission involve electrons confined to few nm length-scales, while the light which they emit has wavelengths on the order of ~1 micron, thus the immediate environment of the light emitter is below the diffraction limit and cannot efficiently host electromagnetic modes. More to the point, the power emitted by a time-harmonic current element of length l is directly proportional to $(l/\lambda)^2$ where λ

is the wavelength of the emitted light, thus this length-scale mismatch leads to, for example, the low absorption cross sections and low emission quantum efficiencies of single molecules.[41] Optical antennas mitigate this length-scale mismatch by confining light to dimensions more amenable to the length scales of an electron confined in a molecule and have led to significant enhancements in fluorescence intensity ($>10^3$)[15] and Purcell enhancements up to ~30 times[15,27] for a single molecules and of ~10^3 for "bulk" (non-quantum confined) semiconductor materials.[28,29] The reader is referred to several excellent reviews for more discussion on relating radio frequency antenna theory to metallic nanostructures[41], optical antenna action (i.e. re-direction of light emission and polarization)[5,41] optical-antenna enhanced quantum yield[5,42] and applications thereof.[5,41-43]

The tailoring of spontaneous emission lifetimes (a.k.a. Purcell enhancement) of organic molecules via coupling to surface plasmons has been studied since the 1960s[44] with early experiments demonstrating both fluorescence enhancement[45,46] and quenching[47,48] of the spontaneous emission intensity. Indeed it was recently shown, both experimentally and theoretically, that surface plasmon enhanced spontaneous emission will transition from a region of enhancement to quenching with decreasing separation from a metal surface (see Figure 1.5).[49] This is because spontaneous emission depends on both the excitation rate of charge carriers and the quantum yield, which have different functional forms. The excitation rate increases monotonically with decreasing separation from the metal surface. The quantum yield, on the other hand, initially rises with decreasing separation but eventually peaks and decreases with proximity to the metal

surface. It was shown by Novotny et al., that the underlying cause is the breakdown of dipole emission and thus excitation of higher order modes within the emitter itself, which leads to increased ohmic losses in the metal surface, a non-radiative pathway.[49] It should be noted that the quantum yield, q, of an optical emitter is equal to:

$$q = \frac{\gamma_r}{\gamma_r + \gamma_{nr}} \qquad \text{Eq. 1.10}$$

where γ_r and γ_{nr} are the radiative and non-radiative decay rates respectively. Thus, after a minimum separation between the excited carrier (active material) and metal, the non-radiative decay rate will increase faster than the radiative decay rate, lowering the quantum yield.

Metallic nanostructures have been interfaced with both organic and inorganic optical emitters leading to Purcell factors of up to ~100, and where the spontaneous emission enhancements are based on interfacing with both LSP modes[15,27,49-56] and SPP modes[30,34-37,57,58] These systems constitute more efficient light emitters and where optoelectronic components based on these materials may be modulated at frequencies up to 100 times that of their bulk counterparts (due to the enhanced recombination rates). Perhaps an even more technologically relevant application is the development of truly nanoscale laser sources. By coupling SP modes with a gain medium, the SPs themselves may be amplified by making multiple passes through the gain medium embedded in a metal nanostructure resulting in surface plasmon amplification by stimulated emission of radiation also known as SPASER action.[59] This is due to LSPs and thus does not require an optical cavity. A more general term, “plasmonic laser”, which applies to all laser

systems that employ SPs to enhance lasing (i.e. propagating SPP and LSP-based) has been used in recent literature.[31,60] Optically pumped plasmon lasers have been synthesized via both LSPs and SPPs such as in a Au-nanoparticle functionalized with an organic dye[54] and a CdS nanocrystal interfaced with a Ag film.[31,37] All cases led to lasing from deep sub-wavelength regions (~$\lambda/12$ and $\lambda/20$ respectively) and enhanced spontaneous emission.

It should be noted that the enhanced light emission discussed thus far is a weak-coupling phenomenon, where the interaction between the radiating dipole and the vacuum electric field can be treated using perturbation theory and where the spontaneous emission rate may be computed using Fermi's golden rule (see section 1.1).[5] Strong-light matter interaction, on the other hand, is possible when the SP dephasing lifetime is longer than the time it takes for energy to be transferred between the exciton (otherwise known as the electron-hole pair) and plasmon; an effect known as Rabi oscillations. Strong light-matter coupling between SPs and excitons has been predicted[61] and observed[62-65] where the SP and exciton form yet another strongly coupled quasi-particle, a polariton. For a general overview of strong-light matter interaction we refer the reader to Klingshirn's "Semiconductor Optics", (Chapters 5 and 6).[66] Discussion on strong-light matter coupling with SPs will be omitted as it is outside the scope of this thesis work, but the interested reader is referred to a brief review on the subject and references therein.[67]

The final piece of the puzzle is the addition of the semiconductor nanowire. As will be explored in the remainder this thesis, the unique optical properties of

semiconductor nanowires, when integrated with plasmonic optical nanocavities, result enhancement of spectroscopic properties of the former to unprecedented levels, with applications including orders of magnitude faster light emission, broad-band emission from a non-light emitting material, anomalous absorption across the visible spectrum, and finally SP-enhanced optical cooling of semiconductors. The combination of semiconductor materials physics with optical cavity engineering has led to a thesis topic, which truly resides at the interface of optical physics with materials science. The final introductory section provides a brief overview of semiconductor nanowires and their role in nanoscience, with an emphasis on their optical properties.

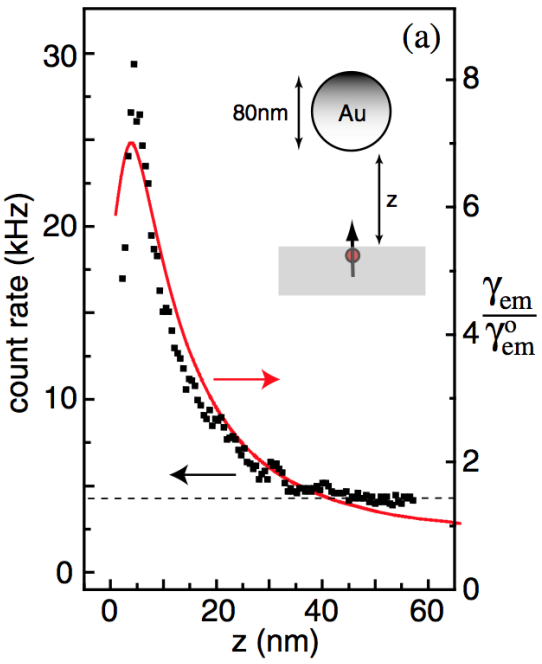

Figure 1.5 | Rate of experimentally measured fluorescence counts (left axis) and Purcell enhanced-spontaneous emission rate (right axis) as function of separation (z) between ultra-low concentration (single molecule level) of Nile-blue, a fluorescent dye, emitting at 650 nm and a Au sphere at tip of a Near Field Scanning Optical Microscope (as depicted in inset).[49] [Adapted from Reference 48]

1.4 Semiconductor Nanowires and their Role in Nanoscience

Due to their 1-D nature and their ability to simultaneously conduct photons, phonons, electrons and the plethora of associated quasi-particles, semiconductor nanowires are firmly poised at the forefront of nanotechnology research; a testament to which is the explosion of publications per year witnessed over the previous decade (Figure 1.6). From an engineering point of view, interest in semiconductor nanowires is fueled by our ability to readily synthesize high crystalline quality nanowires of virtually any composition and architecture[68] (see section 2) and in particular, with exceptional electronic[69] and optical[70] properties. The single crystalline nature of semiconductor nanowires equates to high electron mobilities, while control over their architecture facilitates fabrication of nanoscale p-n junctions resulting in robust nanoscale integrated circuit elements[71,72] that are fully programmable (and reprogrammable).[73] Furthermore, their optoelectronic properties and dimensions have driven the interface of semiconductor nanowires with biological species down to the cellular level.[74,75] Finally, the ability of semiconductor nanowires to trap light and therefore enhance light-matter interaction, has unleashed their potential as platforms for nanophotonics as will be explored in the remainder of this section.

The rich physics of semiconductor nanowire optics stems from their ability to serve as both optical cavities and sources of light. Semiconductors are generally high refractive index materials such that nanowires composed of these materials can effectively trap light. Nanowire resonances have been proven to be versatile and may be

broadly categorized as modes that travel along the nanowire long axis, in other words with k-vector parallel to the long axis and those which propagate in the cross section of the nanowire, only with k-vector perpendicular to the long axis. The modes with k-parallel (to the nanowire long axis) are simply the waveguided modes of a dielectric cylindrical waveguide and are readily described by solving Maxwell's equations,[76] but with the potential for significant guiding of light outside of the nanowire due to the nanoscale dimensions.[77] Figure 1.7a,b features finite element simulations of electromagnetic mode structure inside of a nanowire made cadmium sulfide, a group II-VI semiconductor that is known for its light emitting properties (see chapter 3). The mode selected for simulation is the lowest order (HE_{11}) mode at a wavelength corresponding to the B-exciton resonance of CdS at 480 nm (see chapter 3 for more discussion on the electronic structure of CdS). In this regime the nanowire effectively behaves like a fiber optic cable at the nanoscale as exhibited by the cross section parallel to the long axis (Figure 1.7a), where the electric field is confined to the nanowire and transmitted from end to end. On the other hand, the cross sections perpendicular to the nanowire long axis (Figure 1.7b) demonstrate leakage of the field outside of CdS as the diameter of the nanowire decreases, a result of operating close to the diffraction limit. These waveguided modes, coupled with the electronic properties of semiconductor nanowires, have produced highly sensitive photodetectors[78,79] and nanoscale lasers, which are both optically pumped[80,81] and electrically pumped.[82]

The modes with k-transverse (to the nanowire long axis) are known as either "leaky mode resonances"[83] or whispering-gallery modes (WGM).[84] As can be examined

from the cross section of computational electromagnetics simulation of a germanium nanowire (Figure 1c), these modes propagate in the angular direction, along the nanowire circumference, and are loosely confined. These WGM resonances have been used to enhance light absorption in semiconductor nanowires with direct applications as improved photodetectors[83] and which couple the enhanced electronic properties of semiconductor nanowire solar cells[85] with their light trapping ability for even higher efficiency.[86]

The light-emitting property of semiconductor nanowires stems from the electron-hole pairs that form after the semiconductor is imparted with super-bandgap energy, and which eventually decay radiatively. Several semiconductor materials such as ZnO, ZnSe, and CdS, exhibit high oscillator strengths, which leads to the formation of exciton-polaritons, a strongly coupled quasi particle composed of the electron-hole pair[66] (see section 1.2, footnote i). Thus, semiconductor nanowires serve as both optical cavities and nanoscopic sources of strongly[87] (and weakly) coupled light. For an in-depth overview of light-matter interaction in semiconductor nanowires we refer the reader to a recent review on the subject.[88] [89] Our recently developed understanding of the spectroscopic properties of semiconductor nanowires, which again, stems from the electromagnetics of subwavelength nanowire optical cavities and their solid state light-emitting processes have led to novel physical phenomena such as tunable light-matter coupling[90] and from an applications perspective, all-optical logic gates based on polariton-polariton scattering.[91]

With this understanding of semiconductor nanowire optics in mind, we may begin to tune the spectroscopic properties of nanowires with nanophotonics, i.e. by interfacing nanowires with plasmonic nanocavities, further confining light to dimensions far below the diffraction limit (see section 1.2 and 1.3). Certainly, many of the principles of Q/V_m optimization outlined above may be applied to semiconductor nanowires as they too are active media, but yet another level of complexity is attained due to the fact that these nanowires also act as optical cavities (discussed above). Thus, as we will observe in the following chapters, tuning of the spectroscopic properties of semiconductor nanowires will involve the interplay between nanowire optical modes and the surface plasmon modes of plasmonic nanocavities, which will result in the tuning not only of their light emission properties, but also engineering of the absorption/scattering properties of these plasmonically-coupled nanowires.

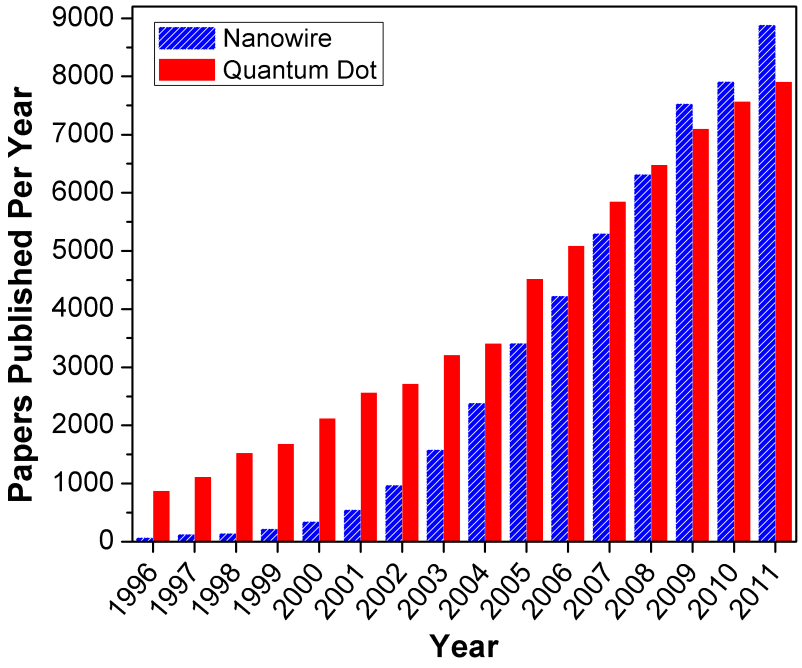

Figure 1.6 | Number of publications involving nanowires and quantum dots published between 1996 and 2011. Results were obtained by performing an ISI keyword-based search for each year.

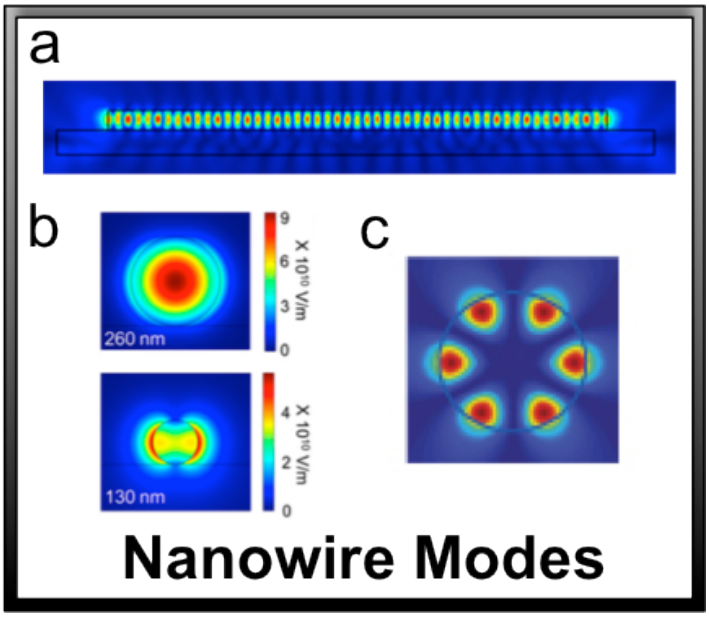

Figure 1.7 | Computational electromagnetics simulations of electromagnetic modes in semiconductor nanowires with k vector parallel and perpendicular to the nanowire long axis. a) Full 3D finite element simulation of the electric field intensity profile of the HE_{11} waveguided mode in CdS nanowire (diameter=200 nm, length=5 micron). The cross section is taken parallel to the nanowire long axis and b) cross sections of CdS nanowires of various diameter (inset) taken perpendicular to the nanowire long axis.[90] c) Simulation of the electric field profile of the TM_{31} WGM resonance in germanium nanowire (diameter=110 nm).[83] [Adapted from References 82 and 88]

1.4.1: Surface Plasmon Enhanced Lasing From a Semiconductor Nanowire

We now make a small digression to briefly review recent work by Zhang et al. that combines the semiconductor nanowire (composed of CdS) with a metal film (silver) to achieve surface plasmon enhanced lasing and spontaneous emission. One of the unifying themes of this thesis is the use of the interaction between semiconductor nanowire modes with surface plasmon modes to manipulate the spectroscopic properties

of the nanowire. Where, Zhang's experiments employ the waveguided (k-parallel) modes of the nanowire (discussed above) this thesis work is based on the WGM (k-transverse) resonances of the nanowire to hybridize with the surface plasmon mode, yet also incorporates key features of plasmonic-cavity design established here.

The planar nanowire-on-film geometry is outlined in figure 1.8a, where a CdS nanowire (with diameter, *d*, 50-400 nm) is interfaced with a thick silver film, but separated from the metal film with a 5 nm insulating layer (MgF_2). The insulating gap is critical both in terms of the quantum yield of the optical emitter and of the electromagnetic modes involved. As discussed in section 1.3, proximity of an optical emitter (such as CdS) to a metal surface can actually quench emission due to both ohmic losses and high order electromagnetic modes excited within the emitter itself, even though the electron-hole pair excitation rate will increase asymptotically with decreasing separation from the metal[49] (Anger et al. predict 5 nm as an optimal separation between emitter and metal which was reproduced experimentally by Oulton et al.[31]). Perhaps even more critical are the new hybridized electromagnetic modes that are enabled by the thin-insulating gap. By using a low refractive index gap, Oulton et al. demonstrated, through finite element analysis, that a significant portion of the field is stored near the optically loss-less insulating gap.[92] The waveguided modes are plasmonic in nature (i.e. confined to deep subwavelength dimensions of $\sim 10^{-2}\ \lambda$ near the metal surface), yet a majority of the field is guided outside of the lossy metal (in the insulating gap) that enables guiding of surface plasmons over micron distances. The large fields inside of the low index spacer layer can be understood in terms of continuity of the displacement current at the

interface between two materials which demands a high normal component of the electric field in the spacer, thus enabling the spacer layer to behave like a capacitor for the field. Furthermore, using coupled mode theory, the new hybrid modes can be modeled as a superposition of the nanowire and SP modes[92], highlighting the potential synergy between these two types of electromagnetic modes.

Returning to the experimental realization of this system, hybrid nanowire waveguided/surface plasmon modes are excited by the photoluminescence from CdS. The high mode volumes associated with the hybrid modes in conjunction with modal overlap in the CdS gain medium results in plasmon-enhanced laser action from CdS (Figure 1.8b) at the CdS I_2 exciton line. More importantly, for small nanowire sizes near ~150 nm the bare CdS nanowire does not exhibit lasing due to decreasing mode confinement (and thus poor overlap with the gain medium) with decreasing nanowire size. This effect was also demonstrated in studies of waveguided modes in bare ZnSe nanowires where single-mode operation was shown at nanowire diameters as small as $\lambda/9$, but with increasing leakage of the mode outside of the nanowire with decreasing diameter.[93] Indeed, the pump threshold intensity for bare CdS increases asymptotically at ~d=150 nm (Figure 1.8c), whereas the plasmonic system demonstrates lasing and thus experimentally attainable threshold values down to d=50 nm, the experimental limit of the sample size distribution. The plasmonic system is also associated with about ~6 times faster spontaneous emission (See Figure 1.8d) as expected from the previous discussion on metals interfaced with active materials (sections 1.2 and 1.3). It should be noted that in addition to lasing from CdS below the photonic "cutoff", the polarization of the laser

light from the plasmonic system is that of the surface plasmon mode (parallel to the nanowire long axis), which is also the polarization of the hybrid mode and is orthogonal to that of lasing from the bare nanowire, as the photonic modes involved have polarization perpendicular to the nanowire long axis.[31]

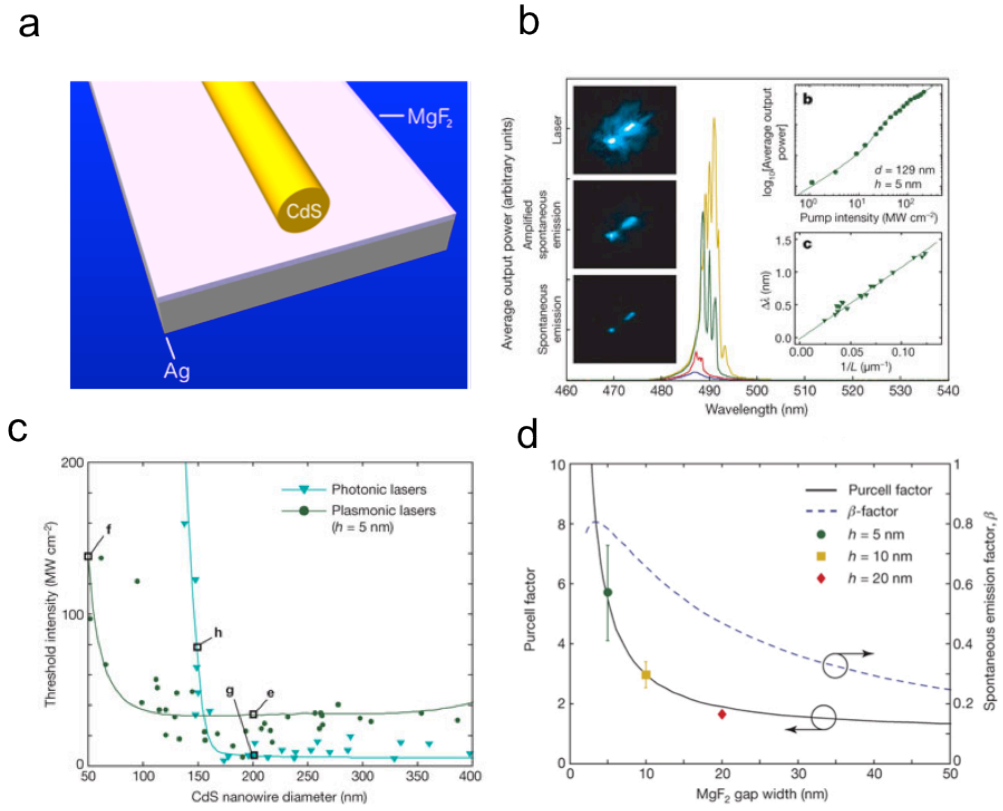

Figure 1.8 | Lasing from CdS nanowire interfaced with Ag film. (a) Schematic of CdS-on-Ag film geometry. b) photoluminescence spectrum of plasmonically-coupled CdS demonstrating lasing action at the I_2 exciton line. (inset, left: transition from spontaneous emission to lasing; inset, right: power dependence of emission and mode spacing vs. length corresponding to an effective index of 11). c) Threshold intensity vs. nanowire diameter demonstrating lasing in plasmonically-coupled CdS below the photonic lasing cutoff. d) Purcell enhancement for plasmonically-coupled CdS.[31] [Adapted from Reference 30]

References

1 Hecht, E. *Optics*. 4th edn, (Addison-Wesley, 2001).

2 Purcell, E. M. Spontaneous Emission Probabilities at Radio Frequencies. *Physical Review* **69**, 681-681 (1946).

3 Marcuse, D. *Theory of Dielectric Optical Waveguides*. (Academic Press, 1974).

4 Ryu, H. Y. & Notomi, M. Enhancement of spontaneous emission from the resonant modes of a photonic crystal slab single-defect cavity. *Optics Letters* **28**, 2390-2392, doi:Doi 10.1364/Ol.28.002390 (2003).

5 Giannini, V., Fernandez-Dominguez, A. I., Heck, S. C. & Maier, S. A. Plasmonic Nanoantennas: Fundamentals and Their Use in Controlling the Radiative Properties of Nanoemitters. *Chem Rev* **111**, 3888-3912, doi:Doi 10.1021/Cr1002672 (2011).

6 Adachi, S. *Properties of Group-IV, III-V and II-VI Semiconductors*. (Wiley, 2005).

7 Vahala, K. J. Optical microcavities. *Nature* **424**, 839-846, doi:Doi 10.1038/Nature01939 (2003).

8 Khitrova, G., Gibbs, H. M., Kira, M., Koch, S. W. & Scherer, A. Vacuum Rabi splitting in semiconductors. *Nat Phys* **2**, 81-90 (2006).

9 Peter, E. *et al.* Exciton-Photon Strong-Coupling Regime for a Single Quantum Dot Embedded in a Microcavity. *Physical Review Letters* **95**, 067401 (2005).

10 Armani, D. K., Kippenberg, T. J., Spillane, S. M. & Vahala, K. J. Ultra-high-Q toroid microcavity on a chip. *Nature* **421**, 925-928, doi:Doi 10.1038/Nature01371 (2003).

11 Burke, J., Stegeman, G. & Tamir, T. Surface-polariton-like waves guided by thin, lossy metal films. *Physical Review B* **33**, 5186 (1986).

12 Maier, S. A. *Plasmonics: Fundamentals and Applications*. (Springer, 2007).

13 Xu, H. X., Aizpurua, J., Kall, M. & Apell, P. Electromagnetic contributions to single-molecule sensitivity in surface-enhanced Raman scattering. *Physical Review E* **62**, 4318-4324, doi:Doi 10.1103/Physreve.62.4318 (2000).

14 Muhlschlegel, P., Eisler, H. J., Martin, O. J. F., Hecht, B. & Pohl, D. W. Resonant optical antennas. *Science* **308**, 1607-1609, doi:Doi 10.1126/Science.1111886 (2005).

15 Kinkhabwala, A. *et al.* Large single-molecule fluorescence enhancements produced by a bowtie nanoantenna. *Nature Photonics* **3**, 654-657, doi:Doi 10.1038/Nphoton.2009.187 (2009).

16 Kneipp, K. *et al.* Single molecule detection using surface-enhanced Raman scattering (SERS). *Phys Rev Lett* **78**, 1667-1670, doi:DOI 10.1103/PhysRevLett.78.1667 (1997).

17 Nie, S. M. & Emery, S. R. Probing single molecules and single nanoparticles by surface-enhanced Raman scattering. *Science* **275**, 1102-1106, doi:DOI 10.1126/science.275.5303.1102 (1997).

18 Hirsch, L. R. *et al.* Nanoshell-mediated near-infrared thermal therapy of tumors under magnetic resonance guidance. *Proceedings of the National Academy of Sciences* **100**, 13549-13554, doi:10.1073/pnas.2232479100 (2003).
19 Atwater, H. A. & Polman, A. Plasmonics for improved photovoltaic devices. *Nat Mater* **9**, 205-213 (2010).
20 Alu, A. & Engheta, N. Achieving transparency with plasmonic and metamaterial coatings. *Phys Rev E* **72**, doi:Doi 10.1103/Physreve.72.016623 (2005).
21 Brongersma, M. L. & Shalaev, V. M. The Case for Plasmonics. *Science* **328**, 440-441, doi:10.1126/science.1186905 (2010).
22 Quinten, M., Leitner, A., Krenn, J. R. & Aussenegg, F. R. Electromagnetic energy transport via linear chains of silver nanoparticles. *Opt. Lett.* **23**, 1331-1333 (1998).
23 Bozhevolnyi, S. I., Volkov, V. S., Devaux, E. & Ebbesen, T. W. Channel Plasmon-Polariton Guiding by Subwavelength Metal Grooves. *Physical Review Letters* **95**, 046802 (2005).
24 Mühlschlegel, P., Eisler, H.-J., Martin, O. J. F., Hecht, B. & Pohl, D. W. Resonant Optical Antennas. *Science* **308**, 1607-1609, doi:10.1126/science.1111886 (2005).
25 Oulton, R. F., Sorger, V. J., Genov, D. A., Pile, D. F. P. & Zhang, X. A hybrid plasmonic waveguide for subwavelength confinement and long-range propagation. *Nat Photon* **2**, 496-500 (2008).
26 Krasavin, A. V. & Zheludev, N. I. Active plasmonics: Controlling signals in Au/Ga waveguide using nanoscale structural transformations. *Applied Physics Letters* **84**, 1416-1418 (2004).
27 Kuhn, S., Hakanson, U., Rogobete, L. & Sandoghdar, V. Enhancement of single-molecule fluorescence using a gold nanoparticle as an optical nanoantenna. *Physical Review Letters* **97**, doi:Doi 10.1103/Physrevlett.97.017402 (2006).
28 Cho, C.-H., Aspetti C. O., *et al.* Tailoring hot-exciton emission and lifetimes in semiconducting nanowires via whispering-gallery nanocavity plasmons. *Nat Mater* **10**, 669-675 (2011).
29 Cho, C.-H., Aspetti, C. O., Park, J. & Agarwal, R. Silicon coupled with plasmon nanocavities generates bright visible hot luminescence. *Nat Photon* **7**, 285-289 (2013).
30 Akimov, A. V. *et al.* Generation of single optical plasmons in metallic nanowires coupled to quantum dots. *Nature* **450**, 402-406, doi:Doi 10.1038/Nature06230 (2007).
31 Oulton, R. F. *et al.* Plasmon lasers at deep subwavelength scale. *Nature* **461**, 629-632 (2009).
32 Frank L. Pedrotti, L. S. P., Leno M. Pedrotti. *Introduction to Optics*. 3rd edn, (Pearson Addison Wesley, 2007).
33 Kittel, C. & McEuen, P. *Introduction to solid state physics*. 8th edn, (J. Wiley, 2005).
34 Neogi, A. *et al.* Enhancement of spontaneous recombination rate in a quantum well by resonant surface plasmon coupling. *Physical Review B* **66**, 153305 (2002).

35 Okamoto, K. *et al.* Surface-plasmon-enhanced light emitters based on InGaN quantum wells. *Nat Mater* **3**, 601-605 (2004).
36 Song, J.-H., Atay, T., Shi, S., Urabe, H. & Nurmikko, A. V. Large Enhancement of Fluorescence Efficiency from CdSe/ZnS Quantum Dots Induced by Resonant Coupling to Spatially Controlled Surface Plasmons. *Nano Letters* **5**, 1557-1561, doi:10.1021/nl050813r (2005).
37 Ma, R.-M., Oulton, R. F., Sorger, V. J., Bartal, G. & Zhang, X. Room-temperature sub-diffraction-limited plasmon laser by total internal reflection. *Nat Mater* **10**, 110-113 (2011).
38 Sorger, V. J. *et al.* Strongly Enhanced Molecular Fluorescence inside a Nanoscale Waveguide Gap. *Nano Letters* **11**, 4907-4911, doi:Doi 10.1021/Nl202825s (2011).
39 Jun, Y. C., Huang, K. C. Y. & Brongersma, M. L. Plasmonic beaming and active control over fluorescent emission. *Nat Commun* **2**, doi:Doi 10.1038/Ncomms1286 (2011).
40 Barnes, W. L., Dereux, A. & Ebbesen, T. W. Surface plasmon subwavelength optics. *Nature* **424**, 824-830, doi:Doi 10.1038/Nature01937 (2003).
41 Biagioni, P., Huang, J. S. & Hecht, B. Nanoantennas for visible and infrared radiation. *Reports on Progress in Physics* **75**, doi:Doi 10.1088/0034-4885/75/2/024402 (2012).
42 Ming, T., Chen, H. J., Jiang, R. B., Li, Q. & Wang, J. F. Plasmon-Controlled Fluorescence: Beyond the Intensity Enhancement. *J Phys Chem Lett* **3**, 191-202, doi:Doi 10.1021/Jz201392k (2012).
43 Schuller, J. A. *et al.* Plasmonics for extreme light concentration and manipulation. *Nature Materials* **9**, 193-204, doi:Doi 10.1038/Nmat2630 (2010).
44 K. H. Drexhage, H. K., F. P. Schäfer. Variation of the Fluorescence Decay Time of a Molecule in Front of a Mirror. *Berichte der Bunsengesellschaft für physikalische Chemie* **72**, 329 (1968).
45 Siiman, O. & Lepp, A. Protonation of the Methyl-Orange Derivative of Aspartate Adsorbed on Colloidal Silver - a Surface-Enhanced Resonance Raman-Scattering and Fluorescence Emission Study. *J Phys Chem-Us* **88**, 2641-2650, doi:Doi 10.1021/J150656a043 (1984).
46 Rubim, J. C., Gutz, G. R. & Sala, O. Surface-Enhanced Raman-Scattering (Sers) and Fluorescence-Spectra from Mixed Copper(I)/Pyridine Iodide Complexes on a Copper Electrode. *Chem Phys Lett* **111**, 117-122, doi:Doi 10.1016/0009-2614(84)80447-9 (1984).
47 Pockrand, I., Brillante, A. & Mobius, D. Nonradiative Decay of Excited Molecules near a Metal-Surface. *Chem Phys Lett* **69**, 499-504, doi:Doi 10.1016/0009-2614(80)85113-X (1980).
48 Eagen, C. F., Weber, W. H., Mccarthy, S. L. & Terhune, R. W. Time-Dependent Decay of Surface-Plasmon-Coupled Molecular Fluorescence. *Chem Phys Lett* **75**, 274-277, doi:Doi 10.1016/0009-2614(80)80512-4 (1980).
49 Anger, P., Bharadwaj, P. & Novotny, L. Enhancement and quenching of single-molecule fluorescence. *Phys Rev Lett* **96**, doi:Artn 113002

Doi 10.1103/Physrevlett.96.113002 (2006).
50 Biteen, J. S., Pacifici, D., Lewis, N. S. & Atwater, H. A. Enhanced radiative emission rate and quantum efficiency in coupled silicon nanocrystal-nanostructured gold emitters. *Nano Letters* **5**, 1768-1773, doi:Doi 10.1021/Nl051207z (2005).
51 Chen, Y., Munechika, K. & Ginger, D. S. Dependence of fluorescence intensity on the spectral overlap between fluorophores and plasmon resonant single silver nanoparticles. *Nano Lett* **7**, 690-696, doi:Doi 10.1021/Nl062795z (2007).
52 Muskens, O. L., Giannini, V., Sanchez-Gil, J. A. & Rivas, J. G. Strong enhancement of the radiative decay rate of emitters by single plasmonic nanoantennas. *Nano Lett* **7**, 2871-2875, doi:Doi 10.1021/Nl0715847 (2007).
53 Bakker, R. M. *et al.* Enhanced localized fluorescence in plasmonic nanoantennae. *Applied Physics Letters* **92**, doi:Doi 10.1063/1.2836271 (2008).
54 Noginov, M. A. *et al.* Demonstration of a spaser-based nanolaser. *Nature* **460**, 1110-U1168, doi:Doi 10.1038/Nature08318 (2009).
55 Dong, Z. C. *et al.* Generation of molecular hot electroluminescence by resonant nanocavity plasmons. *Nat Photonics* **4**, 50-54, doi:Doi 10.1038/Nphoton.2009.257 (2010).
56 Hofmann, C. E., de Abajo, F. J. G. & Atwater, H. A. Enhancing the Radiative Rate in III-V Semiconductor Plasmonic Core-Shell Nanowire Resonators. *Nano Lett* **11**, 372-376, doi:Doi 10.1021/Nl102878b (2011).
57 Okamoto, K. *et al.* Surface plasmon enhanced spontaneous emission rate of InGaN/GaN quantum wells probed by time-resolved photoluminescence spectroscopy. *Applied Physics Letters* **87**, doi:Doi 10.1063/1.2010602 (2005).
58 Jun, Y. C., Kekatpure, R. D., White, J. S. & Brongersma, M. L. Nonresonant enhancement of spontaneous emission in metal-dielectric-metal plasmon waveguide structures. *Physical Review B* **78**, doi:Doi 10.1103/Physrevb.78.153111 (2008).
59 Bergman, D. J. & Stockman, M. I. Surface Plasmon Amplification by Stimulated Emission of Radiation: Quantum Generation of Coherent Surface Plasmons in Nanosystems. *Physical Review Letters* **90**, 027402 (2003).
60 Oulton, R. Surface plasmon lasers: sources of nanoscopic light. *Materials Today* **15**, 26 (2012).
61 Pockrand, I., Swalen, J. D., Gordon, J. G. & Philpott, M. R. Exciton-Surface Plasmon Interactions. *J Chem Phys* **70**, 3401-3408, doi:Doi 10.1063/1.437872 (1979).
62 Bellessa, J., Bonnand, C., Plenet, J. C. & Mugnier, J. Strong coupling between surface plasmons and excitons in an organic semiconductor. *Physical Review Letters* **93**, doi:Doi 10.1103/Physrevlett.93.036404 (2004).
63 Bellessa, J. *et al.* Exciton/plasmon polaritons in GaAs/Al(0.93)Ga(0.07)As heterostructures near a metallic layer. *Physical Review B* **78**, doi:Doi 10.1103/Physrevb.78.205326 (2008).
64 Bellessa, J. *et al.* Giant Rabi splitting between localized mixed plasmon-exciton states in a two-dimensional array of nanosize metallic disks in an organic

semiconductor. *Physical Review B* **80**, doi:Doi 10.1103/Physrevb.80.033303 (2009).

65 Gomez, D. E., Vernon, K. C., Mulvaney, P. & Davis, T. J. Surface Plasmon Mediated Strong Exciton-Photon Coupling in Semiconductor Nanocrystals. *Nano Letters* **10**, 274-278, doi:Doi 10.1021/Nl903455z (2010).

66 Klingshirn, C. F. *Semiconductor Optics*. 3 edn, (Springer-Verlag, 2007).

67 Achermann, M. Exciton-Plasmon Interactions in Metal-Semiconductor Nanostructures. *J Phys Chem Lett* **1**, 2837-2843, doi:Doi 10.1021/Jz101102e (2010).

68 Duan, X. F. & Lieber, C. M. General synthesis of compound semiconductor nanowires. *Advanced Materials* **12**, 298-302, doi:Doi 10.1002/(Sici)1521-4095(200002)12:4<298::Aid-Adma298>3.0.Co;2-Y (2000).

69 Li, Y., Qian, F., Xiang, J. & Lieber, C. M. Nanowire electronic and optoelectronic devices. *Materials Today* **9**, 18-27, doi:Doi 10.1016/S1369-7021(06)71650-9 (2006).

70 Yan, R. X., Gargas, D. & Yang, P. D. Nanowire photonics. *Nature Photonics* **3**, 569-576, doi:Doi 10.1038/Nphoton.2009.184 (2009).

71 Duan, X. F., Huang, Y., Cui, Y., Wang, J. F. & Lieber, C. M. Indium phosphide nanowires as building blocks for nanoscale electronic and optoelectronic devices. *Nature* **409**, 66-69, doi:Doi 10.1038/35051047 (2001).

72 Xiang, J. *et al.* Ge/Si nanowire heterostructures as high-performance field-effect transistors. *Nature* **441**, 489-493 (2006).

73 Yan, H. *et al.* Programmable nanowire circuits for nanoprocessors. *Nature* **470**, 240-244, doi:Doi 10.1038/Nature09749 (2011).

74 Patolsky, F. *et al.* Detection, stimulation, and inhibition of neuronal signals with high-density nanowire transistor arrays. *Science* **313**, 1100-1104, doi:Doi 10.1126/Science.1128640 (2006).

75 Kim, W., Ng, J. K., Kunitake, M. E., Conklin, B. R. & Yang, P. D. Interfacing silicon nanowires with mammalian cells. *Journal of the American Chemical Society* **129**, 7228-+, doi:Doi 10.1021/Ja071456k (2007).

76 W. Snyder, J. D. L. *Optical Waveguide Theory*. (Chapman and Hall, 1983).

77 van Vugt, L. K., Zhang, B., Piccione, B., Spector, A. A. & Agarwal, R. Size-Dependent Waveguide Dispersion in Nanowire Optical Cavities: Slowed Light and Dispersionless Guiding. *Nano Lett.* **9**, 1684-1688, doi:10.1021/nl900371r (2009).

78 Hayden, O., Agarwal, R. & Lieber, C. M. Nanoscale avalanche photodiodes for highly sensitive and spatially resolved photon detection. *Nat Mater* **5**, 352-356 (2006).

79 Sirbuly, D. J., Tao, A., Law, M., Fan, R. & Yang, P. Multifunctional Nanowire Evanescent Wave Optical Sensors. *Advanced Materials* **19**, 61-66, doi:10.1002/adma.200601995 (2007).

80 Johnson, J. C. *et al.* Single gallium nitride nanowire lasers. *Nat Mater* **1**, 106-110, doi:Doi 10.1038/Nmat728 (2002).

81 Agarwal, R., Barrelet, C. J. & Lieber, C. M. Lasing in single cadmium sulfide nanowire optical cavities. *Nano Letters* **5**, 917-920, doi:Doi 10.1021/Nl050440u (2005).
82 Duan, X. F., Huang, Y., Agarwal, R. & Lieber, C. M. Single-nanowire electrically driven lasers. *Nature* **421**, 241-245, doi:Doi 10.1038/Nature01353 (2003).
83 Cao, L. Y. *et al.* Engineering light absorption in semiconductor nanowire devices. *Nat Mater* **8**, 643-647, doi:Doi 10.1038/Nmat2477 (2009).
84 Nobis, T., Kaidashev, E. M., Rahm, A., Lorenz, M. & Grundmann, M. Whispering gallery modes in nanosized dielectric resonators with hexagonal cross section. *Physical Review Letters* **93**, doi:Doi 10.1103/Physrevlett.93.103903 (2004).
85 Law, M., Greene, L. E., Johnson, J. C., Saykally, R. & Yang, P. D. Nanowire dye-sensitized solar cells. *Nat Mater* **4**, 455-459, doi:Doi 10.1038/Nmat1387 (2005).
86 Cao, L. Y. *et al.* Semiconductor Nanowire Optical Antenna Solar Absorbers. *Nano Letters* **10**, 439-445, doi:Doi 10.1021/Nl9036627 (2010).
87 van Vugt, L. K., Piccione, B. & Agarwal, R. Incorporating polaritonic effects in semiconductor nanowire waveguide dispersion. *Applied Physics Letters* **97**, 061115 (2010).
88 Piccione, B., Agarwal, R., Jung, Y. & Agarwal, R. Size-dependent chemical transformation, structural phase change, and optical properties of nanowires. *Philos Mag* **93**, 2089-2121, doi:Doi 10.1080/14786435.2013.765981 (2013).
89 Brian Piccione, Carlos O. Aspetti., Chang-Hee Cho, Ritesh Agarwal. Tailoring light-matter coupling in semiconductor and hybrid-plasmonic nanowires. *Reports on Progress in Physics* **77**, 1-20 (2014).
90 van Vugt, L. K., Piccione, B., Cho, C.-H., Nukala, P. & Agarwal, R. One-dimensional polaritons with size-tunable and enhanced coupling strengths in semiconductor nanowires. *Proceedings of the National Academy of Sciences* **108**, 10050-10055, doi:10.1073/pnas.1102212108 (2011).
91 Piccione, B., Cho, C. H., van Vugt, L. K. & Agarwal, R. All-optical active switching in individual semiconductor nanowires. *Nature Nanotechnology* **7**, 640-645, doi:Doi 10.1038/Nnano.2012.144 (2012).
92 Oulton, R. F., Sorger, V. J., Genov, D. A., Pile, D. F. P. & Zhang, X. A hybrid plasmonic waveguide for subwavelength confinement and long-range propagation. *Nature Photonics* **2**, 496-500, doi:Doi 10.1038/Nphoton.2008.131 (2008).
93 van Vugt, L. K., Zhang, B., Piccione, B., Spector, A. A. & Agarwal, R. Size-Dependent Waveguide Dispersion in Nanowire Optical Cavities: Slowed Light and Dispersionless Guiding. *Nano Letters* **9**, 1684-1688, doi:Doi 10.1021/Nl900371r (2009).

Chapter 2. Growth and Characterization of Single-Crystalline and Surface Passivated CdS Nanowires

The nanowires used in the experiments presented in this thesis are composed of either cadmium sulfide, a direct-band gap semiconductor (see Chapters 3 and 6), or silicon, an indirect-band gap semiconductor (see Chapters 4 and 5). Though the silicon nanowires were commercially obtained, the CdS nanowires were all grown in-house, and both nanowire types were grown via the Vapor-Liquid-Solid (VLS) method. Therefore, we will briefly review VLS growth. Furthermore, CdS was the test bed initially used to explore surface-plasmon based engineering of semiconductor optics, which formed our understanding of the physics behind surface-plasmon enhanced light emission from semiconductors and, which also led to the development of several sample design standards. As such, in this section we will also present an overview relevant physical properties and morphology of our CdS nanowires (further supplemented in chapter 3).

2.1: Overview of Vapor Liquid Solid Method

Nanowires may be synthesized by a variety of top-down and bottom-up methods including (but not limited to) selective chemical etching,[1] solution-based synthesis,[2] molecular beam epitaxy (MBE),[3] and vapor-liquid-solid (VLS) growth.[3] These methods have distinct advantages and disadvantages, for example selective etching yields all the control garnered from traditional top-down electronic micro-fabrication (such as

placement and dimensions). Solution based techniques have high yield with controlled size distributions and high-surface quality. However, when high crystalline quality (leading to optimal optical, electrical and thermal conduction) is required, MBE and VLS methods yield the most consistent results, albeit with less controlled placement on the growth substrate and with a degree of size poly-dispersity.

Due to ease of implementation the VLS method is used for all nanowires used in this thesis. VLS is basically a three-step process (Figure 2.1): first a catalyst particle, such as Au, is deposited over the growth substrate and heated to a melt. The semiconductor precursor is then introduced into the chamber and heated above the eutectic temperature of catalyst-semiconductor system. After the alloy reaches supersaturation, precursor precipitates at the catalyst/substrate interface resulting in nanowire growth.[3] Another great advantage is that VLS growth does not require that the growth substrate be lattice matched to the NW, a combination of kinetics and thermodynamics of the NW surface are the biggest determining factors in the final growth phase.

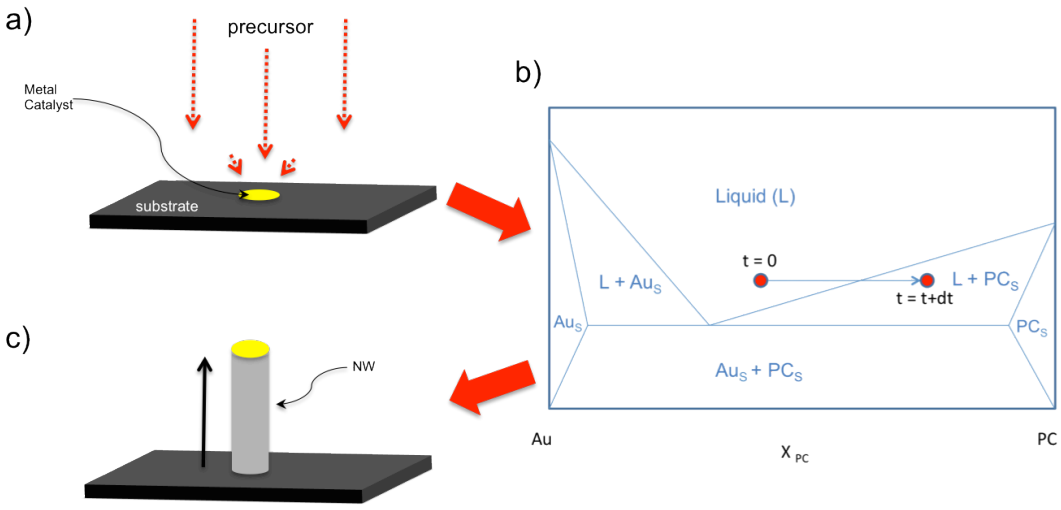

Figure 2.1 | Schematic of VLS process described in three steps. a) Precursor (PC) comes into contact with catalyst particle above the eutectic temperature. b) Fictitious binary phase diagram demonstrating supersaturation of catalyst with time. c) Solid precursor is precipitated at the catalyst-substrate interface leading to vertical nanowire growth.

2.2: Growth of Cadmium Sulfide Nanowires: Experimental Procedure

CdS nanowires were grown by via the VLS method as mentioned above. First, a 5 nm Au film was plasma-sputter coated onto a Si substrate and annealed at 790 C for 5 minutes to form gold islands (these serve as catalyst particles for VLS growth). The substrate was placed on one end of a quartz tube furnace. Pure CdS powder (99.999% purity, Sigma Aldrich) was loaded into a quartz tube furnace at the tube center. Precursor is transported to the growth substrate using 100 sccm of Argon as a carrier gas. During growth, the quartz growth chamber was maintained at a temperature of 760 C and a pressure of 300 milliTorr using an auto vacuum system. The resulting nanowires are

generally single crystalline and grow in the wurtzite phase (Figure 3.1). After 3 hours of growth, we generally see diameters in the range 100-300 nm and an average length of ~15 microns.

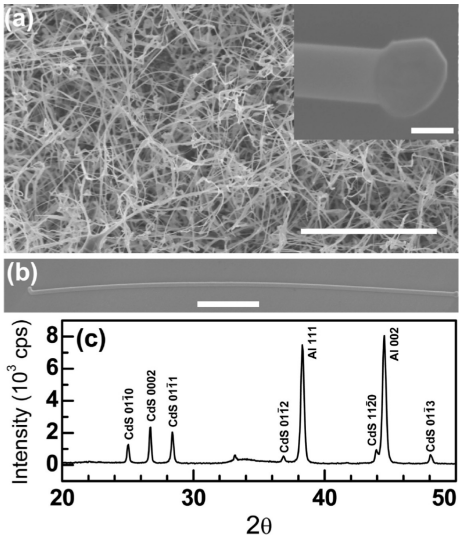

Figure 2.2 | a) SEM micrograph of nanowire growth substrate (1 micron scale bar), (inset: tip of nanowire and catalyst particle, 100 nm scale bar). b) SEM micrograph of individual nanowire on substrate used for optical measurement. c) X-ray diffraction dat for CdS nanowire growth substrate in (a).[4]

2.3: Optical Characterization

The VLS-grown CdS nanowires used in the following studies feature high optical quality, whereby they exhibit high-intensity waveguiding (Figure 2.3) and free exciton emission (Figure 2.4a). As expected in structures at the nanoscale, surface plays an important role in dictating the physical properties. In the case of the optical properties of CdS, trap states and dangling bonds at the surface can serve as scattering centers for

excitons[5] (see section 1.4 for discussion on the exciton in semiconductors), providing a fast non-radiative decay channel.[6] This results in both decreased photoluminescence intensity[6] and light emission (photoluminescence) at lower energies[4] (see figure 2.4a, red curve). Passivation of the surface with a 5 nm SiO_2 coating results in free A and B exciton emission from CdS (figure 2.4a, blue curve), which is in agreement with literature values and implies that majority of emission from CdS now comes from the bulk as opposed to scattering from the surface.[4]

As discussed above, producing CdS nanowires of the highest optical quality is dependent on the treatment of the surface. Upstanding CdS nanowires were coated with 5 nm of SiO_2 using Atomic Layer Deposition (Cambridge Nanotech) and alternating pulses of O_3, (3-aminopropyl) triethoxysilane, and H_2O. The physical and chemical morphology of the coating was confirmed via Transmission Electron Microscopy (TEM) (Figure 2.4b, top) and Fourier Transform Infrared Spectroscopy (FTIR) (Figure 2.4b, bottom) respectively. TEM reveals an uniform 5nm SiO_2 coating. FTIR demonstrates a stark change in the surface chemistry of the nanowire, where surface dangling bonds, known to serve as exciton binding sites (as discussed above) are passivated via formation of metal-sulfate bonds. Dangling bonds at the surface may serve as exciton scattering sites, yet as demonstrated by photoluminescence (PL) spectroscopy, passivation results in a clear to transition to nearly complete free-excitonic emission with peaks at the characteristic A (2.5444) and B (2.5597) exciton energies[7] (Figure 2.4, blue curve).

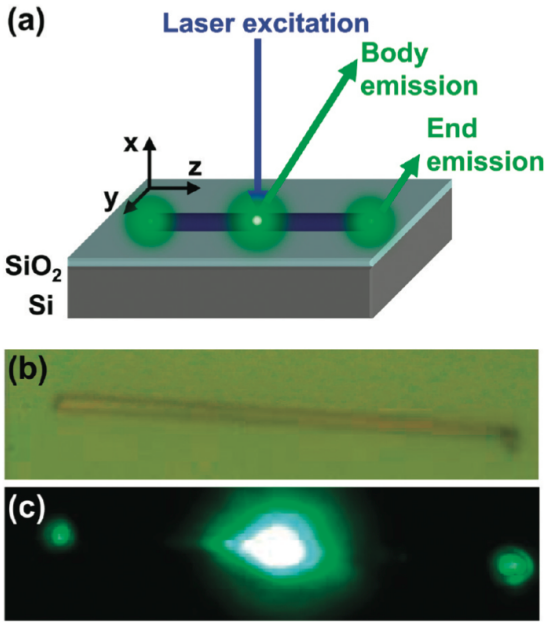

Figure 2.3 | a) Schematic of experimental setup involving pumping of CdS nanowire above the band-gap and both body and end-emission. b) Optical image of nanowire on measurement substrate. c) Same nanowire as (a) under laser excitation.[4]

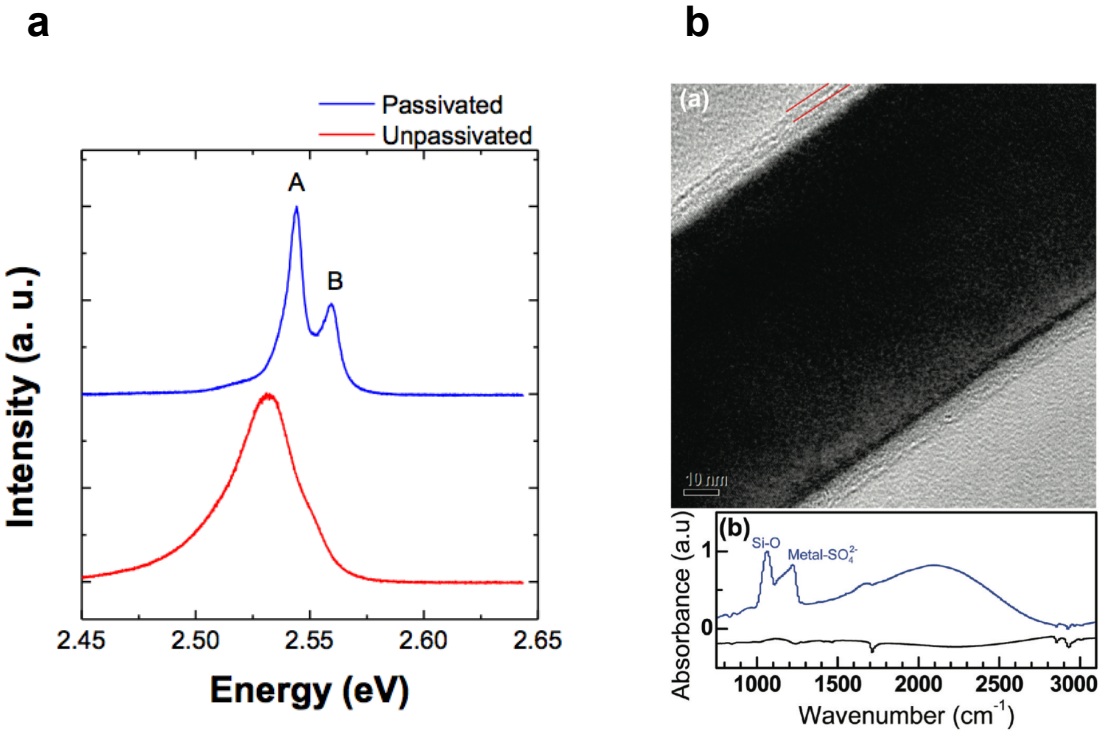

Figure 2.4 | Optical and morphological properties of VLS grown CdS nanowires. a) Photoluminescence spectrum of unpassivated CdS nanowire (red curve) and SiO_2-passivated CdS nanowire (blue curve).[8] b) Transmission electron microscope micrograph of CdS nanowire coated with 5 nm of SiO_2 (top panel) and FTIR spectrum of uncoated CdS nanowire (bottom panel, black curve) and passivated nanowire (bottom panel, blue curve).[4]

References

1 Katouf, R. *et al.* Ultrahigh relative refractive index contrast GaAs nanowire waveguides. *Appl. Phys. Express* **1**, 122101 (2008).

2 Choy, J. H. *et al.* Soft solution route to directionally grown ZnO nanorod arrays on Si wafer; room-temperature ultraviolet laser. *Advanced Materials* **15**, 1911-+, doi:Doi 10.1002/Adma.200305327 (2003).

3 Yi, G.-C. *Semiconductor nanostructures for optoelectronic devices: processing, characterization, and applicatons*. (Springer, 2012).

4 van Vugt, L. K. *et al.* Variable Temperature Spectroscopy of As-Grown and Passivated CdS Nanowire Optical Waveguide Cavities. *The Journal of Physical Chemistry A* **115**, 3827-3833, doi:10.1021/jp108167t (2011).

5 van Vugt, L. K., Veen, S. J., Bakkers, E. P. A. M., Roest, A. L. & Vanmaekelbergh, D. Increase of the photoluminescence intensity of InP nanowires by photoassisted surface passivation. *Journal of the American Chemical Society* **127**, 12357-12362, doi:Doi 10.1021/Ja051860o (2005).

6 Liu, X. F., Zhang, Q., Xing, G. C., Xiong, Q. H. & Sum, T. C. Size-Dependent Exciton Recombination Dynamics in Single CdS Nanowires beyond the Quantum Confinement Regime. *J Phys Chem C* **117**, 10716-10722, doi:Doi 10.1021/Jp312850w (2013).

7 Klingshirn, C. F. *Semiconductor Optics*. 3 edn, (Springer-Verlag, 2007).

8 Cho, C.-H., Aspetti, C. O., *et al.* Tailoring hot-exciton emission and lifetimes in semiconducting nanowires via whispering-gallery nanocavity plasmons. *Nat Mater* **10**, 669-675 (2011).

Chapter 3. Highly Enhanced Spontaneous Emission Lifetimes and Light Absorption in Semiconducting Nanowires via Nanocavity Plasmons

3.1: Introduction

3.1.1: Motivation

Until this point, integration of active media with surface plasmons (SPs) has focused on either open geometries such as metal films and metal nanowires, which host surface plasmon polarition (SPP) modes and metal nanostructures which host localized surface plasmons (LSPs). Resonant optical cavities based on SP modes, on the other hand, should yield the sought-after combination of both high quality factor (Q) modes due to their closed architecture and low mode volumes normally associated with SP modes. Such a resonant cavity may be fabricated by "wrapping" the metal/insulator film around the nanowire core resulting in a core-shell semiconductor-metal cavity (discussed later). Using this resonant plasmonic-cavity architecture, we demonstrate unprecedented Purcell factors of $\sim 10^3$ in "bulk" CdS, that is CdS which is not quantum confined, based on spectral overall between the SPP modes of the plasmonic nanocavity and light emission from CdS.[1] With Purcell enhancements at this extreme level, the spectroscopic properties of the host material system are profoundly altered and will be discussed below.

Furthermore, though a significant portion of the discussion will be dedicated to the use of SP optical cavities to enhance light emitting properties, the reciprocal process is also explored here, whereby SP modes of the core-shell semiconductor-metal cavity are used to enable large enhancements in absorption of light, another important optical property. This SP-enhanced absorption would serve to produce devices that are highly enhanced optical antenna absorbers, with applications as more sensitive nanowire photodetectors[2-4] or even more efficient solar cells.[5]

3.1.2: Exciton Dynamics in CdS (and other Direct Bandgap Semiconductors)

In a direct bandgap semiconductor (e.g. CdS, with significant ionic character), intra-band relaxation of excited charge carriers occurs via scattering with longitudinal-optical (LO) phonons and acoustic phonons in approximately 0.1 ps and 100 ps respectively.[8] The conduction band minimum at k=0 is resonant with the light line (i.e. the photon dispersion: $\omega=ck$) at k~0, thus the photon state is both energy and momentum matched to the electronic state at k~0 and the electron may recombine radiatively (Figure 3.1, blue curves). This radiative recombination process occurs in ~1 ns and is generally much slower than the relaxation processes, (i.e. ~1000 times slower in this case).[8,9] This explains why CdS and other semiconductor materials mostly emit from the ground state, that is the material, under normal conditions, emits light from near the band edge. This phenomenon is well known in photochemistry where it has been described by "Kasha's Rule"; the emission spectrum of any molecule is independent of the excitation wavelength as emission always occurs from the lowest energy excited state.[7]

We note that Purcell enhancement of a semiconductor will lead to increased spontaneous emission (SE) in several systems as discussed above, and as reported in the CdS-on-Ag film structure (where the Purcell factor was ~6).[10] The key point here is that in all of the references on SP enhanced SE discussed thus far (see section 1.3), SE is restricted to emission near the band edge, again due to the discrepancy in timescales between intra-band relaxation and radiative recombination. On the other hand, if Purcell enhancement (or in other words the Q/V_m ratio) and thus the spontaneous emission rate can be pushed high enough (10^2-10^3 for a direct bandgap material like CdS) then, in theory, radiative recombination should become competitive with the relaxation process, which is ~10^3 times faster as discussed above. In theory, we should be able to break Kasha's rule. In order to explore highly enhanced spontaneous emission, CdS was interfaced with a plasmonic nanocavity as will be discussed below.

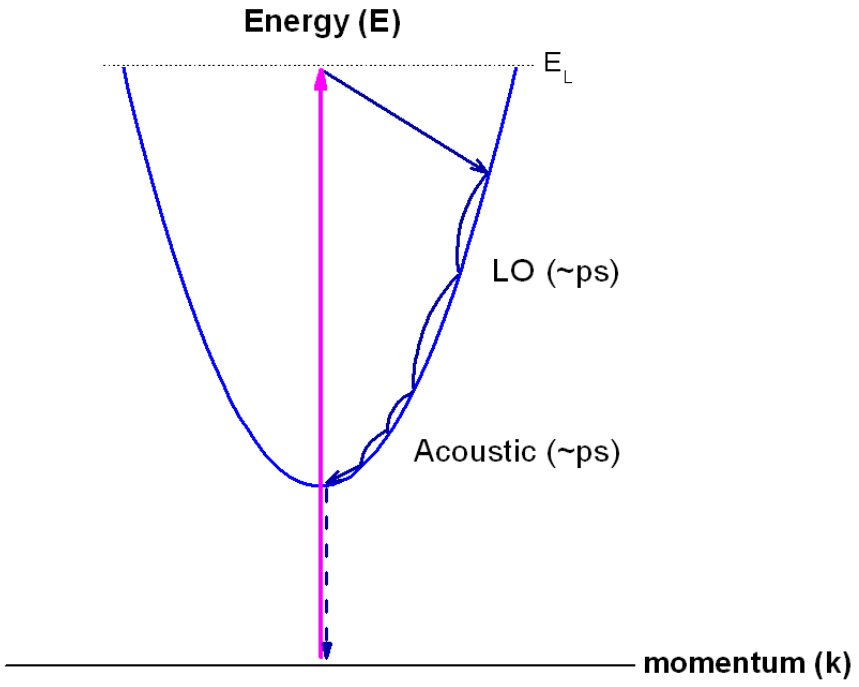

Figure 3.1 | Schematic of E vs. k dispersion relation for an exciton in CdS, depicting the exciton generation, relaxation, and emission process (dark blue curve). E_L denotes the laser excitation energy.

3.2: Synthesis and Characterization of Semiconductor-Metal-Insulator Core Shell Plasmonic Nanocavity

CdS semiconductor nanowires were grown in house following the methods expounded in Chapter 2 and subsequently coated with a layer of SiO_2 (5 nm) and a thin silver film (15 nm) to form a core-shell CdS-SiO_2-Ag structure (Figure 3.2a). Following nanowire growth on a silicon substrate, the substrate was transferred to an atomic layer deposition chamber (Cambridge Nanotech), where it was treated with and alternating

pulses of O_3, (3-aminopropyl) triethoxysilane, and H_2O resulting in 5 nm of SiO_2 on the surface. The uniformity of the coating was checked via transmission electron microscopy (TEM) and reveals a conformal shell around the entire nanowire (Figure 3.2b). It should be noted that VLS-grown CdS nanowires grow vertically on the growth substrate forming an upstanding "forest" of nanowires. This facilitates their uniform exposure to precursor during the surface treatment steps. Following SiO_2 deposition, the growth substrate was placed into an electron-beam evaporation chamber (Thermionics) and metallized at a very slow rate (0.2 Angstrom/second). Once again, TEM reveals a metal coating with a conformal morphology (Figure 3.2c). The uniformity of all coatings where further corroborated via elemental mapping with Energy Dispersive X-Ray Spectroscopy (Figure 3.2d).

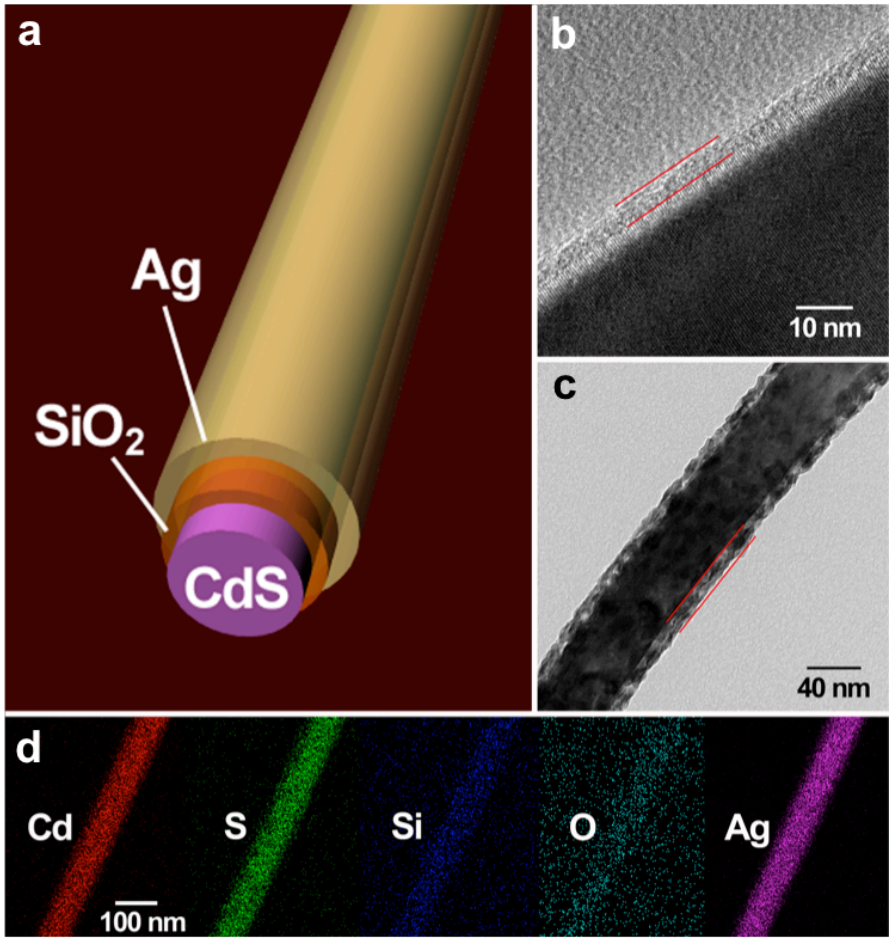

Figure 3.2 | Characterization of core-shell; CdS-SiO_2-Ag nanowire. a) Schematic of core-shell structure. b) TEM micrograph of ALD deposited SiO_2 passivation layer. c) TEM micrograph of 15 nm polycrystalline Ag coating. d) EDX elemental maps demonstrating conformal coatings of all species.[1]

3.3: Material Selection

CdS is an ideal material for this study due, first, to its intrinsically high quantum yield,[11] which enables it to serve as an excitation source for SPPs in the Ag film. Electron hole pairs in CdS also couple strongly to light due to the intrinsic high oscillator strength in CdS,[12] which leads to the formation of excitons that are stable up to room-temperature

(and certainly at the cryogenic temperatures used in this study). This results in well characterized free exciton emission in the photoluminescence spectrum of CdS[13] (see chapter 2). Finally, CdS features particularly high coupling strength between excitons and optical phonons in the crystal lattice. As will become apparent in subsequent sections, this phonon-exciton coupling, in addition to the high Purcell factors, is essential in mediating the anomalous photoluminescence from high energy states observed in CdS when coupled to high Q/V_m plasmonic nanocavities. To provide some perspective on this subsject, phonon-exciton coupling in CdS, also known as fröhlich coupling, is approximately 10 times higher than in GaAs, another important light emitting semiconductor.[14]

The SiO_2 interlayer serves three important functions. First, it serves to prevent non-radiative quenching of excited charge carriers by the metal as explained in work by Anger et al. (see section 1.3). It also plays a key role in developing low-loss hybrid electromagnetic modes of as explained in studies of Oulton et al[10] (see section 1.4.1). Finally, deposition of a SiO_2 layer on CdS has been established as a method to chemically passivate the surface of CdS and prevent exciton scattering at the surface thus promoting free exciton emission[15] (see chapter 2). The photoluminescence spectrum of a bare CdS nanowire (Figure 3.3a, blue curve) shows the traditional free A and B exciton emission in CdS.[16] Silver is used as the metal shell as it demonstrates the lowest losses in the visible range and is thus the best choice for plasmonics at optical frequency[17] (if we ignore chemical reactivity with the environment, in which case gold would be a superior choice).

3.4: Photoluminescence Measurements of Plasmonically-Coupled CdS

3.4.1: Experimental

Photoluminescence measurements were performed using a home-built laser-microscope-spectrometer setup. Light from the laser is fed through a x60, 0.7 NA objective (Nikon) with a spatial resolution of 500 nm. The 457.9 nm laser line of a continuous wave argon-ion laser (Coherent) was focused to a spot size of ~1 micron. Nanoscale silver can be quite susceptible to oxidation in atmosphere and degradation, thus nanowires were excited with low excitation power densities (<100 kW/cm^{-2}) to avoid sample heating. Photoluminescence was collected using a spectrometer (Acton) with 0.1 nm resolution and a cooled CCD (Pixis 2K, Princeton Instruments). Low temperature measurements were conducted using a nitrogen-cooled (Janis, ST-500) cryostat.

3.4.2: Initial Results

The photoluminescence spectra (taken at 77 K) of a bare (but SiO_2 passivated) CdS nanowire and nanowire coated with the silver shell is shown in Figure 3.3. The bare nanowire shows traditional A and B exciton emission, which is expected for CdS (see chapter 2). Upon addition of the metal shell there is an increase in the overall photoluminescence intensity by ~10x (Figure 3.4). Yet more interesting is the spectral shape which now features sharp peaks at multiples of the LO phonon energy in CdS (38 meV) above the free exciton emission (Figure 3.3a, magenta curve) and which correspond to radiative decay from previously characterized hot states in CdS.[18] In other

words, we observe light emission from states, which are above the grounds state. Photoluminescence measurements on different size (diameter) nanowires (Figure 3.4b) also reveal a clear size dependence in the intensity of hot luminescence peaks with a particularly marked effect when the 4th order hot luminescence peak (4-LO) is in resonance with the B-exciton position (2.556 eV), which hints at the role of cavity modes in mediating the emission process.

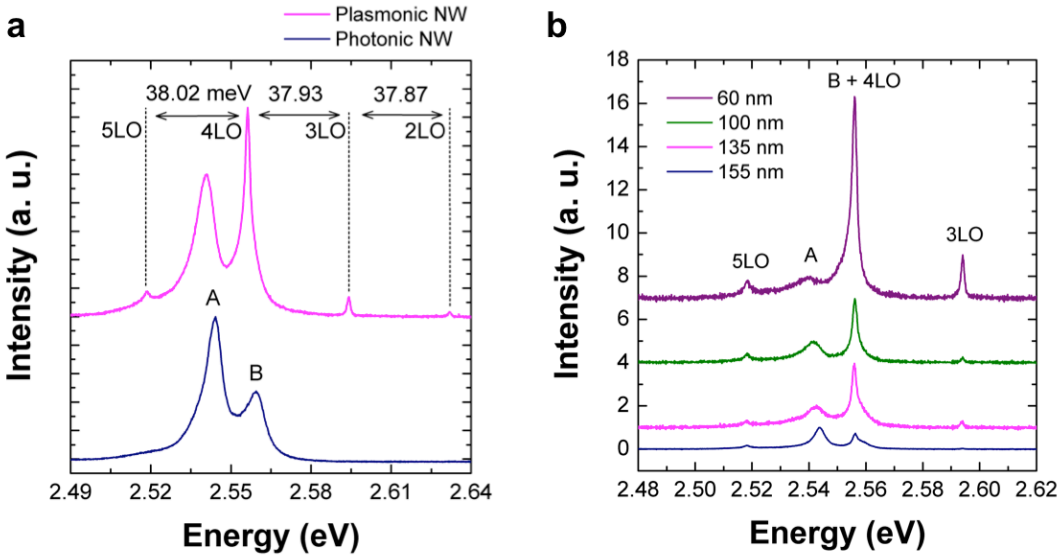

Figure 3.3 | a) Photoluminescence measurements at 77 K for metal-coated (magenta) and bare (blue) nanowires. b) Photoluminescence for metal-coated nanowires with different core diameters (legend: core nanowire diameter).[1]

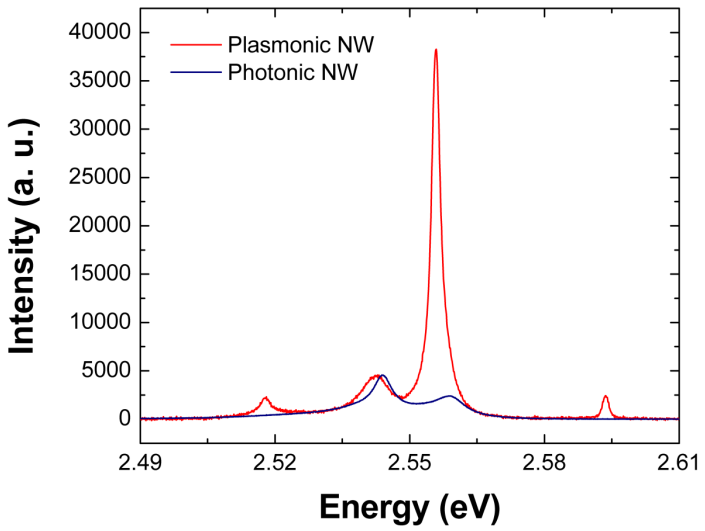

Figure 3.4 | Comparison between photoluminescence spectra of bare and passivated CdS nanowire (blue curve) and metal-coated CdS nanowire (red curve), both with diameter, d=60 nm. In order to provide a fair comparison of the photoluminescence intensities, we take into account both in-coupling and out-coupling through the thin silver film with respect to the bare nanowire. These were calculated to be 280% (enhancement) of the in-coupling and 5% (reduction) in out-coupling using Lumerical, a commercial Finite Difference Time Domain solver. Overall, a significant (~10x) increase in photon counts is observed for the metal-coated nanowire. The in-coupling enhancement is due to antenna effects whereas the decrease in out-coupling is due to ohmic losses.[1]

3.4.3: Results and Discussion

The occurrence of hot luminescence peaks points to either a substantial slowing of non-radiative decay process or an equally high increase in the radiative process. The latter process could occur as result of SPP resonances in the vicinity of free A and B exciton emission, which substantially increase the local photon density of states (LDOS) and thus increase the radiative rate of decay (or decrease the lifetime) via the Purcell effect as discussed in Chapter 1. Indeed, this Purcell enhancement would have to be at least 3 orders of magnitude to make the radiative (~ns) process competitive with the non-radiative (~ps) process (see section 3.1.2). Figure 3.5 is a representation of the proposed hot luminescence mechanism, where decay of the excited carrier to the conduction band and back to the light-line is mediated by the LO phonon, which again has energy equal to 38 meV. The enhancement of the 4-LO peak when resonant with the B-exciton peak is attributed to the rapid accumulation of excitons at the B-exciton state, which is the ground state, and which would not be able to decay much further (these carriers already have k near 0) and would likely recombine radiatively.

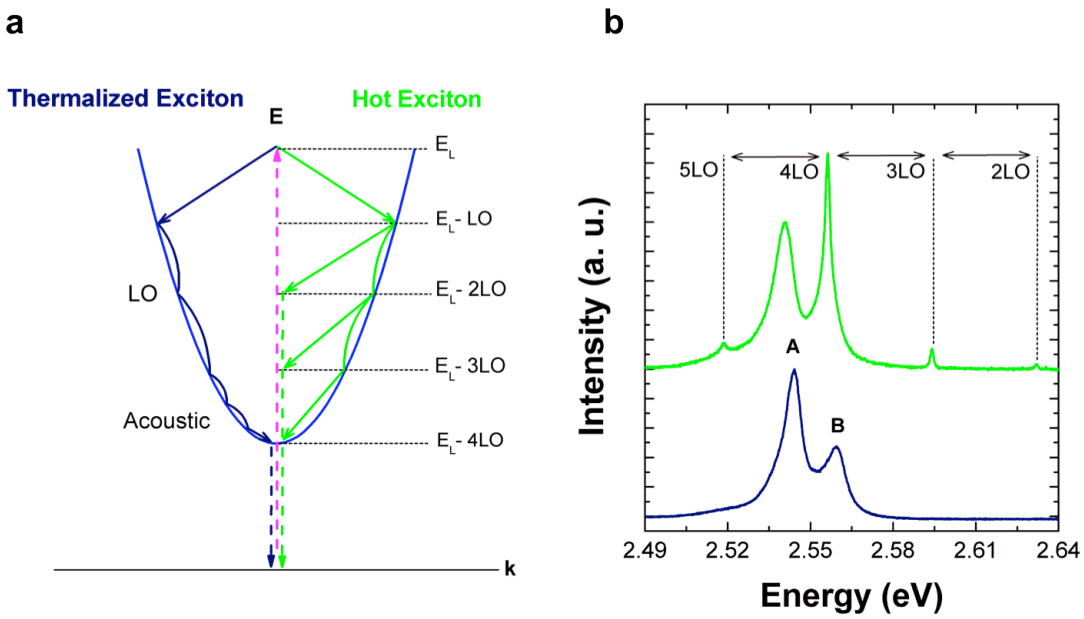

Figure 3.5 | a) Schematic of exciton generation, relaxation, and emission process for a thermalized exciton (blue curve, left) and non-thermalized (hot)-exciton (green curve, right) in CdS. E_L denotes the laser excitation energy. b) Photoluminescence spectra associated with the diagram in (a) (also plotted in figure 3.4) and following the same color code for a bare CdS nanowire (blue curve, bottom) and plasmonic-core shell CdS nanowire (green curve, top). The bare CdS nanowire shows emission from thermalized excitons while the metal-coated CdS nanowire cavity shows emission peaks corresponding to non-thermalized (hot) excitons.[1]

It should be noted that hot photoluminescence has similar spectral characteristics to Resonance Raman scattering (RRS), where light is also scattered at multiples of the LO-phonon energy. The fundamental difference between these two processes is that hot photoluminescence involves a real exciton state (i.e. excitation of the exciton to a high energy state followed by relaxation), whereas RRS is a single photon process.[19] Polarization dependent measurements provide evidence for the excitonic nature of our observed emission. The polarization-resolved photoluminescence in Figure 3.6, clearly

demonstrate a preferential polarization of the hot photoluminescence signal, which is not linked to the polarization of the incident light as would be the case in RRS.[20] Figure 3.6a shows typical A and B exciton polarizations, where the A-exciton is polarized perpendicular to the c-axis of the CdS wurtzite structure and the B-exciton is isotropic.[16] From the polarization of the A-exciton we determine that the nanowires are grown with the c-axis tilted approximately ~55° from the nanowire long axis (also denoted in the Figure). Figure 3.6b shows the polarization of emission from the metal-coated nanowire in which both A and B excitons are polarized perpendicular to the nanowire axis. This point will be discussed in greater detail in the next section, but it is indicative of coupling to a cavity mode, and is clearly not dependent on the incident polarization that is isotropic (circular). In order to elucidate the electromagnetic modes responsible for the Purcell enhancements required by this theory, we performed computational electrodynamics simulations to solve for, and examine, the cavity modes.

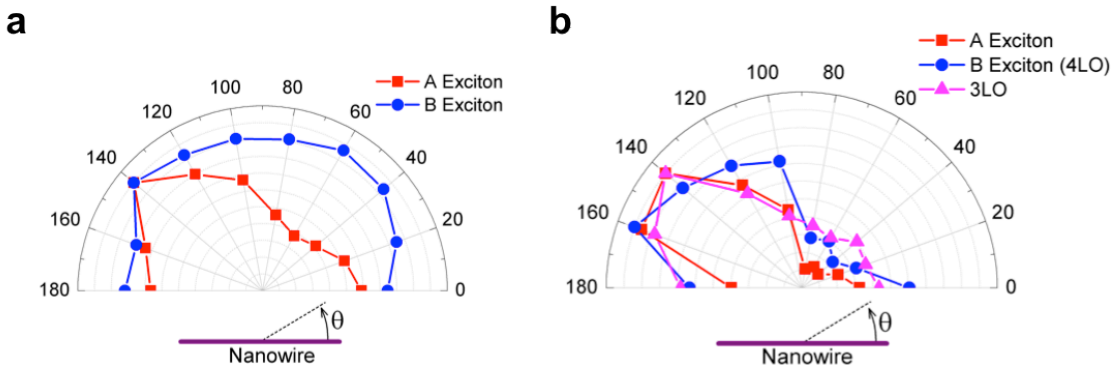

Figure 3.6 | Polarization dependence of the photoluminescence intensity as function of angle, θ, from nanowire long-axis, taken by placing a linear polarizer in front of the spectrometer for a) bare nanowire and b) metal-coated nanowire. From the polarization of the A-exciton in figure 3.6a (which is polarized perpendicular to the c-axis of CdS) it is determined that this batch of nanowires is grown with c-axis ~55° (dashed line at bottom of polar plots) from the nanowire long axis (horizontal purple line at bottom of polar plots). [1]

3.5: Finite Difference Time Domain Simulations of Plasmonically-Coupled Nanowires

3.5.1: Simulation Details

[5]Simulations of the cavity modes of both bare and metal coated nanowires were performed using Lumerical, a commercial Finite Difference Time Domain (FDTD)[21,22] software package. Taking advantage of the cylindrical symmetry of the nanowire, simulations were mostly performed on a 2D cross-section, perpendicular to the nanowire long axis, which in effect simulates an infinitely long wire (though select geometries

---

[5] For an overview of several prominent computational electrodynamics methods, including FDTD, please refer to the review by Smajic et. al.[17a] For a detailed introduction to the FDTD technique please refer to *Computational Electrodynamics: Finite Difference Time Domain Method by Taflove and Hagness, Chapters 1-3*[17a]

were simulated in 3D to ensure the validity of the 2D approximation). As will be discussed further down, the nature of the electromagnetic modes is such that nanowire length does not influence the mode structure unless its magnitude is comparable to the mode wavelength (not the case in our nanowire samples, see chapter 2). The nanowires were excited with a pulsed dipole source in an off-center position. Simulations were performed for all polarizations (with electric field components in-and-out of the plane of the nanowire). The frequency-dependent real and imaginary parts of the dielectric function of Ag were obtained via an analytical fit to experimental data.[23] The real parts of the refractive indices of CdS and SiO_2 were obtained from the *Handbook of Optical Constants*.[24]

3.5.1.1: Nomenclature of Electromagnetic Modes

For the remainder of this thesis, the electromagnetic modes hosted by a nanowire or hybrid-nanowire plasmonic nanocavity will be classified with the naming convention established below. In line with the literature on semiconductor nanowire resonances with k-transverse, that is with propagation constant which is orthogonal to the nanowire long-axis (see section 1.4) we shall label modes that are polarized parallel to the nanowire long axis "TM" or transverse magnetic and those which are polarized perpendicular to the nanowire long axis "TE" or transverse electric[4] [25] (see Figure 3.7). Again, this nomenclature depends on the direction of the electric field polarization with respect to the nanowire long axis and not to the plane of incidence. To provide an example, in the case of Zhang et al.'s work on plasmonic CdS nanowire lasers,[10] the hybrid nanowire-SP

modes (with k-parallel) would be classified as TM, due to their electric field polarization along the nanowire long axis. In the case of the work of Brongersma et al. on WGM resonances (k-transverse) in Germanium nanowires[4] (also known as leaky modes, see section 1.4) both TE and TM modes are realized.

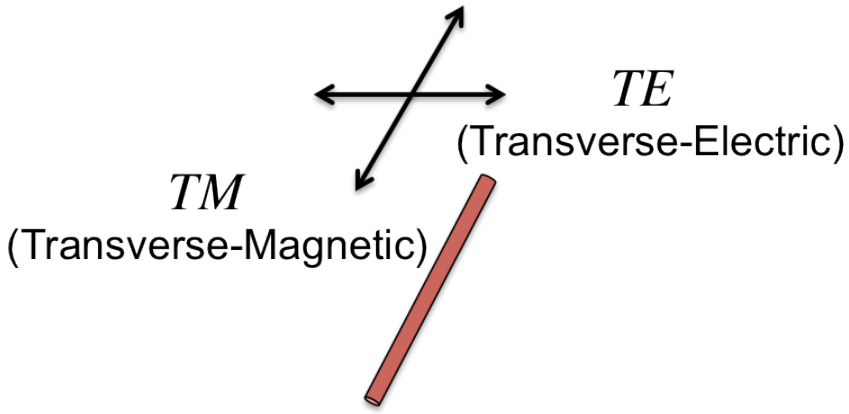

Figure 3.7 | Schematic of naming convention for semiconductor nanowire electromagnetic modes. The black arrows correspond to the electric field polarization with reference to the nanowire below (colored red).

3.5.2: Results and Discussion

As discussed in section 3.4.2, the metal-coated nanowires demonstrate hot exciton emission, which is most intense when the emission is resonant with the B-exciton position (Figure 3.4a, magenta curve). In order to examine the potential for electromagnetic modes involved in the emission process, a metal coated nanowire of the same experimental geometry was simulated (d=140 nm) using the FDTD technique. Taking a Fast Fourier Transform (FFT) of the time domain data reveals a mode near the

B-exciton (2.556 eV) region, the magnetic field intensity profile of which is featured in Figure 3.8. These modes are highly confined to the insulator-metal interface, but noting the insulator is only 5nm in thickness, also leak into the CdS core-region. It should be noted that this mode was excited with an infinitesimal current source (point dipole) with an isotropic average polarization (see section 4.4.1) and in several orientations. It was found that it is only possible to excite this mode with a "TE-polarized" dipole source section, i.e. with electric field components perpendicular to the nanowire long-axis (and in the plane of the wire cross section). The only non-zero magnetic field component is along the nanowire long axis only. Furthermore, these modes propagate along the circumference of the nanowire. In other words, the wavevector, k, is in the angular direction only.

This mode has the same polarization characteristics as the surface plasmon mode at a planar dielectric-metal interface (see section 1.2 for a formal discussion on SP modes), which requires electric field components in the plane of propagation and magnetic field component transverse to the same. Effectively, these are Whispering Gallery Modes (WGM), but with "plasmonic" polarization and which may not be hosted in a bare nanowire of the same size due to small cavity size and associated low confinement (Figure 3.8b). WGM modes are known for being particularly high Q modes, yet when coupled with SPPs can also lead to extremely low mode volumes[26] (see section

1.1 for a brief discussion on WGM resonators). [6]The TE polarization of these WGM modes is further confirmed by the polarization dependent photoluminescence measurements presented in section 3.4.3, where emission from metal coated nanowires is TE polarized (i.e. contains electric field components perpendicular to the nanowire long axis). The combination of experiment and computational electromagnetics simulations reveals that the metal coated nanowires behave as semiconductor nanowires coupled with a plasmonic nanocavity that may host highly confined WGM type modes. Frequency domain calculations for modes propagating parallel to the nanowire long axis yield very high propagation losses (10-30 dB/micron), due to the lossy nature of the metal coating, which means the nanowires (> 1 micron length) cannot support propagating (waveguided) modes.

[6] It should be noted that in section 1.2.1 the SPP mode at a metal-dielectric interface is formally described as a "TM" mode only. This is due to the mode naming convention that depends on field component in relation to the plane of incidence as opposed to a convention that depends on the nanowire-long axis used here. The physical picture, of course, remains the same.

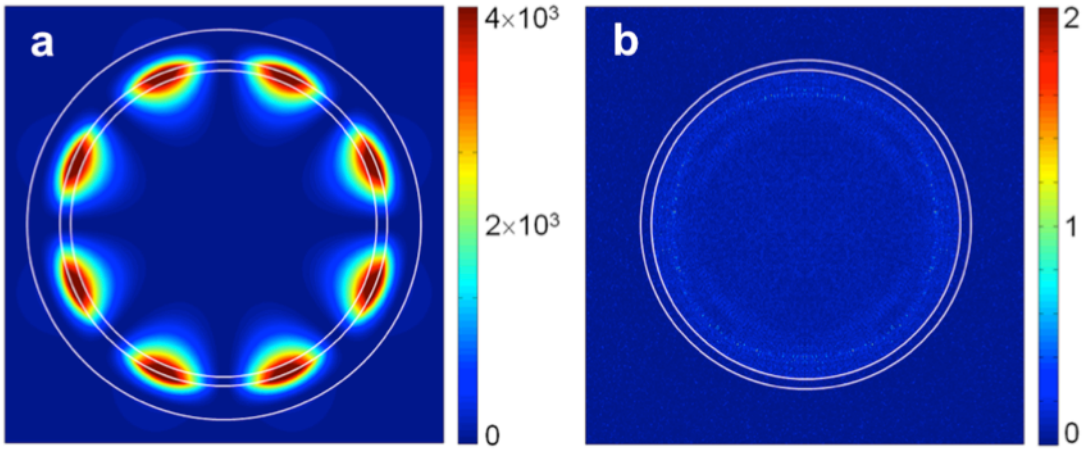

Figure 3.8 | Calculated magnetic field intensity at 2.556 eV (4-LO hot excition/B-exciton energy) for a) d=140 nm plasmonically-coupled nanowire and b) d=140 nm bare nanowire. No electromagnetic mode is observed in the bare nanowire in this energy range. White lines denote material boundaries.[1]

The photoluminescence spectra of various plasmonically-coupled nanowires presented in section 3.4 (Figure 3.3b), demonstrate a strong dependence on the diameter of the nanowire, which would be expected for WGM type modes that propagate along the nanowire circumference only. In order to clarify this dependence, light emission was explored for 44 different nanowire sizes, and the highest intensity peak plotted vs. nanowire diameter (Figure 3.9a, open circles). In order to make a more reliable experimental measurement, the relative enhancement of the 4LO peaks was plotted, instead of the absolute PL intensity (which may be subject to subtle changes in experimental conditions). The enhancement of the 4-LO peak was measured by normalizing all spectra to the respective A-exciton intensity (which is not resonant with any hot PL peaks) and compared to the expected B-exciton intensity in a bare nanowire.[16]

With shrinking nanowire size we observe a monotonic increase in the relative emission intensity of this peak. Furthermore, three peaks at different nanowire diameters punctuate the spectrum. FDTD simulations at the 4-LO spectral position were conducted on plasmonically-coupled nanowires in the same size range. Simulation results were compared with the experimental data, by calculating the average electric field density defined as,

$$E_\sigma = \frac{\iint E(x,y)dxdy}{physical\ nanowire\ core\ area} \qquad \text{Eq. 3.1}$$

This calculation was performed in over 60 different nanowire sizes and plotted vs. diameter on the same graph (Figure 3.9a, red curve). The calculated dependence of the electric field density on nanowire size shows excellent agreement with experimental results. As can be examined from the frequency domain electric field intensity profiles (Figures 3.9b-d) as the size of the nanowire core decreases, the electric field density increases, which closely follows in the increase in hot luminescence (Figure 3.9a). Furthermore, the 3 peaks at *d*=60 nm, 100 nm, and 135 nm correspond to the m=2, 3, and 4th order WGM mode, where m denotes the integer number of wavelengths. These are the "resonant sizes" of the nanowire, which are the dimensions where the SPP-WGM mode is spectrally matched to the emission from CdS. The Purcell factors are calculated in the following subsection.

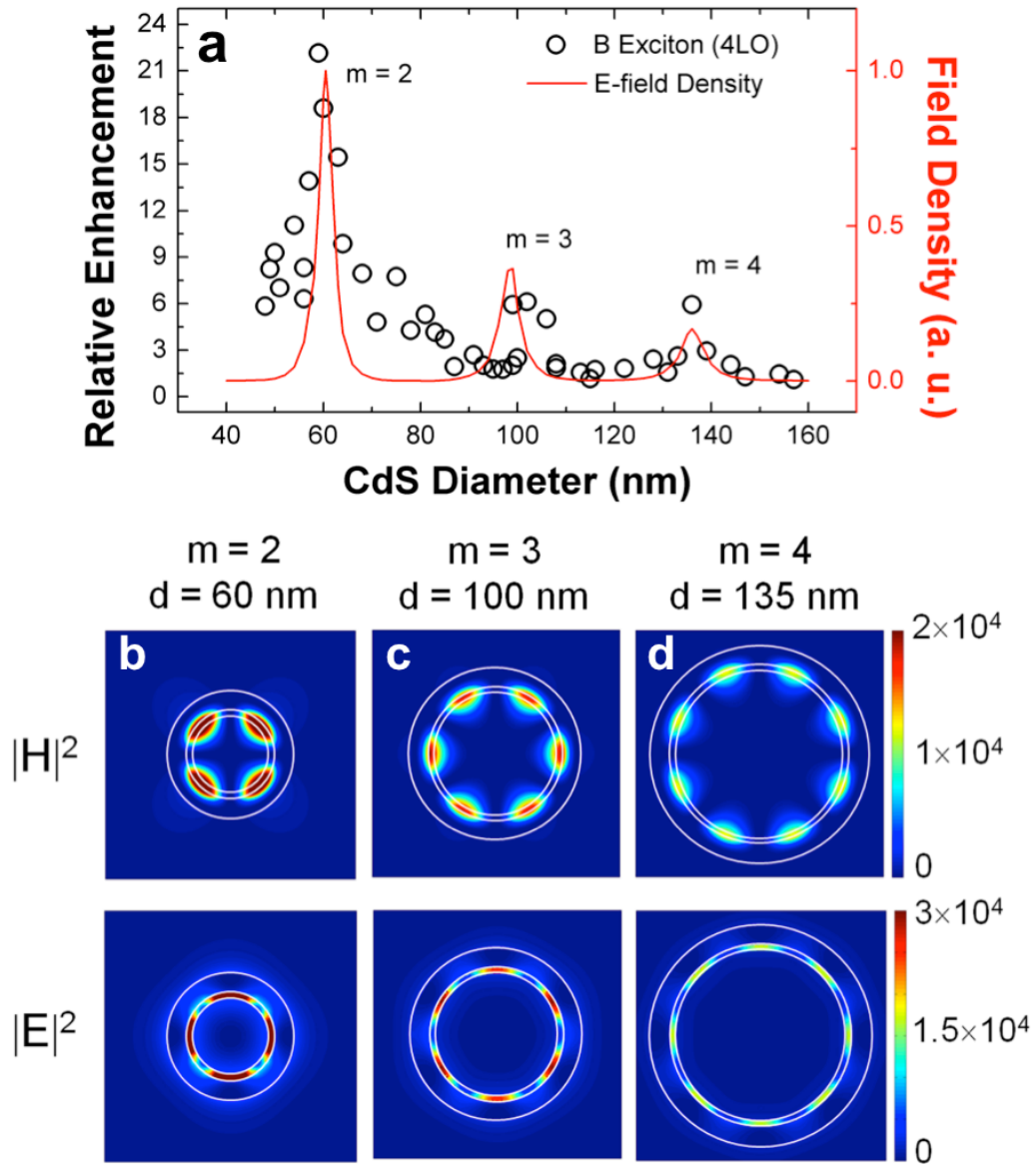

Figure 3.9 | Size-dependent photoluminescence spectra and simulation from plasmonically-coupled core-shell CdS nanowires. a) Size-dependent enhancement of 4-LO hot photoluminescence peak (open circles) and calculated field intensity per unit area (red curve) as a function of nanowire diameter. b-d) Simulated magnetic field (H^2) and electric field (E^2) intensity profiles, as a function of nanowire diameter for three resonant sizes b) *d*=60 nm (azimuthal mode number, m=2) c) *d*=100 nm (m=3), and d) *d*=135 nm (m=4).[1]

3.5.2.1: Calculating the Purcell Factor

As discussed in section 1.1, a dipole emitter in resonance with an electromagnetic mode of an optical cavity will experience an enhanced spontaneous emission rate. The original formulation of the Purcell factor is presented in section 1.1, but a slightly modified version is used for this work based on the derivation by Boroditsky et al.[27] For a non-degenerate mode in a semiconductor optical cavity the Purcell factor is given by:

$$\frac{\gamma}{\gamma_0} = \frac{3Q(\lambda/2n)^3}{2\pi V_m} \qquad \text{Eq. 3.2}$$

where Q, λ, n, and V_m are the quality factor, free space wavelength, refractive index, and effective mode volume respectively as before. This differs from the original form by a factor of π/4 (i.e it is very similar). The difference arises from the Lorentzian nature of the semiconductor resonance and the reader is referred to the original paper for details of the derivation. Again, the effective mode volume is expressed by

$$V_{eff} = \frac{\int \varepsilon(r)E^2(r)d^3r}{(\varepsilon(r)E^2(r))_{max}} \qquad \text{Eq. 3.3}$$

where $\varepsilon(r)$ is the material dielectric constant. Taking the advantage of cylindrical symmetry of nanowire structures, the effective mode volume of whispering gallery modes can be expressed as:

$$V_m \approx A_m \cdot L = \frac{\int \varepsilon(r)E^2(r)d^2r}{(\varepsilon(r)E^2(r))_{max}} \cdot L \qquad \text{Eq. 3.4}$$

where A_m is the effective mode area and L is the effective dimension of whispering gallery mode in the cylinder axis. Furthermore, as demonstrated in the previous section, the SPP-WGM modes are confined to the cross section of the nanowire and do not propagate more than one wavelength away from the excitation region (see Figure 3.8c). In other words, $L \sim \lambda_{SPP}$ where λ_{SPP} is the wavelength of the cavity plasmon. Thus, to obtain the effective mode volume, V_m, for the plasmonically-coupled nanowires, we calculated A_m from the electric field intensity profile and multiplied by λ_{SPP}, which enabled us to use electromagnetic simulation data from the 2D cross section only.

The frequency domain electric-field intensity profiles (Figure 3.9b-d) provide all of the necessary data for calculation of the Purcell factor. The calculated field enhancements for these three resonant cases are 40,000 and 14,400, and 6,400 respectively. In particular, the smallest resonant size nanowire (d=60 nm) demonstrates a quality factor of 55 (high given the nanoscale size of the cavity). Of particular note, is the extremely small mode volume associated with these modes, which is $10^{-4}\ \lambda_0$ where λ_0 is the vacuum wavelength. In other words, light in these cavities is 10,000 times more confined than that in free space, which when coupled with moderate quality factors leads to the exceptionally high Purcell enhancements. In this case (d=60 nm), the Purcell factor is calculated to be 3.8×10^3, which would place the Purcell-enhanced radiative recombination time in the ps range thereby making the radiative process competitive with the non-radiative process.

3.6: Time-Resolved Photoluminescence Measurements

3.6.1: Experimental

In collaboration with Kikkawa group at the Department of Physics and Astronomy at the University of Pennsylvania, time resolved PL measurements were performed on an array of 300-500 plasmonic nanowires, with average diameter of 140 nm $\pm$ 50 nm at room temperature (Figure 4.8). These time-resolved measurements were acquired using the optical Kerr gate effect.[28] The excitation source was the 800 nm output of a 1 kHz regenerative amplifier (Spectra-Physics Spitfire), which was frequency-doubled in a β-barium borate crystal. The spot size (~75 μm) yields an average power density of 0.4 W/cm^2. The resulting emission from the sample was focused onto a Kerr medium (0.76 mm thick Suprasil II plate, Meller Optics). The 800 nm fundamental pulse was used to generate a transient birefringence in the fused silica, which rotated the photoluminescence signal passing through it. Using orthogonally oriented linear polarizers (before and after the Kerr medium) eliminates photoluminescence at other delay times. The remaining photoluminescence signal was focused onto a 500 cm spectrometer (Triax 552, JY) thermally cooled CCD (Spec-10, Princeton Instruments). Varying the position of the delay line retroreflector with regards to the excitation beam yields maps of the emission spectra vs. delay time with sub-ps temporal resolution.

3.6.2: Results and Discussion

A near complete transition from thermalized luminescence to hot luminescence is further corroborated by time resolved photoluminescence spectroscopy, which shows a

transition from 1.6 ns lifetime in bare CdS (in agreement with literature values for bulk CdS, see section 3.1.2) to 7 ps in the plasmonically-coupled samples (Figure 3.10). Perhaps more impressive is the fact that these are ensemble measurements made on CdS nanowires with significant spread in their size distribution, i.e. the measured sample had an average diameter *d*=140nm +/- 50 nm, thus even lower emission lifetimes are expected on the single nanowire level at the "resonant sizes", in this case *d*=60 nm, 100 nm or 135 nm, which are the dimensions where the SPP-WGM mode is spectrally matched to the emission (see Figure 3.9a).[1]

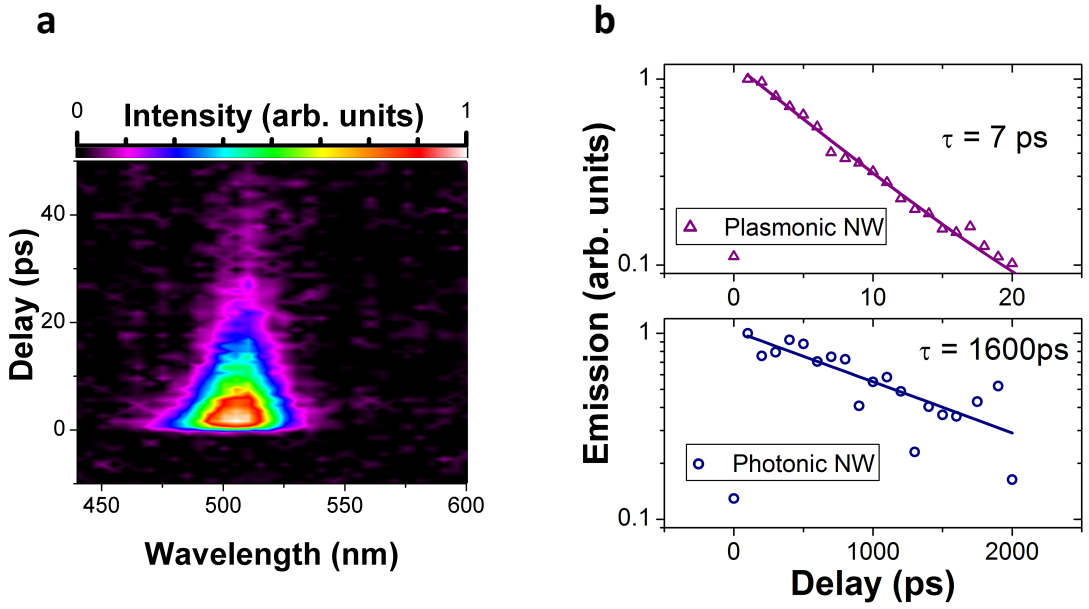

Figure 3.10 | a) Time resolved PL spectral map from ensemble of 300-500 nanowires with average diameter 140±50 nm at room temperature (300 K). b) Time-resolved integrated emission intensity for plasmonic (upper) and photonic (lower) nanowires. Solid lines are an exponential fit to the data. Resulting radiative recombination lifetimes of 7 ps and 1600 ps for plasmonically-coupled and bare nanowires respectively are included next to the fitted curves.[1]

3.7: Concluding Remarks on Surface Plasmon-Enhanced Light Emission

To summarize, by interfacing a direct bandgap material (e.g. CdS) with an appropriately designed metal plasmon nanocavity (a.k.a. an optical antenna) the spontaneous emission rate was enhanced to the point where it became competitive with intra-band relaxation to enable emission from high-energy hot states; an interesting finding from a spectroscopic point of view. Furthermore, this work establishes the nanocavity plasmon WGM cavity as a test-bed for cavity Quantum Electrodynamics, which requires high ratios of Q/V_m to enhance light-matter interaction. From a device physics perspective, on the other hand, this implies that nanowire optical and optoelectronic devices may be modulated at orders of magnitude higher frequency by interfacing the active material with an appropriate metal nanocavity (and there is no immediate impediment as to why the metal cavity could not double as a channel for charge injection and extraction).

3.8: Light absorption in Semiconductor Nanowires

In general, absorption in semiconductor nanowires is dictated by the polarization of incoming light and the dielectric mismatch that exists between the high refractive index nanowires and air. In the absence of electromagnetic resonances, it has been demonstrated that semiconductor nanowires absorb light, which is polarized parallel to the long axis of the nanowire much more readily than light which is polarized perpendicular to the long axis (in the plane of the cross section) due to the dielectric mismatch.[29] In line with the literature on nanowire resonances, we shall label modes that

are polarized parallel to the nanowire long axis "TM" or transverse magnetic and those which are polarized perpendicular to the nanowire long axis "TE" or transverse electric.[4] For a more detailed discussion on nomenclature of nanowire optical modes the reader is referred to section 3.5.1.1.[25] This polarization anisotropy, which is observed in bare semiconductor nanowires when the cross section is small compared to the wavelength of the incoming light, is orthogonal to that of semiconductor nanowires integrated with a plasmonic nanocavity discussed above. Boundary conditions on SPP modes dictate that their (electric field) polarization must be in the direction of propagation[17] (see Chapter 1, section 1.2.1). Thus, for SP modes in the plane of the nanowire cross section, we expect TE polarized light to play a significant role in the absorption characteristics of the semiconductor nanowire, traditionally dominated by TM polarized light in bare nanowires.[29]

3.9: Simulating Absorption: FDTD Methodology

The absorption properties of both Cadmium Selenide and Germanium are highlighted for this study. CdSe is chosen due the similarity in its dielectric (refractive index) properties to CdS, but with a lower bandgap (1.74 eV) that enables absorption across the visible spectrum. Germanium, on the other hand, is an indirect band gap semiconductor with established electronic and optoelectronic applications.[4,30,31] Simulations were performed using the time Finite Difference Time Domain technique and the Lumerical commercial solver as before (see section 3.5), but with several key differences. First, we replicate our experimental setup by using a Gaussian beam as the

excitation source, which is focused through a 0.7 NA lens and resulting in a diffraction-limited spot at the sample. Secondly, in order to obtain absorption data of the highest possible accuracy, several single frequency simulations were performed as opposed to simulating broadband data with a single pulsed excitation. This eliminates the need to fit the optical constants of CdSe[24] and Ge[32] (Figure 3.11), which, in the case of CdSe (Figure 3.11a), feature several excitonic resonances that make obtaining accurate fits a difficult process. At each frequency the absorbed power, *P*, is calculated as:

$$P = -0.5\omega|E^2|Imag(\varepsilon) \qquad \text{Eq. 3.5}$$

where ω, E, and ε are the angular frequency, electric field amplitude, and dielectric function respectively. This is normalized to the source power, which allows us to express the absorption as percent absorbed power with respect to the source. Furthermore, any power absorbed outside of the nanowire core (for example in the metal) is filtered out to provide a measure strictly of the power that is absorbed by the nanowire.

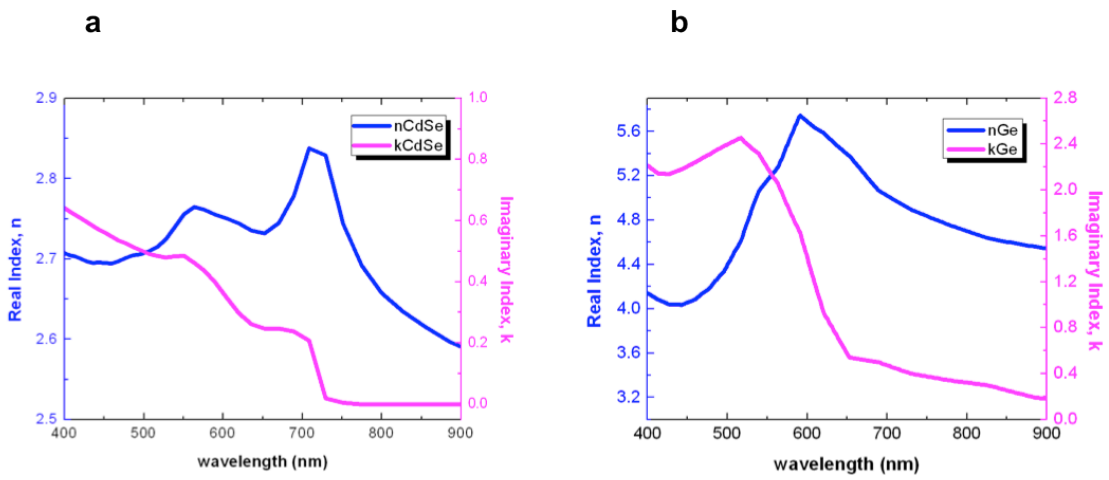

Figure 3.11 | Experimentally obtained refractive index values for a) CdSe and b) Ge. The real part of the refractive index (blue curves) and imaginary part (magenta curves) are listed for the wavelength range over which absorption spectra were computed.

3.10: Results and Discussion

3.10.1: Anomalous Absorption in Plasmonically-Coupled CdSe, a Direct Bandgap Material

The simulated absorption spectra of a bare CdSe nanowire (diameter *d*=60 nm) is shown in figure 3.12a. As expected in this subwavelength nanowire size range, TM polarized light dominates the absorption spectra due to the much higher dielectric mismatch experienced by TE polarized light, and approaches zero absorption near the CdSe bandgap due to the lack of electronic states at lower energies. Absorption of TE polarized light demonstrates a monotonic decrease with increasing wavelength (Figure 3.12b, blue curve) due to the lack of any optical resonances and due to increasing spatial (refractive index) mismatch with increasing wavelength of the incident light. Addition of

a conformally coated thin (15 nm) silver film on the CdSe nanowire (see Figure 3.2), on the other hand, reverses the polarization dependence of the absorption spectrum, where the absorption is now dominated by the TE polarized light (Figure 3.12b, red curve) albeit at the expense of absorption due to TM polarized light (Figure 3.12b, blue curve). Interestingly, by placing what is essentially a mirror on the active material we would expect a decrease in light absorption all along the active layer (in this case the CdSe nanowire), but by making the Ag film thin, and on the order of the skin depth, the system is able to host SP modes which transform this system into an optical antenna, capable of concentrating far field light into the nanowire core (Figure 3.12c). Here, the absorption spectrum is punctuated by the dipolar SP resonance (centered at ~690 nm) and a higher order mode centered at ~480 nm. Absorption in the metal-coated nanowire due to TM radiation is mediated by the fundamental (first order) WGM mode resonance (Figure 3.12d) and will be exploited to achieve increases in absorption to levels even higher than the photonic case (discussed later). Furthermore, the resonances are highly tunable (Figure 3.12e) demonstrating a blue shift with increasing shell size that is in line with that reported for core-shell metal-semiconductor nanoparticles.[33]

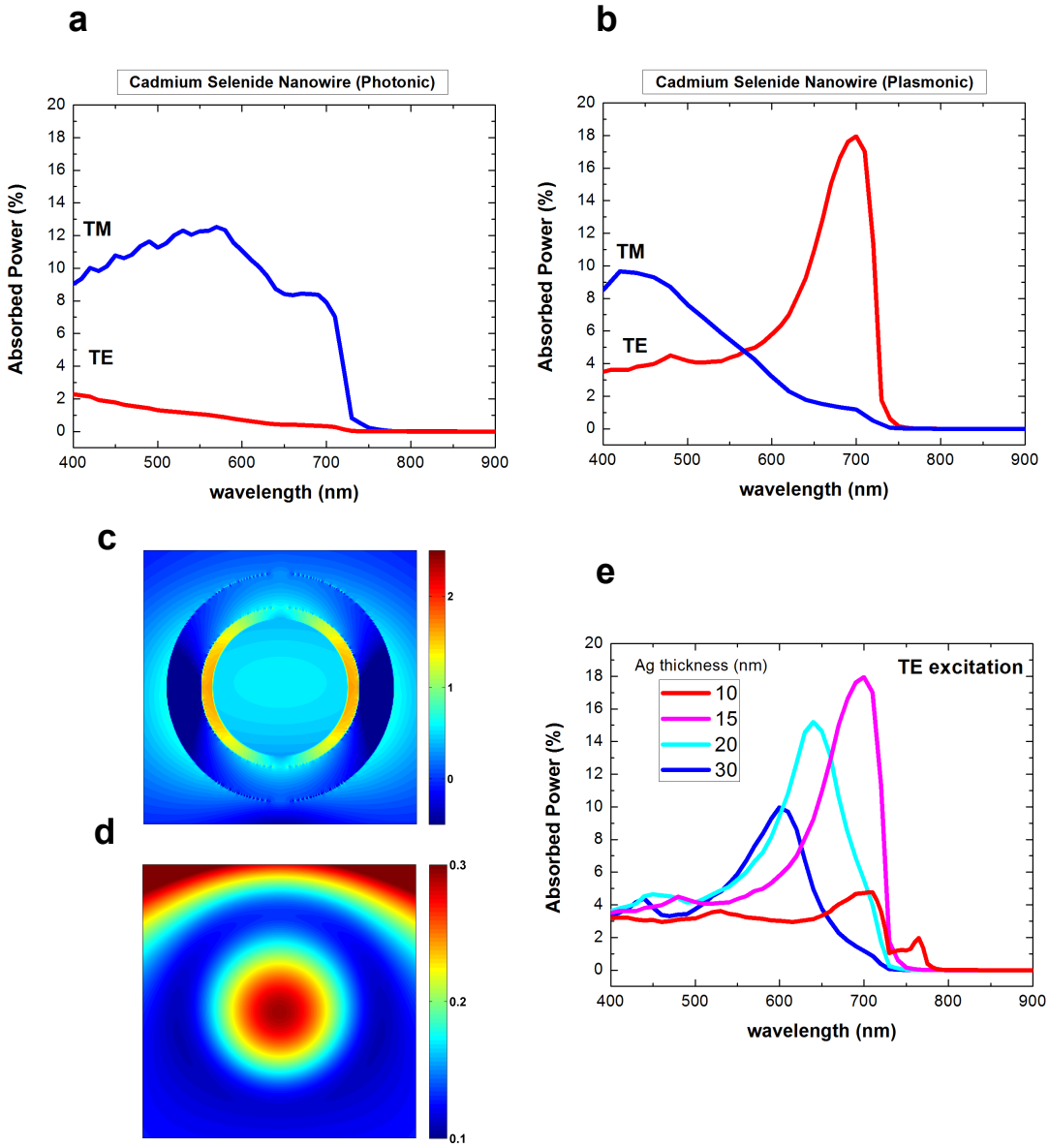

Figure 3.12 | Enhanced absorption with anomalous polarization dependence (with respect to a bare CdSe nanowire) in a plasmonically-coupled CdSe nanowire. a, b) Absorption spectrum of (a) bare CdSe nanowire (d=60 nm) and (b) plasmonically-coupled CdSe nanowire featuring absorption of TM polarized light (blue curve) and TE polarized light (red curve). c) Frequency domain electric field intensity ($|E|^2$) profile of dipole surface plasmon resonance due to TE excitation in plasmonically-coupled CdSe (log scale). d) Frequency domain electric field intensity ($|E|^2$) profile of fundamental WGM resonance in plasmonically-coupled CdSe due to TM excitation (linear scale). e) Absorption spectra of plasmonically-coupled CdSe under TE excitation with varying Ag shell thicknesses (in range 10 nm to 30 nm).

3.10.2: Anomalous Absorption in Plasmonically-Coupled Ge, an Indirect Bandgap Material

Similar studies were conducted on Ge, which is generally used as an electronic (as opposed to optical) material as discussed above. The characteristics of the absorption spectrum of a bare Ge nanowire, *d*=40 nm (Figure 3.13a), are similar to those of CdSe, but with the spectrum extending to the near IR due to the lower Ge band gap (0.67 eV). We note that in the previous study of CdSe, 15 nm is the smallest thickness of the Ag shell possible, before the dipolar SP resonance is pushed below the CdSe bandgap (as demonstrated for a CdSe nanowire coupled with a 10 nm Ag shell, Figure 3.12e, red curve). In the case of Ge, which exhibits a lower energy bandgap, addition of a 10 nm Ag coating yields broadband enhancement not only the of the TE-absorption (Figure 3.13b, red curve), but also of the absorbed TM-polarized light (Figure 3.13b, blue curve) in comparison to the bare Ge nanowire. Again, the TE-spectrum is mediated by the strong dipolar SP-resonance (Figure 3.13c). Furthermore, we note that by choosing a smaller nanowire (*d*=40 nm, compared to *d*=60 nm for CdSe) we are able to tune the resonances to the visible range, which highlights the tunability of these resonances as function of nanowire dimensions. Again, TM absorption is dominated by the lowest order WGM mode (Figure 3.13d). In this case, absorption of TM polarized light is enhanced across the entire spectrum and to levels higher than that of the bare Ge nanowire. We expect that the broadband enhancement of the TM-absorption is due in part to the high refractive index of Ge (which is known to lead to WGM resonances even in the photonic case[4]), coupled with limited radiative losses, which are achieved by placing a metal around the

nanowire. Although for the TM case this is not an SP mode *per se*, using metals to limit radiative losses of photonic modes is a known technique that leads to increased photonic confinement.[34-36]

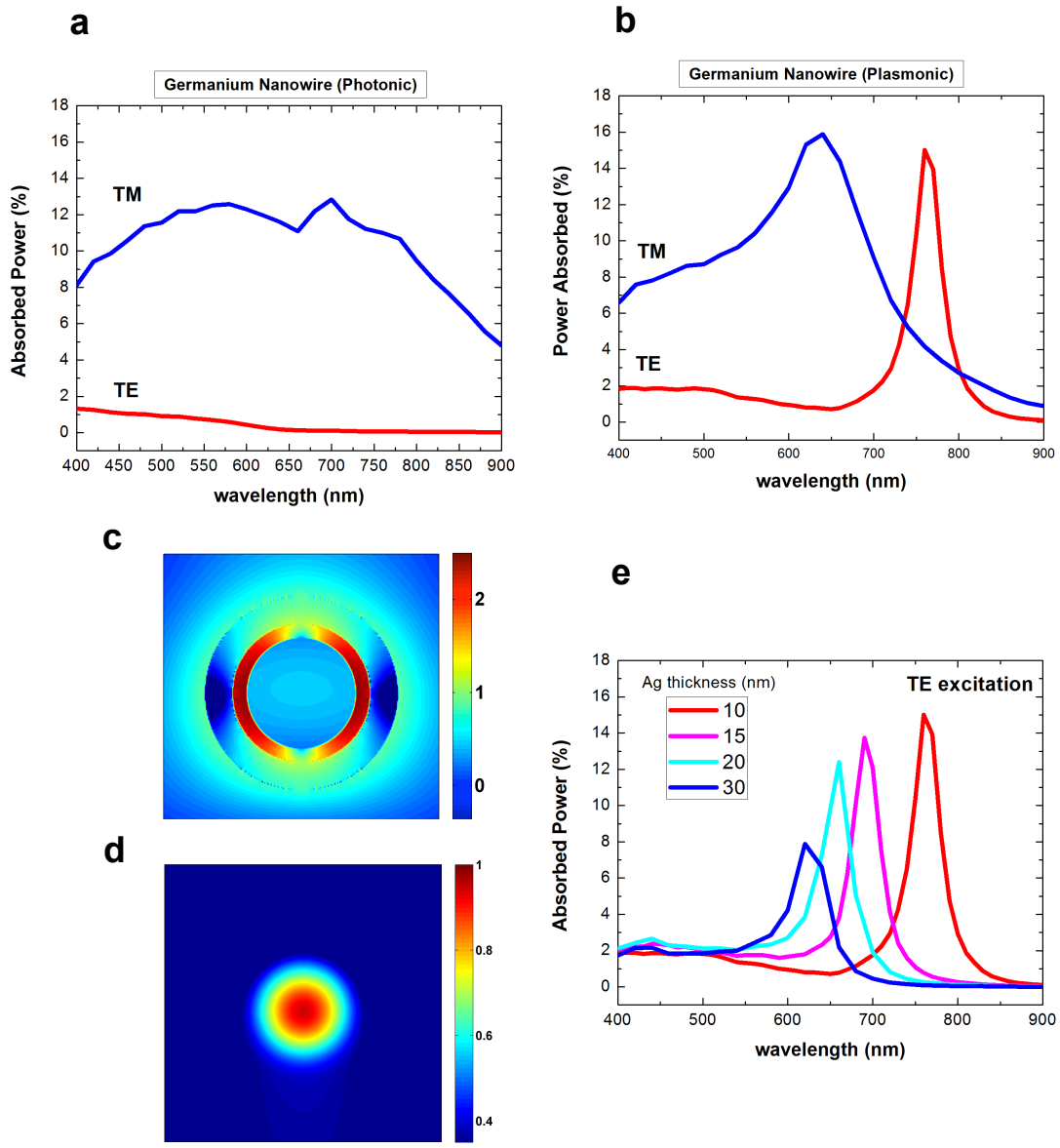

Figure 3.13 | Enhanced absorption with anomalous polarization dependence (when compared to a bare Ge nanowire) in a plasmonically-coupled Ge nanowire. a, b) Absorption spectrum of (a) bare Ge nanowire (d=40 nm) and (b) plasmonically-coupled Ge nanowire featuring absorption of TM polarized light (blue curve) and TE polarized light (red curve). c) Frequency domain electric field intensity ($|E|^2$) profile of dipole surface plasmon resonance due to TE excitation in plasmonically-coupled Ge (log scale). d) Frequency domain electric field intensity ($|E|^2$) profile of fundamental WGM resonance in plasmonically-coupled Ge due to TM excitation (linear scale). e) Absorption spectra of plasmonically-coupled Ge under TE excitation with varying Ag shell thicknesses (in range 10 nm to 30 nm).

3.11: Concluding Remarks on SP Enhanced Light Absorption

As demonstrated in this study, the semiconductor nanowire-metal core-shell architecture can lead to broadband enhancement in the absorption of TE polarized light, which is usually poorly absorbed in high-aspect ratio, high-refractive index nanowires due to refractive index mismatch. Furthermore, through optimization of the cavity dimensions (nanowire size and metal shell thickness) it was shown the broadband enhancement in the absorption spectrum may be achieved under isotropic polarization (both TE and TM polarized light), where both SP modes and highly confined photonic modes play a role. We expect that such optical antenna-based engineering of absorption in semiconductor nanowires to have direct applications in photodetection and photovoltaics, which will add a viable alternative to the LSP-based engineering examined thus far.[25,37]

References

1 Cho, C.-H., Aspetti, C. O., *et al.* Tailoring hot-exciton emission and lifetimes in semiconducting nanowires via whispering-gallery nanocavity plasmons. *Nat Mater* **10**, 669-675 (2011).

2 Hayden, O., Agarwal, R. & Lieber, C. M. Nanoscale avalanche photodiodes for highly sensitive and spatially resolved photon detection. *Nat Mater* **5**, 352-356 (2006).

3 Sirbuly, D. J., Tao, A., Law, M., Fan, R. & Yang, P. Multifunctional Nanowire Evanescent Wave Optical Sensors. *Advanced Materials* **19**, 61-66, doi:10.1002/adma.200601995 (2007).

4 Cao, L. Y. *et al.* Engineering light absorption in semiconductor nanowire devices. *Nat Mater* **8**, 643-647, doi:Doi 10.1038/Nmat2477 (2009).

5 Law, M., Greene, L. E., Johnson, J. C., Saykally, R. & Yang, P. D. Nanowire dye-sensitized solar cells. *Nat Mater* **4**, 455-459, doi:Doi 10.1038/Nmat1387 (2005).

6 Pankove, J. I. *Optical Processes in Semiconductors*. (Dover Publications, 1975).

7 Kasha, M. Characterization of Electronic Transitions in Complex Molecules. *Discuss Faraday Soc*, 14-19 (1950).

8 Wiesner, P. & Heim, U. Dynamics of Exciton-Polariton Recombination in Cds. *Physical Review B* **11**, 3071-3077, doi:Doi 10.1103/Physrevb.11.3071 (1975).

9 Dassarma, S., Jain, J. K. & Jalabert, R. Hot-Electron Relaxation in Gaas Quantum Wells. *Physical Review B* **37**, 1228-1230, doi:Doi 10.1103/Physrevb.37.1228 (1988).

10 Oulton, R. F. *et al.* Plasmon lasers at deep subwavelength scale. *Nature* **461**, 629-632 (2009).

11 Zhang, J., Li, D. H., Chen, R. J. & Xiong, Q. H. Laser cooling of a semiconductor by 40 kelvin. *Nature* **493**, 504-508, doi:Doi 10.1038/Nature11721 (2013).

12 Hopfield, J. J. & Thomas, D. G. Polariton Absorption Lines. *Physical Review Letters* **15**, 22-&, doi:Doi 10.1103/Physrevlett.15.22 (1965).

13 van Vugt, L. K. *et al.* Variable Temperature Spectroscopy of As-Grown and Passivated CdS Nanowire Optical Waveguide Cavities. *The Journal of Physical Chemistry A* **115**, 3827-3833, doi:10.1021/jp108167t (2011).

14 Adachi, S. *Properties of Group-IV, III-V and II-VI Semiconductors*. (Wiley, 2005).

15 van Vugt, L. K. *et al.* Variable Temperature Spectroscopy of As-Grown and Passivated CdS Nanowire Optical Waveguide Cavities. *Journal of Physical Chemistry A* **115**, 3827-3833, doi:Doi 10.1021/Jp108167t (2011).

16 Thomas, D. G. & Hopfield, J. J. Exciton Spectrum of Cadmium Sulfide. *Physical Review* **116**, 573-582, doi:DOI 10.1103/PhysRev.116.573 (1959).

17 Maier, S. A. *Plasmonics: Fundamentals and Applications*. (Springer, 2007).

18 Gross, E., Permogor.S, Travniko.V & Selkin, A. Hot Excitons and Exciton Excitation Spectra. *Journal of Physics and Chemistry of Solids* **31**, 2595-&, doi:Doi 10.1016/0022-3697(70)90254-4 (1970).

19 Permogorov, S. Hot Excitons in Semiconductors. *Phys Status Solidi B* **68**, 9-42, doi:Doi 10.1002/Pssb.2220680102 (1975).
20 Pelekanos, N. *et al.* Hot-Exciton Luminescence in Znte/Mnte Quantum-Wells. *Physical Review B* **43**, 9354-9357, doi:Doi 10.1103/Physrevb.43.9354 (1991).
21 Smajic, J., Hafner, C., Raguin, L., Tavzarashvili, K. & Mishrikey, M. Comparison of Numerical Methods for the Analysis of Plasmonic Structures. *J Comput Theor Nanos* **6**, 763-774, doi:Doi 10.1166/Jctn.2009.1107 (2009).
22 Taflove, A. & Hagness, S. C. *Computational Electrodynamics: The Finite Difference Time-Domain Method*. (Artech House, 2005).
23 Johnson, P. B. & Christy, R. W. Optical Constants of Noble Metals. *Physical Review B* **6**, 4370-4379, doi:Doi 10.1103/Physrevb.6.4370 (1972).
24 Palik, E. D. & Ghosh, G. *Handbook of optical constants of solids*. (Academic Press, 1998).
25 Hyun, J. K. & Lauhon, L. J. Spatially Resolved Plasmonically Enhanced Photocurrent from Au Nanoparticles on a Si Nanowire. *Nano Letters* **11**, 2731-2734, doi:Doi 10.1021/Nl201021k (2011).
26 Min, B. K. *et al.* High-Q surface-plasmon-polariton whispering-gallery microcavity. *Nature* **457**, 455-U453, doi:Doi 10.1038/Nature07627 (2009).
27 Boroditsky, M. *et al.* Spontaneous emission extraction and Purcell enhancement from thin-film 2-D photonic crystals. *J Lightwave Technol* **17**, 2096-2112, doi:Doi 10.1109/50.803000 (1999).
28 Fleming, G. R. *Chemical applications of ultrafast spectroscopy*. (Oxford University Press, 1986).
29 Wang, J., Gudiksen, M. S., Duan, X., Cui, Y. & Lieber, C. M. Highly polarized photoluminescence and photodetection from single indium phosphide nanowires. *Science* **293**, 1455-1457 (2001).
30 Xiang, J. *et al.* Ge/Si nanowire heterostructures as high-performance field-effect transistors. *Nature* **441**, 489-493 (2006).
31 Yan, H. *et al.* Programmable nanowire circuits for nanoprocessors. *Nature* **470**, 240-244, doi:Doi 10.1038/Nature09749 (2011).
32 Aspnes, D. E. & Studna, A. A. Dielectric Functions and Optical-Parameters of Si, Ge, Gap, Gaas, Gasb, Inp, Inas, and Insb from 1.5 to 6.0 Ev. *Physical Review B* **27**, 985-1009, doi:Doi 10.1103/Physrevb.27.985 (1983).
33 Oldenburg, S. J., Averitt, R. D., Westcott, S. L. & Halas, N. J. Nanoengineering of optical resonances. *Chem Phys Lett* **288**, 243-247, doi:Doi 10.1016/S0009-2614(98)00277-2 (1998).
34 Yu, K., Lakhani, A. & Wu, M. C. Subwavelength metal-optic semiconductor nanopatch lasers. *Optics Express* **18**, 8790-8799 (2010).
35 Nezhad, M. P. *et al.* Room-temperature subwavelength metallo-dielectric lasers. *Nature Photonics* **4**, 395-399, doi:Doi 10.1038/Nphoton.2010.88 (2010).
36 Ni, C. Y. A. *et al.* Metal-Coated Zinc Oxide Nanocavities. *Ieee J Quantum Elect* **47**, 245-251, doi:Doi 10.1109/Jqe.2010.2073680 (2011).

37 Colombo, C., Krogstrup, P., Nygard, J., Brongersma, M. L. & Morral, A. F. I. Engineering light absorption in single-nanowire solar cells with metal nanoparticles. *New J Phys* **13**, doi:Doi 10.1088/1367-2630/13/12/123026 (2011).

Chapter 4. Silicon Coupled with Plasmon Nanocavity Generates Bright Visible Hot Luminescence

4.1: Introduction

4.1.1: Motivation

In the previous chapter, experiments on plasmonically-coupled CdS demonstrated that we may use deeply-confined nanocavity plasmons to generate orders of magnitude increases in the spontaneous radiative decay rate of materials, to the point where it is possible to make radiative decay competitive with non-radiative relaxation, and thus activate luminescence from non-thermalized (hot) carriers. This was confirmed via steady state photoluminescence spectroscopy, numerical simulation of the cavity modes and time-resolved photoluminescence spectroscopy. Furthermore, we elucidated the role of electromagnetics (cavity modes) and solid state physics (phonons) in mediating hot photoluminescence. Increasing the quantum efficiency in CdS wasn't the end goal per se, as this already a direct-band gap material that emits light efficiently. In terms of making more efficient light emitters, CdS is not the appropriate material as its quantum yield (QY) is already high.[1] In terms of more efficient light emission, materials that would benefit from highly enhanced spontaneous emission would be "dark" materials i.e. indirect-bandgap semiconductors, which convert energy to heat much more readily than to light.[2] In fact, light-emitting materials, which already have a high QY, will often see a

drop in their QY when they are interfaced with optical antennas due to the enhancement of both non-radiative and radiative processes (see section 1.3). Materials with low intrinsic QY, on the other hand, will generally observe an increase in their QY due to the comparatively high increases in radiative decay rate,[3] given proper optimization of active media-metal architecture as discussed above in the previous chapter.

Silicon is one of the most important of the indirect-band gap semiconductor materials due to its ubiquity in the semiconductor electronics industry. Silicon combines a suite of attractive physical properties: it is mechanically robust, conductive, non-toxic, abundant, and as such the semiconductor industry has spend decades perfecting Si processing techniques. Yet one of the key properties that does not belong to Si is efficient light emission. It has an extremely low quantum yield estimated to be between 10^{-4}-10^{-6} (discussed further down). This is one of the largest impediments to making the transition from Si electronics into Si-based photonics, plasmonics or even opto-electronics, thus the previous two decades have witnessed a significant scientific effort towards engineering the optical properties of Si[4-8]and realizing the next generation of Si-based ultra-fast opto-electronic components.[9,10] Furthermore, semiconductor giants like Intel have made large monetary investments into silicon-based photonics (i.e. Intel Silicon Photonics lab)[11] where the goal is to make optical devices that operate at the speed of light, while taking advantage of the decades worth of silicon processing experience of the semiconductor industry. As stated by Mario Paniccia, head of silicon photonics at Intel, the goal is to "siliconize photonics"[11]; and a fundamental piece of the puzzle, arguably one of the most challenging, is the development of a silicon light source. The following two chapters

discuss how the lessons from interfacing CdS with a plasmonic optical cavity were applied to silicon. The result was broadband luminescence from "bulk" sized silicon nanowires, that is silicon that is not quantum confined, and over a broad nanowire size range (40-150 nm in diameter and lengths up to several microns).

4.1.2: Charge Carrier Excitation and Relaxation Dynamics in Si (and other Indirect Bandgap Semiconductors).

In Si, once the electron is excited to the conduction band, typically by a phonon assisted process, its behavior is quite similar to that of an excited charge carrier in the direct-band gap semiconductor (see Chapter 3, section 3.1.2). The excited electron will quickly relax to the conduction band minimum via phonon scattering events (i.e. intra-band relaxation) that occur on a 0.1-1 ps timescale[12-14] (Figure 4.1). The key difference with a direct-band gap material like CdS, is that in an indirect band gap material such as Si, once the electron reaches the conduction band minimum (near the X and L points), it is momentum mismatched from the valence band maximum at the Γ point (Figure 4a). This prohibits radiative recombination of the electron-hole pair from the conduction band minimum (the ground state of the excited electron) to the valence band maximum as both energy and momentum must be conserved. Thus, in order for the electron to recombine radiatively with a hole it must exchange momentum with the crystal lattice, which is an incredibly inefficient process. Unlike in CdS, here the QY is ~10^{-6} at the conduction band minimum[2] and estimated to be 10^{-4} near the direct bandgap (at the Γ point).[15] The estimate for the QY near the Γ point is obtained from the radiative recombination lifetime

for electrons near the Γ point, reported as ~10 ns[16] and the known intra-band relaxation times stated above, which is taken as the time for non-radiative recombination. Using the usual prescription for calculation quantum yield, i.e.

$$QY = \frac{\gamma_{radiative}}{\gamma_{radiative} + \gamma_{non-radiative}} \quad \text{Eq. 4.1}$$

where γ is the decay rate (i.e. the reciprocal of the associated lifetime).

Again, given the fast intra-band relaxation times, most excited charge carriers will decay to conduction band minimum first, at which point the relaxed carrier is much more likely to lose its energy via several non-radiative processes such as recombination at defect sites (impurity states), free carrier absorption,[17] and Auger recombination.[4] Stating the problem another way, if we were to obtain light emission from Si, it would benefit us to do so before the electron has time to relax to the conduction band minimum (thereby increasing momentum mismatch with the light-line at k~0). Stimulation of hot-luminescence is a logical route for efficient light emission from Si, noting the farther carriers relax along the electronic dispersion, the less-likely it is to find a phonon of the appropriate momentum to enable radiative recombination. As was the case with CdS, hot luminescence would depend on significant shortening of the spontaneous emission lifetime (or enhancement of the spontaneous emission rate), which may be accomplished through the use of highly confined plasmonic optical cavities featuring large values of Q/V_m (see sections 1.1, 1.3 and chapter 3). Si nanowires were integrated with a plasmonic nanocavity as detailed in the following section.

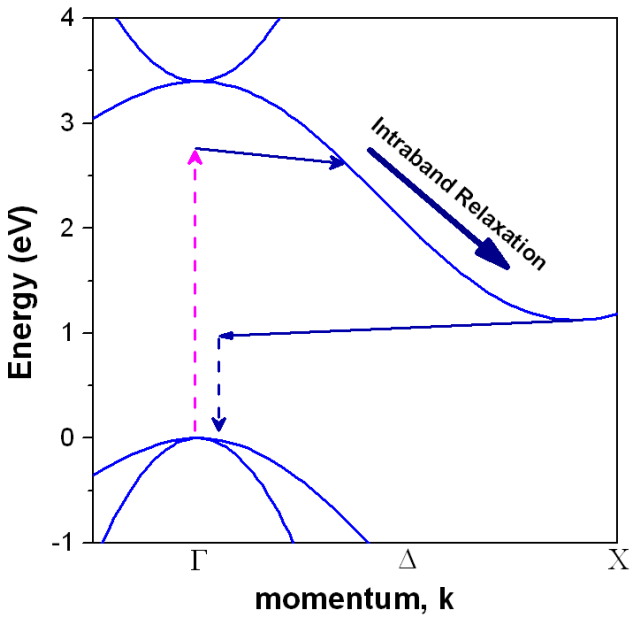

Figure 4.1 | Schematic of electronic dispersion relation in Si depicting the excited charge carrier generation (magenta curve), relaxation, and emission processes (dark blue curves).[15]

4.2: Synthesis of Plasmonically-Coupled Silicon Nanowires

Silicon nanowires were obtained from Sigma Aldrich in powder form. These were size-polydispersed with a reported 40 nm average diameter and 1-20 micron length. Experimentally, we found a diameter range of 30-80 nm. These NWs were dispersed in Isopropyl Alcohol via a ~5 second sonication step and drop cast on 150 micron thick glass coverslip slides from Fisher Scientific. A 3 nm SiO2 interlayer was deposited via Atomic Layer Deposition (we assumed a ~1-2 nm native oxide layer) and served to prevent exciton quenching at the metal surface (see section 4.3) while further passivating

the Si nanowire. This was followed by metallization of 100 nm of Ag via electron beam evaporation (Thermionics). The resulting structure is an Ω-shaped metal nanocavity (Figure 4.2) capable of supporting surface plasmon polariton (SPP) modes.

There are three reasons for constructing this device in the Ω-cavity architecture as opposed to the core-shell geometry presented in Chapter 3. First, synthesis of the core-shell conformal coating requires up-standing nanowires on a substrate such that the entire nanowire surface is exposed to incoming deposition materials. Microfabrication for electronics usually involves stacking of ~2D layers, thus it is much more likely that application of this technology will use nanowires which are already dispersed on the substrate horizontally to allow for 2D fabrication. Second, these nanowires will likely require higher pump power intensities to perform accurate detection of the signal as Si is known to have a very low QY (see section 4.1). The core-shell geometry employs a very thin (15 nm) Ag shell, which is a trade off between being thin enough to allow light to couple into the nanowire, while thick enough to constitute a continuous Ag film and sustain SPP oscillations. Unfortunately, this film is not stable under intense laser irradiation and requires lower pump powers. The Ω-cavity employs a thick Ag film (100 nm), which may be pumped at higher intensities (>100 kW/cm^2) as the thicker Ag film is also good heat sink. In theory there is no dependence of the results presented in this work on the Ag film thickness, as long as the thickness of the film is greater than the skin depth of Ag (~15 nm at optical frequency), and thus there is no cross talk between SPP modes on the either the inner or outer interfaces of the Ag film. The third reason is more subtle, but as will be described below, the Ω-cavity sustains half-integer multiples of the SPP

wavelength as opposed to full integer multiples of the core-shell cavity and thus allows more SPP resonances in same spectral region.

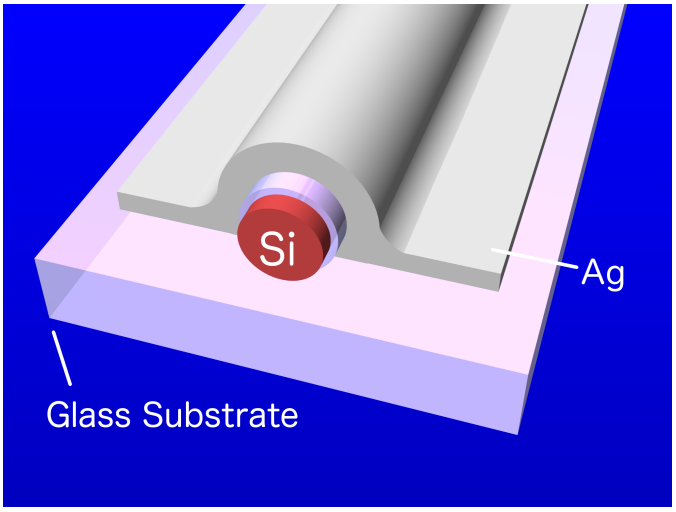

Figure 4.2 | Schematic of silicon nanowire coupled with silver nanocavity in "Ω" shaped configuration. The nanowire is conformally coated by 3 nm of SiO_2 via atomic layer deposition, followed by 100 nm of Ag using electron beam evaporation at a slow deposition rate (0.2 Å/s).[18]

4.3: Photoluminescence of Plasmonically-Coupled Si Nanowires

Photoluminescence measurements were performed on the same home-built setup described in Chapter 3, section 3.4.1. All measurements were performed at room temperature, and at pump intensity ~250 kW/cm^2. Measurements in this section were performed with the 457.9 nm laser line of a continuous wave (cw) argon-ion laser (Coherent) and the 355.7 nm line of a frequency-doubled femtosecond pulsed

Ti:Sapphire laser (Chameleon) to allow for UV excitation. The Ω-cavity was excited and measured through the SiO_2 substrate.

The conformal coating of nanowire with diameter, *d*=65 nm, is imaged in Figure 4.3a. When the nanowire was illuminated under cw excitation, we observed bright white-light (Figure 4.3b, c) from the excitation region (note, all light below 460 nm is filtered to avoid any signal from the laser). The photoluminescence spectrum of the bare nanowire features a response at noise level as expected from bulk silicon (Figure 4.3d, blue curve). The spectrum of the nanowire coupled with the plasmonic Ω-cavity (Figure 4.3d, green curve), on the other hand, reveals broad luminescence over the visible spectrum (from the laser line to ~1.75 eV or 708 nm). Again, there were no observable photon counts from the silicon nanowire without the Ag coating.

This experiment was repeated on another nanowire (*d*=45nm) under UV excitation (3.486 eV). The resulting photoluminescence spectrum again reveals a broad envelope, which starts at the laser line suggesting that the observed emission is indeed hot-carrier photoluminescence. We propose a hot photoluminescence mechanism (Figure 4.4b) where, as expounded in the previous chapter, excited charge carriers undergo two competing processes, thermalization to the minimum of the conduction band via non-radiative phonon scattering and scattering back into the light line (at k~0 or the Γ point) via LO-phonon scattering. Radiative recombination from high energy states above the conduction band minimum is possible if the spontaneous emission lifetime (~ns) becomes comparable to that of the non-radiative recombination process (<1ps), and if

there is a sufficient source of readily available phonons to participate in the scattering process (discussed below).[15,19]

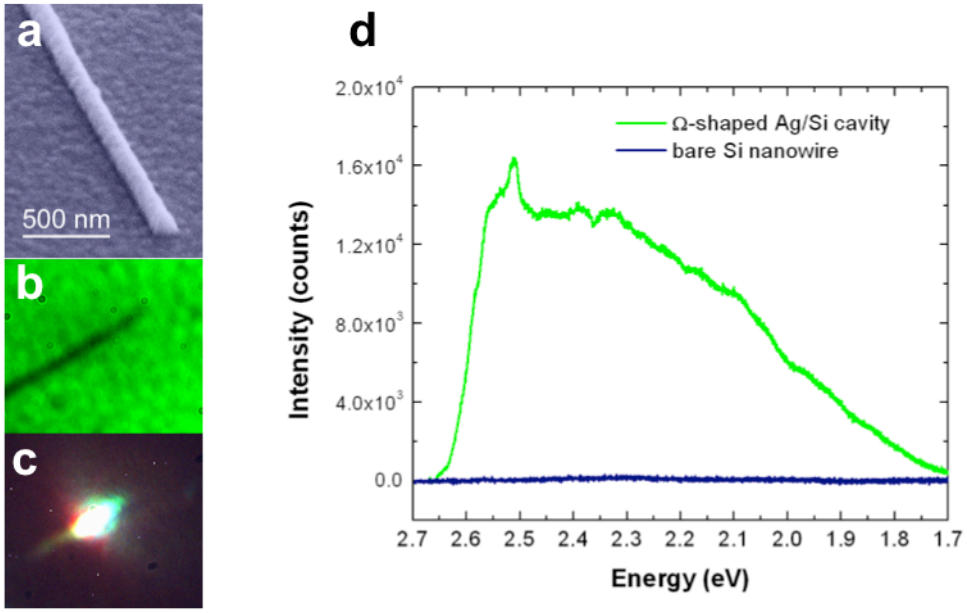

Figure 4.3 | Ω-cavity silicon and associated photoluminescence spectra. a) Scanning electron microscope micrograph of the Ag coated nanowire (Ω-cavity). b-c) Bright field optical microscope image of Ω-cavity and corresponding image under CW laser excitation. d) Photoluminescence spectrum of Ω-cavity (*d*=65 nm) and bare Si nanowire coated with ~5 nm SiO2 only. There were no observable counts above noise level from the the bare Si nanowire.[15]

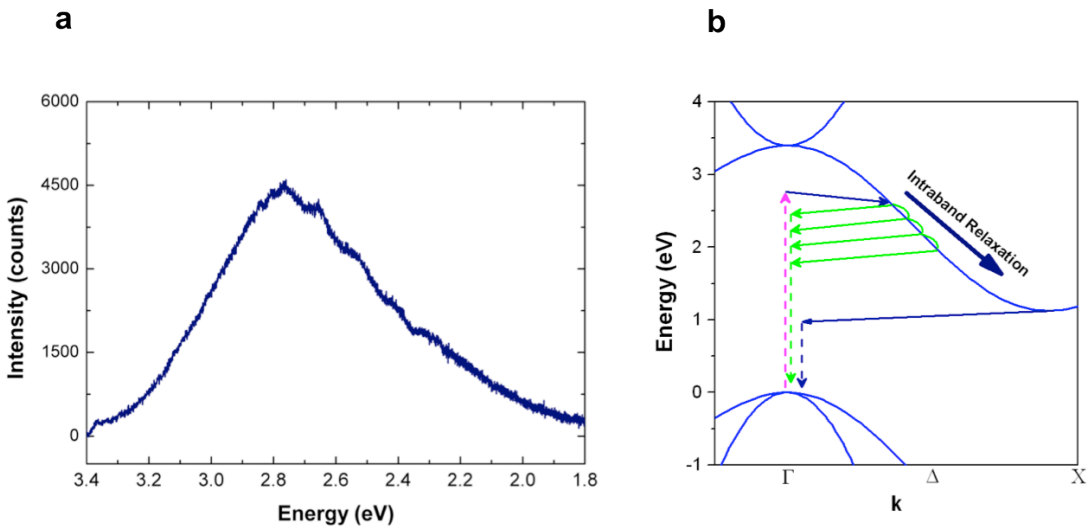

Figure 4.4 | UV excitation of Ω-cavity silicon nanowire and proposed hot photoluminescence mechanism. a) Photoluminescence from Ω-cavity silicon nanowire (*d*=45 nm) excited at 3.486 eV demonstrating broad luminescence up to the laser line. b) Schematic of electronic dispersion in Si depicting carrier generation, relaxation, and emission for thermalized carriers (blue curves) and a hot, i.e. non-thermalized carrier (green curves). Excited electrons relax rapidly along the conduction branch to the X-point via intra-band relaxation, which competes with LO-phonon scattering back to the light line (k~0), thereby leading to a broad photoluminescence spectrum.[15]

4.4: Size Dependent Photoluminescence Spectroscopy and FDTD Simulations of Plasmonically-Coupled Silicon Nanowires

First, the reader is referred to Chapter 1, section 1.4 for discussion on semiconductor nanowire modes and Chapter 3, section 3.5.1.1 for a review of the nomenclature for electromagnetic modes in this thesis work. As demonstrated in Chapter 4, the spectral position of WGM/leaky modes is sensitively dependent on nanowire diameter, thus to explore the effect of cavity size on hot luminescence, several plasmonically-coupled nanowires were measured. The photon counts of hot photoluminescence were highest for the d=70 nm nanowire (Figure 4.5a, magenta curve) and demonstrates a clear peak structure superimposed on the broad hot luminescence background. We postulate that the origin of the efficient emission channels is related to the phonon dispersion of Si and will be discussed in the following section. FDTD simulations of these nanowires (see Chapter 3, section 3.5.1 for simulation details) reveal several cavity modes, that are spectrally matched to the high efficiency emission channels and which themselves span the visible range (Figure 4.5a, blue curve).

In order to verify the role of cavity modes in mediating hot photoluminescence, systematic measurements made on plasmonically-coupled nanowires spanning the range d=30 nm-80 nm, which were combined and plotted (Figure 4.5b). Interestingly, the emission is strongest for nanowires at two different diameters, d=55 nm and d=70 nm, which hints at the role of cavity modes in the increased spontaneous emission process. Furthermore, samples in the same size range were simulated using FDTD (Figure 4.5c)

and their cavity spectra superimposed on the size dependent plot. Indeed, the cavity spectra are spectrally matched to highest efficiency emission channels observed at d=70 nm, at d=55 nm also. We refer to these as resonantly-sized cavities where the resonance is between high efficiency emission channels and the cavity modes.[15]

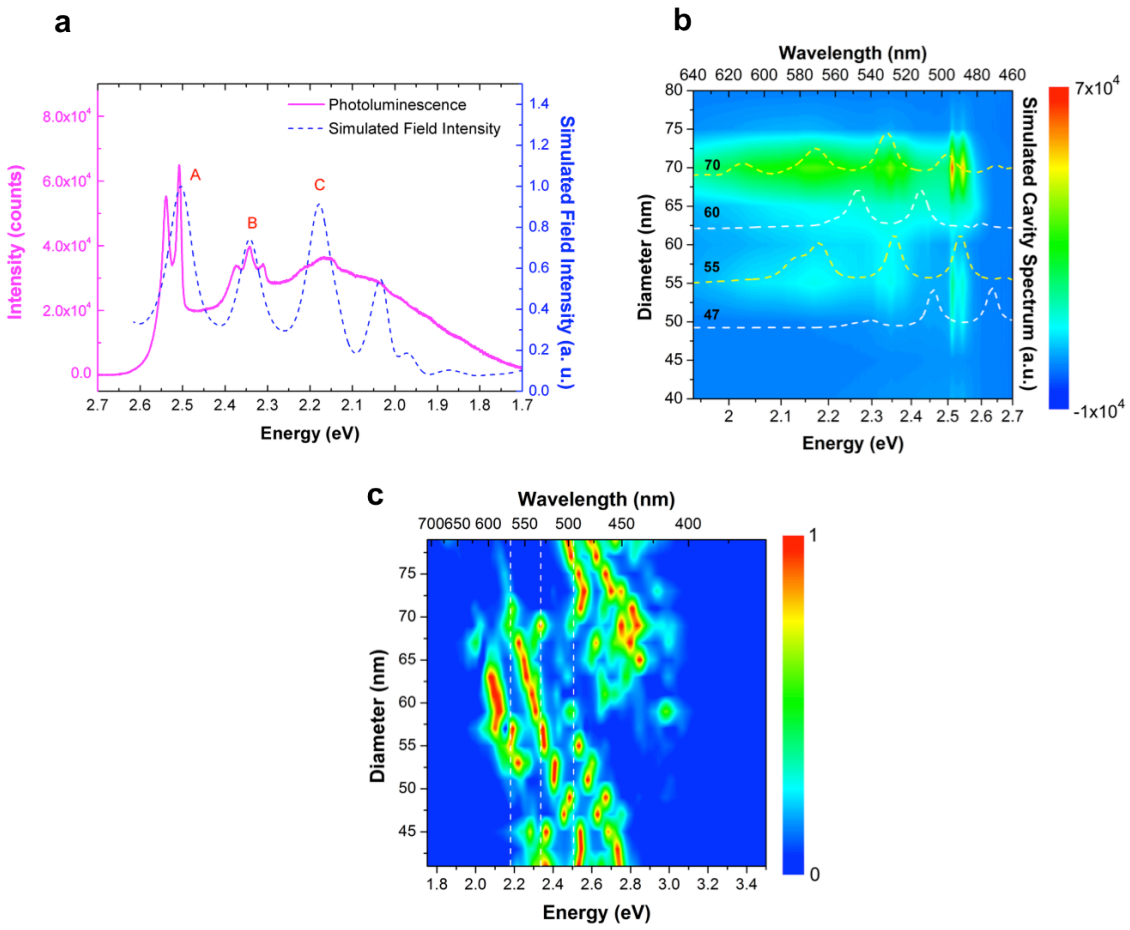

Figure 4.5 | Photoluminescence spectrum of resonantly sized cavity and experimental and simulated spectra of cavity electromagnetic modes as a function of nanowire diameter. a) Photoluminescence spectrum (magenta curve) of cavity at (d=70 nm) which corresponds to dimensions that are resonant with the cavity modes (blue curve). The high efficiency emission channels are labeled A, B, and C from high to low energy. b) Size-dependent photoluminescence spectra of Ω-cavity Si. The white dash lines represent selected off-resonance simulated cavity spectra taken from (c). The yellow dash lines represent resonant simulated cavity spectra corresponding to the experimentally measured size (d=70 and d=55 nm) and are also plotted in (c). c) Simulated spectra of cavity modes at various nanowire diameters in the range d=40 nm-80 nm. The white dash lines correspond to locations of the hot photoluminescence bands.[15]

Returning to analysis of mode structure, FDTD simulations (following a similar procedure to that of Chapter 3, section 3.5.1) reveal multiple equally-spaced cavity modes positioned at 2.505 eV, 2.342 eV, and 2.179 eV (Figure 4.6a-c), which are spectrally matched to the phonon-mediated hot photoluminescence peaks observed experimentally (Figure 4.5a, labeled A-C). The frequency-domain mode profiles, reveal highly confined SPP modes, at the Ag/SiO2 interface which occur at half integer multiples of the SPP wavelength (m=5, 4 and 3 for modes at 2.505 eV, 2.342 eV, and 2.179 eV respectively). In the core-shell geometry, propagation losses for SPP modes along the nanowire long-axis direction were found to be exceedingly high (10-30 dB/micron, see Chapter 3, section 3.5.2).[19] To confirm whether these are WGM-type modes or waveguided modes, we performed full 3D simulations which demonstrate a propagation length <200 nm (or about one wavelength) (Figure 4.6d) In other words, these modes propagate in the plane transverse to the long-axis only. The Quality factor of these modes is ~30 with an ultra-low mode volume of $\lambda^3 10^{-4}$ and calculated Purcell Factor $>10^3$ at 2.505 eV. The reader is referred to Chapter 3, section 3.5.2.1 for details of Purcell factor calculations and section 4.6 for a discussion of Purcell factor calculation in off-resonance conditions.[15]

In addition, the polarization characteristics are the same as discussed in Chapter 3, section 3.5, i.e. they are SPP modes with TE polarization propagating along the metal-dielectric interface. It should be noted that unlike the modes of the core-shell cavity, these are not Whispering Gallery Modes (WGM). The Ω-cavity breaks circular symmetry thereby eliminating the periodic boundary condition on the electromagnetic modes. In

other words, it is not possible to fit half-integer multiples of the SPP wavelength in the core-shell geometry due to the periodic boundary condition, which is not the case in the Ω-cavity. We exploit the broken symmetry of the Ω-cavity to obtain broadband emission (across the visible range). The modes are Fabry-Perot-type modes, which reflect back and forth between the two vertices of the Ω-cavity at half integer wavelength multiples. The following section will discuss the proposed origin of high efficiency emission channels in plasmonically-coupled silicon.

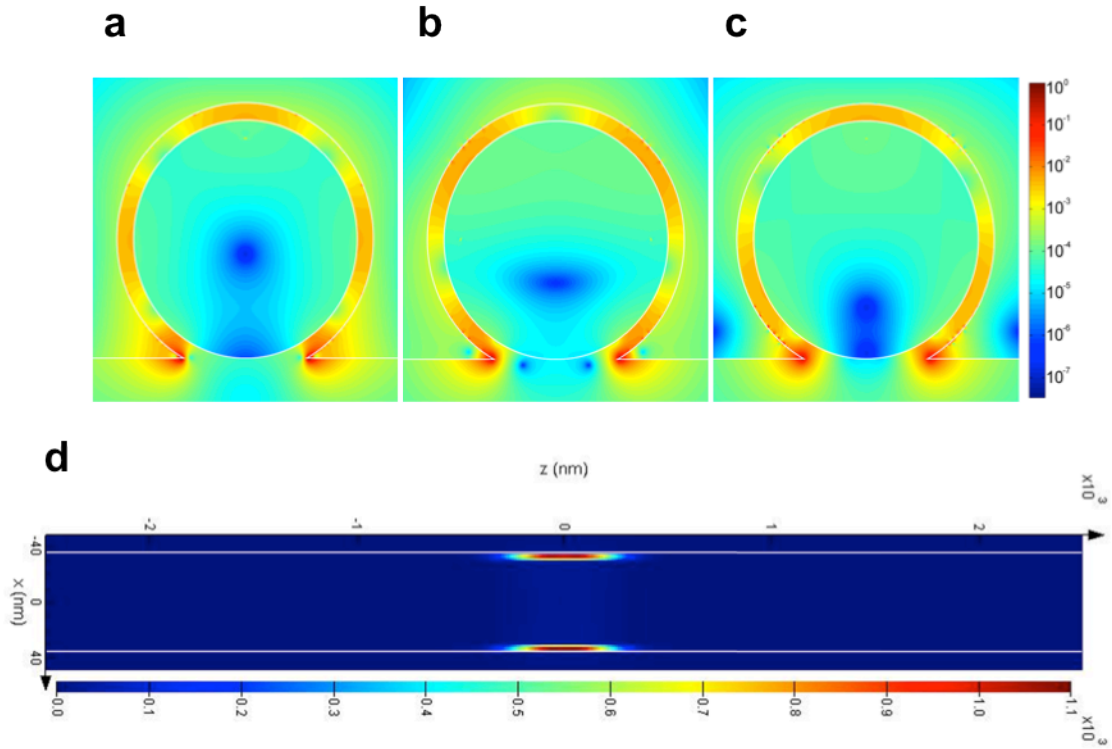

Figure 4.6 | Simulated cavity mode spectra of resonant-sized cavity (*d*=70 nm). a-c) Frequency domain profiles of the electric field intensity (log scale) of resonant peaks at a) 2.505 eV, b) 2.342 eV, and c) 2.179 eV respectively. d) Simulated field profile along the Si wire axis (corresponding to 2.505 eV, m=5 mode). The field profile is taken 15 nm below the top surface in the antinode regions of the electric field. The decay length is estimated to be ~200 nm.[15]

4.5: Hot-Carrier Radiative Recombination via Coupling with Phonons with High-Density of States.

Polarization dependent photoluminescence measurements were performed in an attempt to decouple the contribution from phonon-mediated hot photoluminescence and cavity modes. As discussed in section 4.4 the Ω-cavity modes are TE (electric field polarized *perpendicular* to nanowire long-axis) modes, thus the emission, if mediated by the SPP modes, should be polarized perpendicular to the nanowire long axis also. The TE polarized light emission of the *d*=70 nm nanowire **(**Figure 4.7a) highlights the hot photoluminescence peaks with a polarization ratio, ρ, of 0.56 where $\rho = \frac{I_{TE}-I_{TM}}{I_{TE}+I_{TM}}$. In other words ~70% of the emission is TE polarized. Separating the TE and TM polarized photoluminescence allows us to examine both cavity modes and hot luminescence events in a non-resonant case *d*=50 nm, Figure 4.7b) where the cavity modes are detuned from the hot luminescence peaks observed in the resonant case (see section 4.4). As expected, the cavity modes, "C" peaks, shift as a function of nanowire size and are well matched by simulation of the cavity spectra for a *d*=50 nm Ω-cavity. An interesting phenomenon is that the phonon-mediated hot luminescence, "P", peaks occur at similar energies as in the resonant case, pointing to a hot-carrier emission mechanism that is intrinsic to Si. Note, even though the "C" peaks are detuned from the hot luminescence peaks, they may still induce Purcell enhanced spontaneous emission, albeit at lower photon counts (see section 4.6).

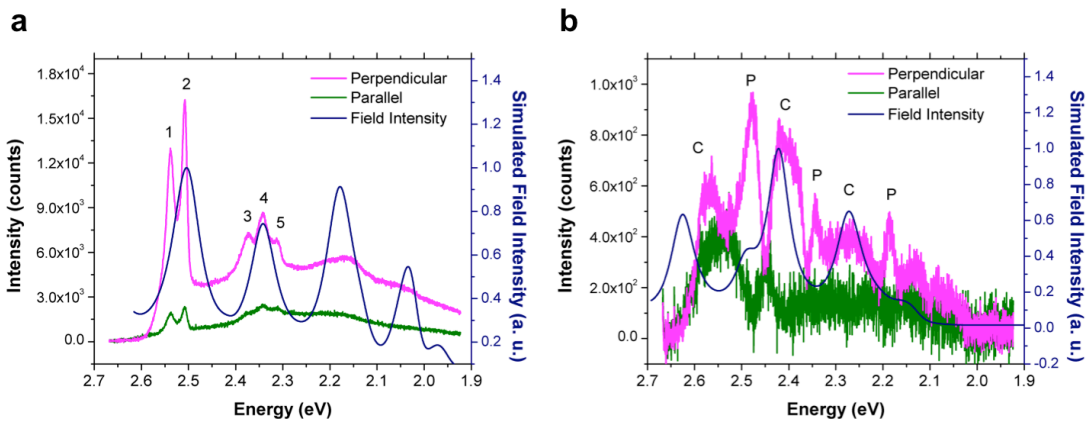

Figure 4.7 | a) Photoluminescence spectrum of resonant (*d*=70 nm) Ω-cavity Si for perpendicular and parallel polarizations (with respect to the nanowire long axis). Numbers 1-5 represent different phonon-mediated hot photoluminescence events. b) Photoluminescence spectrum for non-resonant (*d*=50 nm) cavity also for perpendicular and parallel polarizations. The perpendicular polarization reveals both cavity, "C", modes and hot photoluminescence, "P", modes. The cavity modes are confirmed by the simulated spectrum of the cavity electromagnetic modes.[15]

As we learned in Chapter 4, radiative recombination of carriers in indirect bandgap materials requires the participation of phonons to absorb the excess momentum, thereby returning carriers to the k~0 light line (see section 4.1.2). The phonon assisted process must conserve momentum, i.e. it will require scattering with phonons of momentum $q = -(q_e + \sum q_r)$, where q_e is the momentum of the charge carrier scattered to the conduction branch and q_r is the momentum of all phonons involved in thermalization of the charge carrier, thus bringing the carrier back to k~0. This event is limited by the availability of phonons and is therefore an improbable event, yet the probability of

radiative decay would be a function of the density of states of the phonon dispersion (i.e. their availability to participate in relaxation processes). We find that this probability increases greatly when the cavity SPP modes are resonant with hot-carrier emission that is mediated by phonons from the highest density of states (high-DOS) regions in the Si phonon dispersion.

Figure 4.8a is the phonon dispersion of Si along high-symmetry directions K, X and L (adapted from the work of Wei et. al.[20]). Along the <110> direction we can see a flat region in the transverse-optical, TO, phonon and transverse-acoustic, TA, phonon branches at ~$2\pi/a(0.6, 0.6, 0)$. This is a region of very high-DOS in the phonon dispersion relation. Now examining the electronic dispersion, we note that there are carriers with momentum equal to $2\pi/a(0.6, 0.6, 0)$ at ~2.51 eV (Figure 4.8b, blue line). These are carriers, which may relax back to the light line via a phonon with energy and momentum equal to the corresponding high-DOS phonon region. Applying the same analysis we identify two other high-DOS phonon regions: one at $\sim 2\pi/a(0.7, 0.7, 0)$ also between the Γ and K point for longitudinal-optical (LO) phonons and TA phonons and another at $\sim \pi/a(0.9, 0.9, 0.9)$ for TO and TA phonons near the L point (along <111> direction). These correspond to electronic states at ~2.18 eV and 2.34 eV respectively. Indeed, these predicted hot-PL bands agree well with experimentally measured hot-photoluminescence bands (Figure 4.5a).[15]

The absorption process in Si (i.e. when excited with a laser source) involves scattering with a phonon to the conduction band, followed by intra-band relaxation with

low momentum phonons. This either occurs via a 1-phonon step involving optical phonons near the Brillouin zone center (Γ-point) or 2-TA phonons with opposite momentum values at the zone boundaries.[21] Noting, the density of states is much higher for TA phonons than LA phonons at the zone boundary, we expect intra-band relaxation to be dominated by TA phonons. In theory we may use this information, coupled with known phonon energies to infer the type (optical or acoustic) and number of phonons involved in the hot photoluminescence process (i.e. each photoluminescence sub-peak), but this requires further experimentation and theoretical examination and is outside the scope of this study.

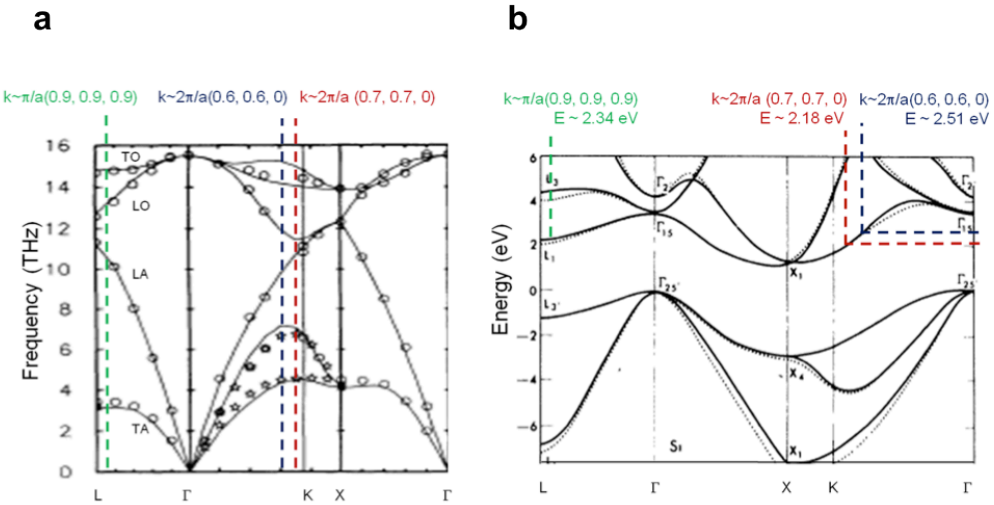

Figure 4.8 | a) Phonon dispersion of crystalline Si (adapted from Wei et.al.[20]) The dashed vertical lines indicate phonon modes in high density-of-states (~zero slope) regions. Electronic dispersion of Si (adapted from Chelikowsky et. al.[22]), where dashed lines demonstrate the corresponding electronic states at the same momentum values as high-DOS phonons from a). a) and b) are used to explain the hot photoluminescence bands.[15]

4.6: Purcell Enhancement in Off-Resonance Conditions

Thus far, the spontaneous emission enhancement (Purcell enhancement) has only been calculated for the condition of perfect resonance between the emitter and the cavity mode, i.e. the Purcell Factor. In reality, spontaneous emission enhancement would be lower than the Purcell Factor and will depend on the spectral mismatch (i.e. the amount of detuning between the cavity mode and emitter), spatial mismatch, polarization mismatch, and the finite linewidths of both the emitter and the cavity mode. Furthermore, as we have observed, even if the cavity mode is detuned from an emission channel, we may still observe enhanced spontaneous emission at a lower level (see previous section and section 4.4 on size dependent measurements). A more accurate representation of the spontaneous emission (SE) enhancement is as follows,

$$SE = F_p \frac{\gamma_c(2\gamma_e + \gamma_c)}{4(1-\omega_c/\omega_e)^2 + (2\gamma_e + \gamma_c)^2} \frac{|E(r)|^2}{|E_{max}|^2} \eta \qquad \text{Eq. 4.2}$$

where F_P is the Purcell factor, and ω_c and ω_e are the frequency of the cavity mode and the emitter respectively. γ_e (= $\Delta\omega_e / \omega$) and γ_c (= $\Delta\omega_c / \omega$) denote the decay rates of the emitter and the cavity mode, the inverse of which is the Quality factor. $\Delta\omega_e$ and $\Delta\omega_c$ are the linewidth of the emitter and the cavity mode respectively, and η is the polarization matching factor.[23] The Quality factor of the Ω-cavity is ~30 corresponding to a spectral linewidth of ~84 meV for the cavity modes (i.e. peak A in Figure 4.5a). The homogenous

broadening (linewidth) of the single hot photoluminescence peaks, on the other hand, is typically much smaller ~15 meV (i.e. peak 2 in Figure 4.7a). The polarization matching factor, η, was chosen as 2/3 noting only electric field components in the plane of the nanowire cross section may excite SPP modes. For the resonant size Ω-cavity, calculations were carried out for cavity modes at 2.51 eV (Purcell factor = 3688) and 2.34 eV (Purcell factor = 3457). These are represented by the two solid lines (blue and orange) as a function of spectral (energy) mismatch. The dashed lines represent the spectral position of the hot photoluminescence subpeaks (peaks 1-5 in Figure 4.9a). Peaks 1 and 2 belong to the first band (blue line) and peaks 3-5 belong to the second band (orange line). The intersection of the hot photoluminescence peaks with the detuned SE is therefore a more accurate Purcell factor value and is still $>10^3$ for energy mismatch up ~60 meV. Again, this highlights the applicability of surface plasmon-enhanced SE over a broad energy range due to the low Q-values of SP modes in plasmonic nanocavities (see Chapter 1, section 1.1). The value of the resonant Purcell factor was taken near the surface of the Si nanowire where it is highest (due to strongest modal overlap). For the non-resonant case (d=50 nm, Figure 4.7b) the SE enhancement was calculated for the mode at 2.42 eV, which has the highest Purcell factor value (2138) out of all the cavity modes and is expected to dominate SE (Figure 4.9 b, solid blue curve). In the next section we will quantify the enhancement in the quantum yield of silicon as a result of Purcell enhancement.

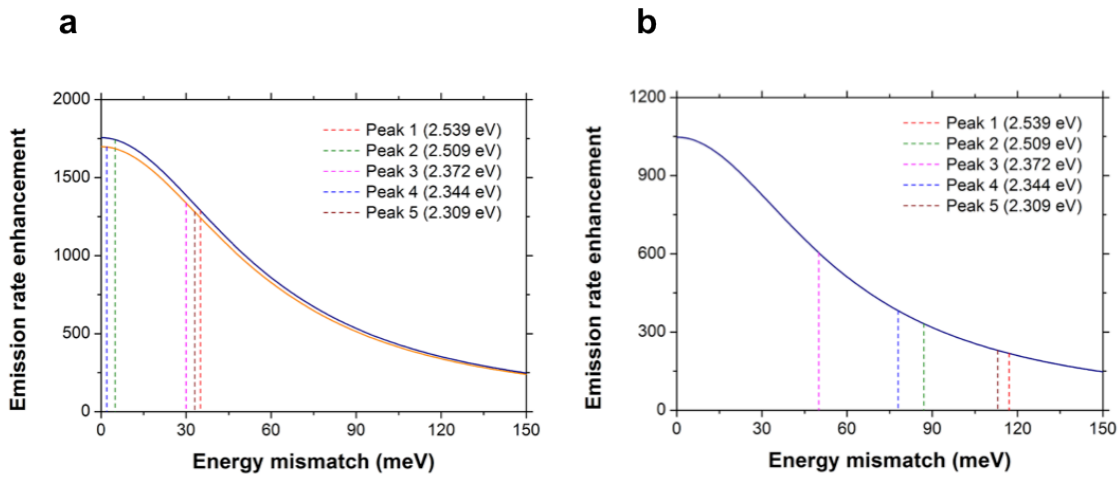

Figure 4.9 | Spontaneous emission enhancement as function energy mismatch between Ω-cavity mode and phonon-mediated hot photoluminescence state for a) resonant size nanowire (d=70 nm) and b) non-resonant size nanowire (d=50 nm). The vertical dash lines represent the positions of the hot photoluminescence bands reported in Figure 4.7a and intersect with the curve corresponding to spontaneous emission enhancement of those states.[15]

4.7: Enhanced Quantum Yield of Plasmonically-Coupled Silicon

Thus far, we have demonstrated the ability to transform silicon from a dark material, to a light-emitting material by coupling with a plasmonic nanocavity. Ideally, we would like to provide a measure of the internal quantum yield (QY), which quantifies the efficiency with which a material converts excited carriers to emitted photons. As a reminder, the QY of bulk silicon is 10^{-4}-10^{-6} (see section 4.1). In order to obtain an accurate estimate of the quantum yield, we must first know the power incident and absorbed by the silicon and also the collection efficiency of our measurement setup. The collection efficiency of the fiber-coupled spectrometer with a charge-coupled device (CCD) detector was obtained by measuring a known laser power and comparing the known power to the measured integrated counts (taking into account the response curve of the CCD). The collection efficiency was estimated to be 1%. From the integrated counts of the photoluminescence spectrum of the resonant size Ω-cavity Si sample, the measured radiated power through the objective was 0.8 nW. The far-field out-coupling efficiency was determined via full three-dimensional FDTD calculations. For the Ω-cavity (d=70nm, l=8 μm), the average far-field out-coupling efficiency is 0.059% throughout the entire emission spectral range after considering the numerical aperture of our objective. We estimate the actual power emitted from Si to be 1.4 μW. An absorption efficiency of 1% was calculated via FDTD using a 2 μm spot-size (FWHM) and a laser wavelength of 457.9 nm, resulting in 100 μW of absorbed power at 10 mW of incident laser power. Therefore, the quantum yield of 1.4% was estimated by taking the ratio of the emitted power from Si (1.4 μW) to the absorbed power in Si (100 μW).

4.8: Conclusions

This work presents surface plasmon-enhanced hot photoluminescence as a viable method of obtaining light emission from Si. As discussed in previous sections, due to the ubiquity of silicon in modern technology we expect such findings to play an important role in the development of semiconductor technology. The ability to obtain visible light at a reasonable quantum yield (> 1%) from Si at length scales that are compatible with contemporary electronics (>20 nm) is a significant step towards the integration Si-based photonics with conventional electronics. From a scientific point of view, this work highlights the interplay of three (quasi)-particle systems: charge carriers, phonons, and cavity plasmons and will require a substantial amount of theoretical and experimental work to unravel the exact hot photoluminescence mechanism. Furthermore, the previous two chapters lay out what appears to be a general technique of engineering light emission from semiconductor materials, as it was applied to two materials with starkly different electronic structures, namely a light emitting material (CdS) with a direct bandgap and a dark material (Si) with an indirect bandgap. A hot photoluminescence process, which is mediated by phonons, should be independent of the excitation energy; a property that should be verified by variable energy excitation experiments. Moreover, we would like to perform temperature-dependent measurements as a means to separate hot photoluminescence from Resonant Raman Scattering (see Chapter 3, section 3.4.3). Finally, the role of the electronic structure of silicon in mediating hot luminescence should be clarified. The next chapter will be dedicated to variable energy and temperature dependent studies of plasmonically-coupled silicon nanowires.

References

1 Zhang, J., Li, D. H., Chen, R. J. & Xiong, Q. H. Laser cooling of a semiconductor by 40 kelvin. *Nature* **493**, 504-508, doi:Doi 10.1038/Nature11721 (2013).

2 Pavesi, L., Lockwood, D. J. & Alumni and Friends Memorial Book Fund. *Silicon photonics*. (Springer, 2004).

3 Ming, T., Chen, H. J., Jiang, R. B., Li, Q. & Wang, J. F. Plasmon-Controlled Fluorescence: Beyond the Intensity Enhancement. *J Phys Chem Lett* **3**, 191-202, doi:Doi 10.1021/Jz201392k (2012).

4 Liang, D. & Bowers, J. E. Recent progress in lasers on silicon. *Nature Photonics* **4**, 511-517, doi:Doi 10.1038/Nphoton.2010.167 (2010).

5 Cullis, A. G. & Canham, L. T. Visible-Light Emission Due to Quantum Size Effects in Highly Porous Crystalline Silicon. *Nature* **353**, 335-338, doi:Doi 10.1038/353335a0 (1991).

6 Wilson, W. L., Szajowski, P. F. & Brus, L. E. Quantum Confinement in Size-Selected, Surface-Oxidized Silicon Nanocrystals. *Science* **262**, 1242-1244, doi:Doi 10.1126/Science.262.5137.1242 (1993).

7 Brongersma, M. L. *et al.* Tuning the emission wavelength of Si nanocrystals in SiO2 by oxidation. *Applied Physics Letters* **72**, 2577-2579, doi:Doi 10.1063/1.121423 (1998).

8 Walavalkar, S. S. *et al.* Tunable Visible and Near-IR Emission from Sub-10 nm Etched Single-Crystal Si Nanopillars. *Nano Letters* **10**, 4423-4428, doi:Doi 10.1021/Nl102140k (2010).

9 Xu, Q. F., Schmidt, B., Pradhan, S. & Lipson, M. Micrometre-scale silicon electro-optic modulator. *Nature* **435**, 325-327, doi:Doi 10.1038/Nature03569 (2005).

10 Fan, L. *et al.* An All-Silicon Passive Optical Diode. *Science* **335**, 447-450, doi:Doi 10.1126/Science.1214383 (2012).

11 http://www.intel.com/content/www/us/en/research/intel-labs-silicon-photonics-research.html.

12 Goldman, J. R. & Prybyla, J. A. Ultrafast Dynamics of Laser-Excited Electron Distributions in Silicon. *Physical Review Letters* **72**, 1364-1367, doi:Doi 10.1103/Physrevlett.72.1364 (1994).

13 Sabbah, A. J. & Riffe, D. M. Femtosecond pump-probe reflectivity study of silicon carrier dynamics. *Physical Review B* **66**, doi:Doi 10.1103/Physrevb.66.165217 (2002).

14 de Boer, W. D. A. M. *et al.* Red spectral shift and enhanced quantum efficiency in phonon-free photoluminescence from silicon nanocrystals. *Nature Nanotechnology* **5**, 878-884, doi:Doi 10.1038/Nnano.2010.236 (2010).

15 Cho, C.-H., Aspetti, C. O., Park, J. & Agarwal, R. Silicon coupled with plasmon nanocavities generates bright visible hot luminescence. *Nat Photon* **7**, 285-289 (2013).

16 Prokofiev, A. A. *et al.* Direct Bandgap Optical Transitions in Si Nanocrystals. *Jetp Lett+* **90**, 758-762, doi:Doi 10.1134/S0021364009240059 (2009).

17 Yu, P. Y. & Cardona, M. *Fundamentals of semiconductors : physics and materials properties*. 3rd edn, (Springer, 2001).
18 Piccione, B., Aspetti, C. O., Cho, C.-H. & Agarwal, R. Tailoring light-matter coupling in semiconductor and hybrid-plasmonic nanowires. *Reports on Progress in Physics* **77**, 1-20 (2014).
19 Cho, C.-H., Aspetti, C. O., *et al.* Tailoring hot-exciton emission and lifetimes in semiconducting nanowires via whispering-gallery nanocavity plasmons. *Nat Mater* **10**, 669-675 (2011).
20 Wei, S. Q. & Chou, M. Y. Phonon Dispersions of Silicon and Germanium from 1st-Principles Calculations. *Physical Review B* **50**, 2221-2226, doi:Doi 10.1103/Physrevb.50.2221 (1994).
21 Racek, W., Bauer, G. & Kahlert, H. Dynamic Measurement of Hot-Electron Magnetophonon Effect in N-Insb at 11-K. *Physical Review Letters* **31**, 301-304, doi:Doi 10.1103/Physrevlett.31.301 (1973).
22 Chelikowsky, J. R. & Cohen, M. L. Electronic-Structure of Silicon. *Physical Review B* **10**, 5095-5107, doi:Doi 10.1103/Physrevb.10.5095 (1974).
23 Ryu, H. Y. & Notomi, M. Enhancement of spontaneous emission from the resonant modes of a photonic crystal slab single-defect cavity. *Optics Letters* **28**, 2390-2392, doi:Doi 10.1364/Ol.28.002390 (2003).

Chapter 5. Studies of Hot Photoluminescence in Plasmonically-Coupled Silicon via Variable Energy Excitation And Temperature Dependent Spectroscopy

5.1: Introduction

5.1.1: Motivation

The previous chapter was dedicated to the demonstration of super-bandgap (hot) photoluminescence in the visible spectral range from non-quantum confined silicon nanowires.[1] The spontaneous emission rate of silicon (and thereby the emission intensity) was enhanced by coupling silicon to highly confined modes of a plasmonic nanocavity using methods similar to those previously applied to cadmium sulfide, a direct bandgap material[2] (see Chapter 3). However, emission from non-thermalized carriers or "hot-luminescence" has similar spectral characteristics to resonant-Raman scattering (RRS)[3], such as scattering peaks that occur at fixed phonon energies from the laser line, even though hot-luminescence and RRS are fundamentally different processes; the former involves real electronic transitions whereas the latter does not. Thus, experimental verification of hot photoluminescence in silicon, and potentially other plasmonically-coupled indirect-bandgap materials, is of fundamental importance.

By integrating silicon nanowires (~150 nm diameter, 20 micron length), with an Ω-shaped plasmonic nanocavity we are able to generate broadband visible luminescence,

which is induced by high-order hybrid nanocavity-surface plasmon modes. The nature of this super-bandgap emission is explored via photoluminescence spectroscopy studies performed with variable laser excitation energies (1.959 eV to 2.708 eV) and finite difference time domain simulations. Furthermore, temperature-dependent photoluminescence spectroscopy, in addition to steady-state spectroscopic evidence, demonstrates that the observed emission corresponds to radiative recombination of un-thermalized (hot) carriers as opposed to a Resonant Raman process.

5.1.2: Review of Light Emission in Silicon

Silicon, due to its indirect bandgap, converts excited charge carriers to heat much more readily than to light. In other words, silicon is a "dark" material in comparison to direct bandgap semiconductors, which is the main impediment to the application of Si for light emitting devices. The exceptionally low quantum yield of silicon stems from the large momentum mismatch between its conduction minima and valence band maxima.[4] To be more specific, it is this momentum mismatch which is predominantly responsible for a slow radiative recombination lifetime of milliseconds once carriers relax to the conduction band minimum (near the X-point), corresponding to a (theoretical) radiative quantum yield of 10^{-6}.[5] The low levels of light emission may be circumvented in sub-10 nm quantum confined silicon nanocrystals,[6,7] or nanoporous structures but this introduces significant new challenges in their integration with conventional electronic devices.[8-10] Previous work has demonstrated efficient emission in bulk silicon diodes (up to 6% at room temperature)[11] where the emission is enhanced by (1) applying a bias, which

exponentially increases the equilibrium photon occupation probability,[12] (2) patterning the surface to enhance both absorption and emission,[13] and (3) using pristine float-zone silicon to suppress non-radiative scattering centers[13]. In addition to the fabrication costs of these devices, significant limitations include its restriction to band-edge emission (1.12 eV) and slow modulation rates; the recombination lifetime is still in the millisecond range compared to nanoseconds in most direct bandgap materials.[14,15]For a comprehensive overview of the dynamics of excited charge carriers in silicon and the light emission process, the reader is referred to section Chapter 4, section 4.1.2.

5.2: Experimental

Silicon nanowires were integrated with plasmon nanocavities (Figures 5.1a, b) following a procedure similar to that detailed in Chapter 4, section 4.2. However, in contrast to the previous study, large (d ~150 nm, L ~20 micrometers) commercially obtained silicon nanowires (Sigma Aldrich) were used. These nanowires demonstrate superior uniformity in their morphology, while their increased diameters (compared to *d*=30 nm–80 nm) result in higher order (plasmonic) cavity modes. High resolution transmission electron microscopy reveals a native oxide layer on these nanowires of 1.5-2.5 nm thickness (Figure 5.1c), which is used as an insulating interlayer to separate the active material from the metal and thereby prevent non-radiative recombination of charge carriers at the metal surface.[16] This layer is also used to sustain high intensity surface plasmon fields in the gap between the metal and the silicon core (Figures 5.1d, e). The reader is referred to Chapter 1, section 1.3 and Chapter 3, section 3.3 for discussion on

the role of the insulating interlayer in interfacing active materials with plasmonically active metals. A thick silver film (300 nm) was deposited atop the silicon nanowires using both thermal and electron beam evaporation techniques. Thermal evaporation was used because it uses a tungsten boat to hold silver source as opposed to a graphite crucible, thereby eliminating a potential source of carbon contamination, which can be an issue with silver (see section 5.5.2). During thermal evaporation, particular care was taken to ensure a clean environment by first coating the entire chamber with a 200 nm layer of silver (base pressure of 10^{-6} Torr) followed by deposition on the Si nanowires. Samples synthesized using both techniques yield similar results, though for consistency all samples studied for this manuscript were synthesized with a single technique (electron beam evaporation). This highlights precautions taken during silver deposition, which is key for supporting surface plasmon modes in the vicinity of the silicon core, which can span the visible spectral range. Finite-difference-time-domain simulations of the silicon-oxide-silver cavity demonstrate these nanowires (150 nm diameter) are capable of sustaining high order ($m > 7$) hybrid surface plasmon modes which can significantly enhance spontaneous emission in silicon via the Purcell effect.[1,2]

Optical characterization of individual nanowire samples with Ag-based plasmonic nanocavities was carried out using a home-built microscope setup equipped with a 60X, 0.7 NA objective (Nikon) that has a spatial resolution of ~600 nm. Variable-energy excitation experiments were conducted with 5 different laser lines obtained from a continuous wave argon-ion laser including: 457.9 nm, 488 nm, 496.5 nm, 501.7 nm, 514.5 nm, and a He-Ne laser (633 nm) corresponding to an energy range (1.959 eV -

2.708 eV). The incident photon flux at each wavelength was maintained constant by focusing 1 mW of incident laser power to a ~1 μm spot at all wavelengths. Photoluminescence spectra were collected using a spectrometer (Acton) coupled to a cooled CCD (charge-coupled device) with a spectral resolution of 0.1 nm. Temperature dependent measurements were conducted using a liquid nitrogen cooled cryostat (for temperatures between 77 K and room temperature). We measured plasmonically-coupled silicon nanowires with diameters ranging from 148 nm to 156 nm and at all the laser energies mentioned above.

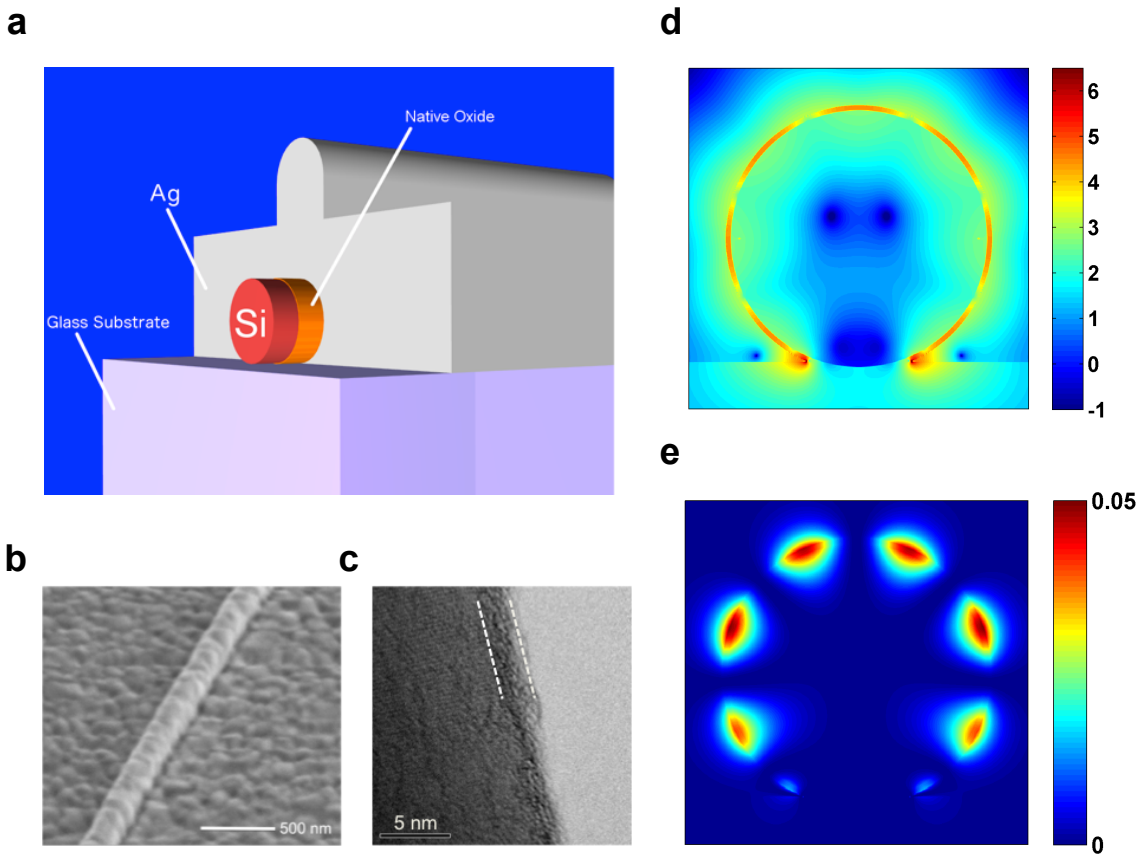

Figure 5.1 | a) Schematic of silicon nanowire integrated with a 300 nm thick silver film to form a plasmonic nanocavity (drawn to scale). The native oxide of silicon (SiO_x) is used to separate the active silicon core from the silver shell. b) Scanning electron microscope (SEM) of silver coated silicon nanowire. c) Transmission electron microscope (TEM) image of a representative bare silicon nanowire demonstrating 1.5-2.5 nm of native oxide (denoted by dashed white lines) on the nanowire surface. d) Frequency domain spatial distribution of the electric field intensity in Ω-cavity Si (d=150 nm) demonstrating high order (m=9) mode (obtained via FDTD simulation) and e) corresponding magnetic field intensity.[17]

5.3: Variable Energy Excitation and Photoluminescence Spectroscopy of Plasmonically-Coupled Silicon Nanowires

The photoluminescence spectra of a single plasmonically-coupled silicon nanowire of diameter *d*=150 nm are plotted vs. (absolute) emission energy (Figure 5.2a) for different laser excitation energies. The emission envelope spans the visible range and appears to have a fixed spectral width that is independent of the excitation energy. Plotting the same spectra vs. energy shift from the laser line reveals two high intensity subbands labeled A and B (Figure 5.2b), which occur at a fixed distance from the laser line, and are consistent with the previously reported data obtained with 2.708 eV excitation,[1] which was the focus of the previous chapter. The extent of the emission envelope and the occurrence of high intensity bands are related to the electronic structure and phonon dispersion of silicon respectively, which are discussed below.

In indirect bandgap semiconductors, once the excited charged carrier is scattered to the electronic branch with momentum q_e and relaxes along the electronic branch by scattering with phonons with momentum q_r, radiative recombination at the light line (with momentum q ~ 0) will require scattering with phonons of momentum $q = -(q_e + \sum q_r)$ to satisfy momentum conservation (Figure 5.2c).[18] We refer the reader to chapter 4, sections 4.3 and 4.5 for an introductory discussion of phonon-mediated hot photoluminescence in silicon. It should be noted that both energy and momentum must be conserved, thus the emitted photon will have energy $E = E_{excited} - \sum E_q$, where $E_{excited}$ is the excitation energy and $\sum E_q$ is the total energy of all phonons involved in scattering.

In silicon, intraband relaxation typically occurs on a picosecond timescale[19] [20] while radiative recombination has a ~10 ns lifetime near the direct bandgap[21]; thus radiative recombination is normally observed from carriers that thermalize near the minimum of the conduction band (near X point) (Figure 5.2c, blue curves). The spontaneous emission rate of silicon nanowires, on the other hand, may be enhanced by up to ~10^2-10^3 via the Purcell effect due to highly confined hybrid plasmonic-cavity modes[1] thereby making spontaneous emission competitive with the intraband relaxation process and enabling luminescence from non-thermalized states, i.e. hot-photoluminescence.

This competition between intraband relaxation and radiative recombination (Figure 5.2c, green curves) results in a broad emission envelope (Figure 5.2a) as carriers scatter back to the almost vertical photon dispersion line near q~0 (also known as the light line), which leads to radiative recombination, but also as the carriers continue relaxing along the conduction bands. The limited number of available relaxation channels in the electronic dispersion is responsible for the apparent emission cut-off at ~2 eV. For all excitation energies, examining the electronic structure of silicon, we note the existence of multiple pathways for the relaxation of the excited carrier, i.e. towards the two local conduction band minima near the X-point (1.12 eV) and the valley at the L-point (~2.1 eV).[22] Based on momentum mismatch between the light line at q~0 and the electronic branch, the two most likely relaxation pathways (towards X and L points) are depicted in Figure 5.2c. A carrier excited with at high energy (> 2.1 eV) may relax towards all available conduction band minima, yet once the energy of the excited carrier is < 2.1 eV, relaxation towards the L-point will no longer be possible leading to less radiative

recombination events, and thus a fixed spectral extent of the emission region. In addition, carriers excited with energy < 2.1 eV may only be absorbed to the conduction band along the X and K points (near the conduction band minima), which are also electronic states that have high-momentum mismatch from the light line (at q~0). Thus, we expect lower counts from these states due to both the lower number of emission channels and also the low availability of phonons required to scatter back to the light line from near the X point (see discussion of phonon mediated hot-luminescence below). We note that hot emission from states below the L-point bandgap is still possible, albeit at lower counts (Figure 5.3a) due to the requirement of phonons with high density of states (high-DOS) (see discussion below). Indeed, excitation at 1.959 eV yields a nearly background level spectrum (Figure 5.2b, yellow curve), suggesting the involvement of real electronic states for both absorption and emission. As illustrated in Figure 5.2c it can be seen that hot-photoluminescence (like thermalized emission) is also an indirect process and requires phonon scattering to satisfy momentum conservation. Depending upon the excitation energy, excited carriers can occupy the available electronic branches (towards X and L points), and they can emit light through the phonon-assisted recombination process during intraband relaxation. However, for excitation at 1.959 eV, the electronic branch towards L point becomes inactive, and the excited carriers in the conduction band along the X point have momentum values which do not correspond to that of phonons with high-DOS,[1] thus giving rise to the low radiative quantum yield.

The high intensity subbands (Figure 5.2b, labeled A, B) occur at a fixed energy separation from the laser line and thus are evidence of events, which depend on phonon

scattering rather than decay from fixed electronic states. Though the most likely phonons that can participate in this process would be those that have the highest density of states in the phonon dispersion of Si,[1] labeling of the individual subpeaks within these bands is a significant theoretical problem, which should incorporate potential effects of phonons at the SiO_2-Si interface which are known to play a role in device physics,[23 24] coherent phonons due the high fields involved,[25] and correspondingly large phonon population numbers. Still potential hot-luminescence pathways are discussed below.

The phonon dispersion of silicon features several flat regions in the phonon dispersion,[26] which correspond to phonons with high-density of states. For the experimentally observed hot luminescence range between 2.6 and 2.0 eV (band A), taking into account the electronic dispersion of silicon, the corresponding high-DOS regions of the phonon dispersion are observed near K- and L- points. The high-DOS transverse optical (TO) phonons around the K-point correspond to the energies between 56 - 64 meV, while those around the L-point correspond to 60 meV. In addition, the high-DOS transverse acoustic (TA) phonons can be found near the K- and L-points with the energies of 19 and 14 meV, respectively. Thus, the high intensity bands (A and B) could originate from the hot carrier transition assisted by the various pathways of high-DOS phonons. For example, taking into account at least 1 TO phonon to scatter to the electronic dispersion, one for intra-band relaxation, and another for scattering back to the light line, we expect a high intensity band at about 190 meV shift from the laser line (band A). Similarly, hot carrier emission involving 6 TO phonons can result in a high intensity band at ~360 meV shift (band B). However, it should be noted that the above

pathways are representative cases, and the high intensity bands would be attributed to a summation of the various combinations of the high DOS phonons including TO and TA along with many other pathways involving slightly lower DOS phonons. These would be the most likely phonons to participate in radiative recombination and should result in the same high intensity bands regardless of the excitation energy ranging from 2.708 to 2.410 eV. Plotting the photoluminescence spectra of the *d*=150 nm plasmonically-coupled nanowire vs. energy shift from the laser line (Figure 5.2b), we observe broad high-intensity bands at ~190 meV and ~360 meV as expected from high-DOS phonons in silicon.

In addition, since the phonon dispersion around the high-DOS states is relatively flat, we also expect scattering from several electronic states which satisfy both momentum and energy conservation with a range of high-DOS phonons. Indeed, we observe variation of peak positions in band A by as much as 20 cm^{-1} (3 meV) when examining band A of a single 150 nm nanowire at various excitation energies (Figure 5.3b, c). We observe even greater scatter in peak positions (40 cm^{-1} or 5 meV) as a function of nanowire size at a single excitation energy of 2.541 eV (Figure5.3d, e), again a reflection of the fact that high-DOS phonons from a relatively broad region of the phonon dispersion may be involved in the hot-photoluminescence process. Indeed, a similar mechanism of hot photoluminescence was recently observed in organic dye molecules, where surface-plasmon enhanced spontaneous emission results in a series of peaks at fixed vibrational mode energies (also revealed by variable energy excitation)

superimposed on a broadband emission envelope which is restricted due to availability of electronic states.[27]

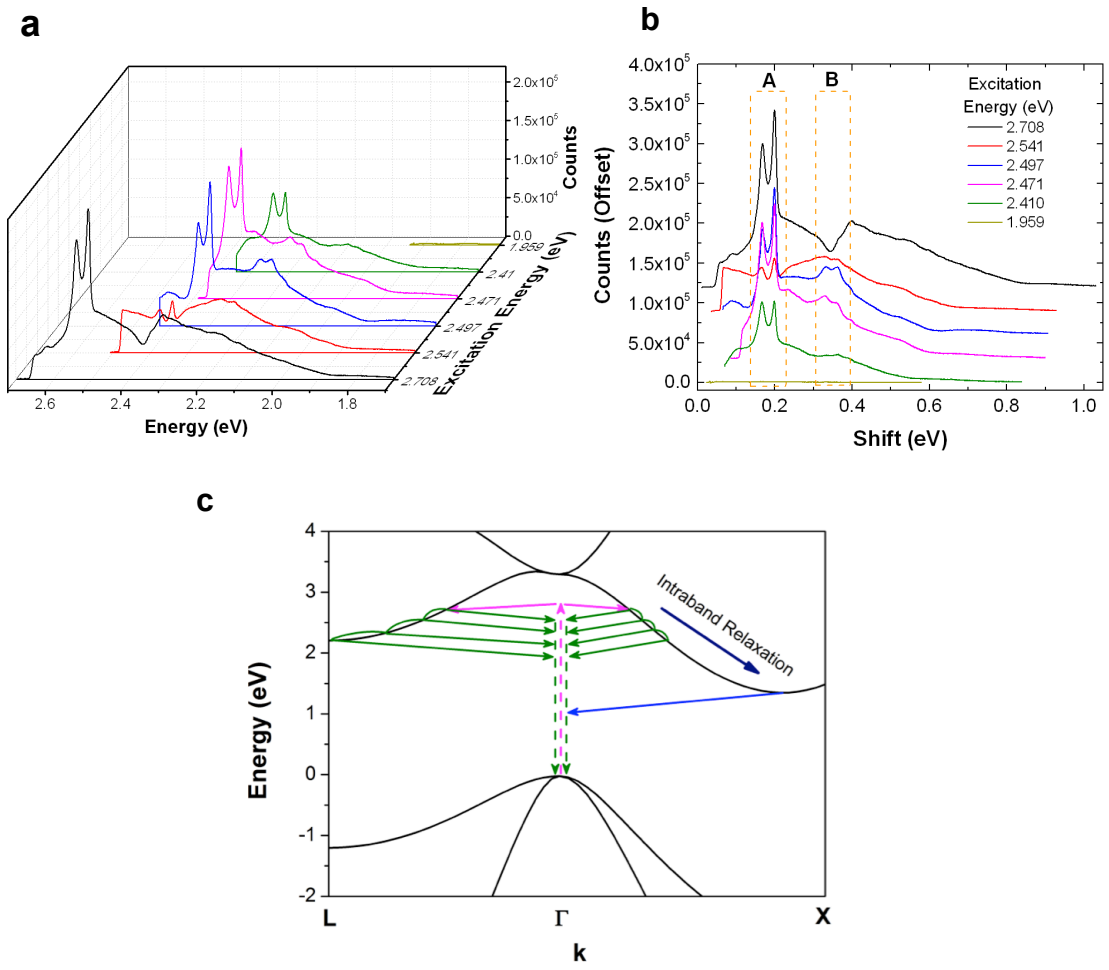

Figure 5.2 | Photoluminescence spectrum of plasmonically-coupled silicon nanowire (d=150 nm) plotted vs. a) absolute emission energy and b) energy shift from the laser line for various excitation energies in the range 1.959 eV-2.708 eV. Spectra in (b) are plotted with a constant offset of 2×10^3 counts for clarity. The dashed boxes labeled A and B denote high-intensity emission bands. c) Schematic of the electronic dispersion of silicon featuring carrier excitation (magenta arrows), intra-band relaxation and hot-luminescence (green arrows) and radiative recombination from thermalized carriers (blue arrows). This process is examined for relaxation towards the selected conduction band minima at both the X-points (1.12 eV) and L-points (~2.1 eV).[17]

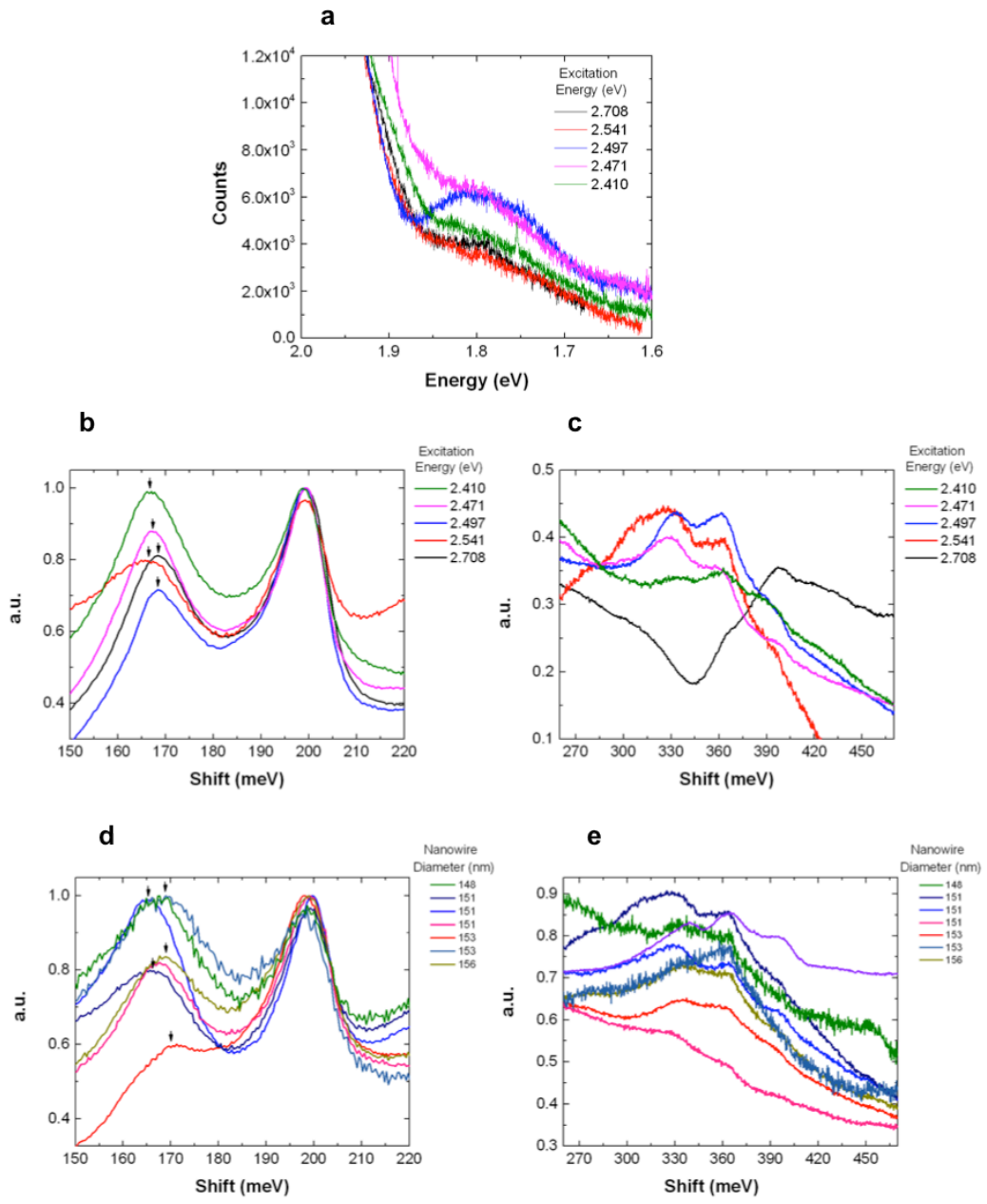

Figure 5.3 | a) Magnified photoluminescence spectra of *d*=150 nm plasmonically-coupled silicon nanowire in low energy region demonstrating emission below the silicon bandgap at the L-point. (b-e) Variation in spectral positions of subpeaks in photoluminescence spectrum of plasmonically-coupled silicon nanowire. b) variation in band A and c) band B as a function of excitation energy for a single silicon nanowire size (*d*=150 nm). d) variation in spectral positions of band A and e) band B for several nanowire sizes as a function of excitation energy. Black arrows denotes location of first high intensity peak.[17]

5.4: Electromagnetic Properties of High Order Modes in Large Plasmonically-Coupled Si Optical Cavities and their Role in Mediating Photoluminescence

5.4.1: Relationship between Mode Order and Quality Factor of WGM-Type Modes

It should be noted that the Purcell-enhanced spontaneous emission of silicon is a highly complex function of the spectral and spatial overlap between cavity modes and states that satisfy momentum and energy conservation, thereby involving three (quasi)-particles, i.e., plasmons, charge carriers and phonons. Noting that cavity modes for a particular nanowire are spectrally fixed, we expect there to be an excitation energy dependent modulation of the higher intensity emission bands. As discussed above, these bands occur at fixed energy shifts from the laser line (i.e. bands A and B), thus their spectral positions will change with the exciting laser and be tuned in and out of resonance with the cavity modes which are spectrally fixed for any given geometry. Both the broad emission envelope and the subbands are expected to be modulated as a function of the excitation energy.

In order to explore the cavity modes responsible for modulating the emission envelope, we performed finite-difference-time-domain simulations of all experimentally measured samples. The frequency domain response of the sample was obtained by averaging the Fourier transforms of the time domain fields due to all 3 orthogonal polarizations; that is two orthogonal polarizations in the plane of the nanowire cross section and a polarization along the nanowire long axis. Unlike the nanowires previously studied in Chapter 4 (in the size range $d < 80$ nm[1]), these larger nanowires with diameters

d~150 nm demonstrate markedly different cavity mode spectra characterized by higher order modes with electric field polarizations both perpendicular to the long axis (TE or transverse electric) and parallel to the long axis (TM or transverse magnetic) of the nanowire (Figure 5.4a). Note this convention is orthogonal to that used in some plasmonics literature where the field polarization is labeled with respect to the plane of incidence,[28] but inline with recent nanowire literature where the field polarization is referenced with respect to the nanowire long-axis.[29] For more details of this naming convention we refer the reader to Chapter 3, section 3.5.1.1. Figure 5.4 shows the photoluminescence spectrum of the plasmonically-coupled silicon nanowire examined in Figure 5.2, along with the associated cavity field spectrum (Figure 5.4b). Note there is a region of low mode activity between peak 1 at 2.58 eV and peak 2 at 2.22 eV of the simulated cavity spectrum. This is responsible for the lower photoluminescence counts in this spectral range. This region of low mode activity is observed all across the measured size range in this work and is due to a lack of high order TE polarized modes and lower order TM modes with both azimuthal and radial components.

As can be observed from the frequency domain electric field profiles (Figures 5.4c-f), these modes resemble whispering gallery modes (WGM) and will be classified as either TE_{mn} for perpendicular electric field polarization or TM_{mn} for parallel electric field polarization (with respect to the nanowire long-axis) and where the indices m and n correspond to the integer number of half wavelengths in the azimuthal and radial directions respectively. It should be noted that for WGM modes, the index "m" often refers to an integer number of wavelengths as circularly symmetric structures must

observe the periodic boundary condition, which only allows modes at full wavelength multiples.[30] The base at the intersection of the nanowire and substrate breaks the circular symmetry and enables modes at half-wavelength multiples.[1] Following the spectra from right to left (i.e. from low energy to high energy laser excitation in Figure 5.4b), we observe 3 modes with perpendicular electric field polarization, which are attributed to the TE_{71}, TE_{81}, and TE_{91} modes respectively. These are plasmonic modes similar to those in chapter 4, but of higher order, and where the majority of the field is stored near the Si/SiO_x interface also.[1] The mode at ~2.6 eV (Figure 5.4c), on the other hand, is polarized parallel to the nanowire long-axis and has a completely different field profile, where the majority of the field is stored inside the Si core as opposed to the metal interface. This may be classified as the TM_{11} mode. Referring to Figures 5.4c-f, we note that the field intensities (normalized to the source) within the core in both the TM and TE modes are $>10^2$. The TE modes demonstrate >1000 times intensity at the silicon surface, but this is offset by the superior spatial overlap between the active region and the cavity mode in the TM_{11} mode. It has been previously demonstrated that in silicon-Au plasmonic core-shell nanowire photodetectors, both the TE and TM modes may contribute in similar magnitudes to the spectral characteristics of the system,[31] thus given the relative field intensities within the silicon core, we expect that both TE and TM modes can mediate the hot-PL process.

The question remains, as to why is there a spectral gap in emission between the TE and TM modes in the spectrum (Figure 5.4b). This may be understood from the inverse relationship between azimuthal mode order and quality factor that exists in

plasmonic cavities. In all-dielectric WGM resonators, the quality factor scales proportional to the azimuthal order (and inversely proportional to the radial order),[32,33] in other words this is why larger resonators, which host very high order modes, demonstrate the highest quality factors.[34] The opposite trend is true in plasmonic systems; the quality factor decreases with increasing azimuthal mode order[35]. In a surface-plasmon WGM-type resonator, increasing mode order within the same circumference implies increased confinement to the metal-dielectric interface. Metals are lossy media,[28,36-38] thus higher interaction with the metal-interface results in increased damping of the cavity mode. By tracking quality factor of the TE cavity modes as a function of azimuthal order (Figure 5.4g) we observe that the quality factor drops precipitously with increasing order, which signifies that in our system mode damping becomes prohibitively high for azimuthal mode orders >9. Therefore, due to the highly damped high order TE modes we expect a decreased photoluminescence emission intensity in regions at energies higher than the highest order TE mode, but lower than the lowest order TM mode.

This characteristic of the cavity modes is reflected in the emission spectra of several nanowires, which demonstrate a drop in emission intensity between bands A and B, and which was not observed in previous measurements of smaller (sub 80 nm) plasmonically-coupled nanowires.[1] For 2.708 eV excitation, we observe two broad regions of the emission envelope, one centered around 2.5 eV due to the TM mode and the other centered around 2.2 eV due to the TE modes. Interestingly, in the spectra excited at 2.708 eV, band B is effectively quenched (Figure 5.2b and 5.4b, black curves), as it is resonant with this area of low mode activity. Furthermore, the spectra due to

excitation at 2.541 eV, where band A (at ~0.2 eV shift, Figure 5.2b) is now resonant with the region of low mode activity, also exhibits low intensity in this region when compared with the spectra excited at other laser energies. In fact, the features of the photoluminescence spectra due to excitation at other laser energies in the range 2.541 eV - 1.959 eV are all superimposed on the same emission envelope due to the TE cavity modes, but again, restricted in the low energy region due the silicon bandgap at the L-point (discussed above). Therefore, for larger sized Si nanowires (d~150 nm range) we now exploit both TE and TM modes to generate hot-luminescence in larger nanowire cavities.

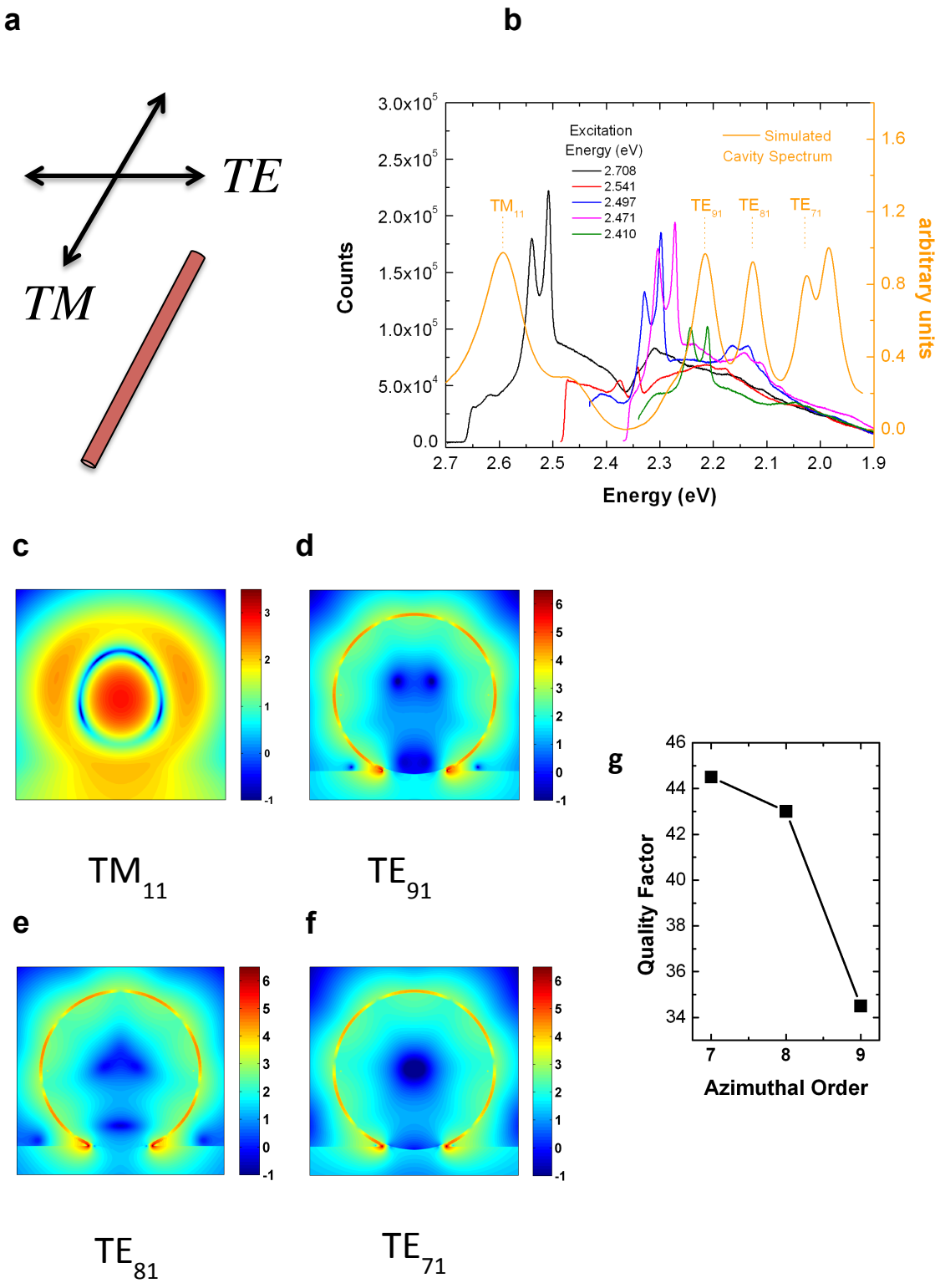
a
b
TE
TM
Counts
Energy (eV)
arbitrary units
Excitation Energy (eV)
2.708
2.541
2.497
2.471
2.410
Simulated Cavity Spectrum
TM11
TE91
TE81
TE71
c
d
e
f
g
TM11
TE91
TE81
TE71
Quality Factor
Azimuthal Order

Figure 5.4 | Electromagnetic mode properties of plasmonically-coupled silicon analyzed via FDTD simulations and photoluminescence spectroscopy. a) nomenclature convention for modes polarized parallel (TM) and perpendicular (TE) to the nanowire long-axis. b) Variable-energy excitation photoluminescence spectra of *d*=150 nm Ω-cavity silicon nanowire juxtaposed with simulated cavity mode spectrum (orange curve). c-f) frequency domain profiles of the electric intensity (log scale) for cavity modes ordered from highest to lowest energy. g) Plot of quality factor versus azimuthal index (m), for TE modes in (b) and represented by the field profiles in (d-f).[17]

5.4.2: Size Dependent Photoluminescence Spectroscopy of Plasmonically-Coupled Si

The size dependence (albeit a narrow range of 151 nm to 156 nm) of the emission is shown in figure 5.5. Photoluminescence spectra are analyzed for nanowires with sizes *d*=151 nm, 153 nm, and 156 nm, corresponding to Figures 5.5a-c respectively and excited at different laser energies. For *d*=151 nm, the emission spectrum excited with the 2.708 eV laser line (Figure 5.5a, black curve) demonstrates a dip in the emission around 2.38 eV (as in the *d*=150 nm sample examined above), which we attribute to cavity mode structure (Figure 5.5a, top). When the sample is excited with a 2.541 eV (488 nm) laser (Figure 5.5a, red curve) band A becomes resonant with the local minimum in the cavity field spectrum resulting in significant damping of the emission in this region. Indeed, the entire emission envelope resulting from the excitation energy of 2.541 eV and those at other laser energies up to 1.959 eV also reflects the same structure observed at 2.708 eV excitation. Figure 5.5e shows simulated cavity spectra for various nanowire diameters, which demonstrate a monotonic red-shift in the cavity modes with increasing diameter (as expected). As the nanowire size (although in a small range) increases (Figure 5.5b, c), the cavity modes redshift (Figure 5.5e) and the emission envelope shifts to the right

(lower energies) leading to a direct modulation of subpeaks in band A (Figure 5.5b, red curve). The overall red shift of the emission also results in luminescence from lower energy states. Figure 5.5d is a magnified view of the low energy region of the spectrum (1.5 eV-1.9 eV), excited at 1.959 eV for all three nanowires. As the intensity of band A significantly decreases under excitation at 1.959 eV, the plasmonic nanowire with *d*=153 nm shows a different peak spacing of ~15 meV, compared to that of ~30 meV at the other excitation energies, which differs by 1 TA phonon energy. This strongly suggests that, since the excitation energy is smaller than the energy gap at L-point (~2.1 eV), the electronic states along the <111> direction cannot contribute to the hot luminescence process, leading to a dramatic decrease in the counts and also different peak positions. Furthermore, as expected from figure 5.5e, increasing nanowire size leads to an increase in measured counts from low energy states due to the increased overlap between the cavity mode and the band A for the larger size nanowires.

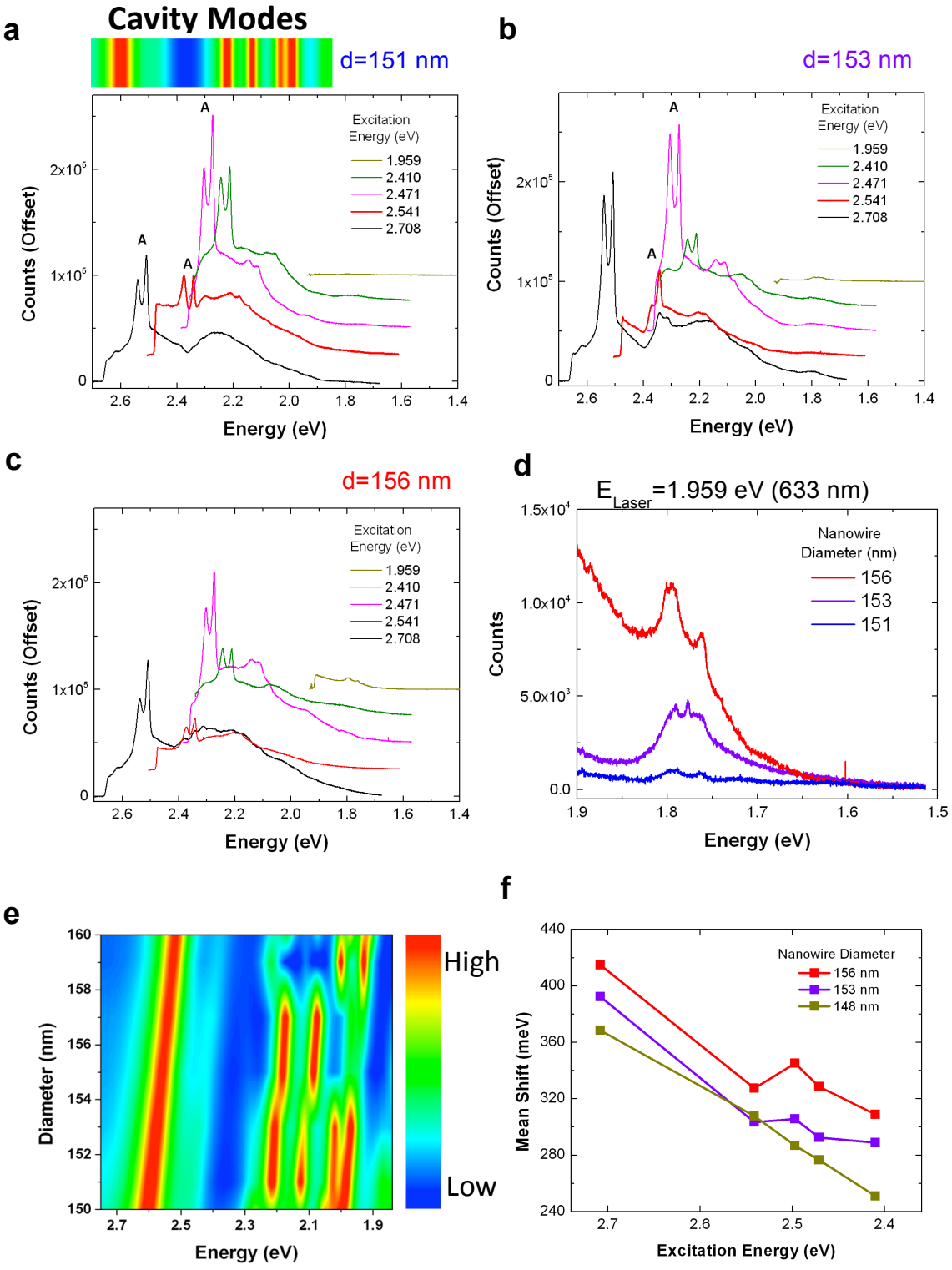
a
Cavity Modes
d=151 nm
Counts (Offset)
Energy (eV)
Excitation Energy (eV)
1.959
2.410
2.471
2.541
2.708
A
b
d=153 nm
c
d=156 nm
d
E_Laser=1.959 eV (633 nm)
Counts
Nanowire Diameter (nm)
156
153
151
e
Diameter (nm)
High
Low
f
Mean Shift (meV)
Excitation Energy (eV)
Nanowire Diameter
156 nm
153 nm
148 nm

Figure 5.5 | a-c) Photoluminescence spectra of plasmonically-coupled nanowires excited at various laser energies in the range 1.959 eV – 2.708 eV for nanowires of size a) d=151 nm, b) d=153 nm, and c) d=156 nm (all spectra are offset by 25,000 counts for clarity). The cavity mode spectrum of the *d*=151 nm nanowire is plotted on top of the photoluminescence spectra (high in red to low in blue) using the same energy scale. The variable energy excitation photoluminescence spectra demonstrate the role of mode structure in modulating high intensity subpeaks. In addition to size-dependent peak modulation, the modes, which red-shift with increasing size, also enable hot luminescence at lower energies for larger nanowires. d) Photoluminescence spectrum in low energy region (excited with 633 nm, He-Ne laser) for samples (a-c). e) Simulated cavity mode spectra of plasmonically-coupled silicon nanowires with diameters in the range *d*=150 nm to 160 nm as a function of energy.[17]

5.5: Differentiating Hot Photoluminescence from Resonant Raman Scattering

5.5.1: Temperature Dependent Spectroscopy of Plasmonically-Coupled Si

To further test the validity of the hot-luminescence process, we examined the temperature dependence of the photoluminescence spectrum from plasmonically-coupled silicon and compared it to the known temperature dependence of other radiative and scattering processes. Raman spectroscopy typically shows a decrease in intensity with increasing temperature due to a decrease in the polarizability of a material with temperature.[39] Resonant Raman Spectroscopy of silicon also demonstrates a negative temperature dependence with increasing temperature (as the number of photons involved in electronic absorption increases with temperature, due to phonon mediated indirect absorption, thereby limiting the amount of photons involved in the Raman process).[40,41] Likewise, photoluminescence from direct-bandgap materials, such as GaAs[42] and CdS[43] also exhibit a negative temperature dependence due to increased non-radiative recombination at higher temperatures[18]. On the other hand, indirect transitions such as hot

luminescence from an indirect-bandgap material (such as silicon) involve a competition between an increase in the non-radiative decay rate and also an increase in the radiative decay rate with temperature, as phonons are critical to mediating radiative recombination (see Chapter 4, sections 4.1.2 and Chapter 5, section 5.3). Previously, a positive temperature dependence was verified for silicon quantum dots, where increased photoluminescence was observed at higher temperatures and attributed to indirect-radiative recombination, as also confirmed by time resolved photoluminescence measurements.[44]

For these plasmonically-coupled silicon samples, we measured the photoluminescence spectrum at temperatures in the range 77 K-300 K at 2.708 eV excitation and with a fixed laser power. A monotonic increase in counts as a function of increasing temperature (Figures 5.6) was observed, again, in contrast to the stokes-Raman spectra, which generally shows a decrease in intensity with increasing temperature. We chose two representative data sets (Figure 5.6 a, b), which exhibit spectra with differing levels of intensity and broad spectral features, while both exhibit a positive temperature dependence in their photoluminescence counts. We observed this positive temperature dependence in all samples measured. It should be noted that at higher temperatures the absorption coefficient of silicon will also increase (as it is phonon mediated), which can lead to a larger concentration of excited carriers and emitted light.[45] However, the ratio of absorption coefficients for silicon (2.708 eV) at 300 K and 77 K is 2.4, while the observed ratio of integrated counts (emission) at the same temperatures ranges from 10-20 depending on the nanowire size and laser excitation energy. Therefore, the

temperature dependent change in absorption is insufficient to explain an order of magnitude increase in the measured increase in counts. Thus, the temperature dependence of the emission intensity can be best explained by a hot-photoluminescence process, where the thermal activation of phonons that are required for intra- and inter-band relaxation can increase the radiative quantum yield.

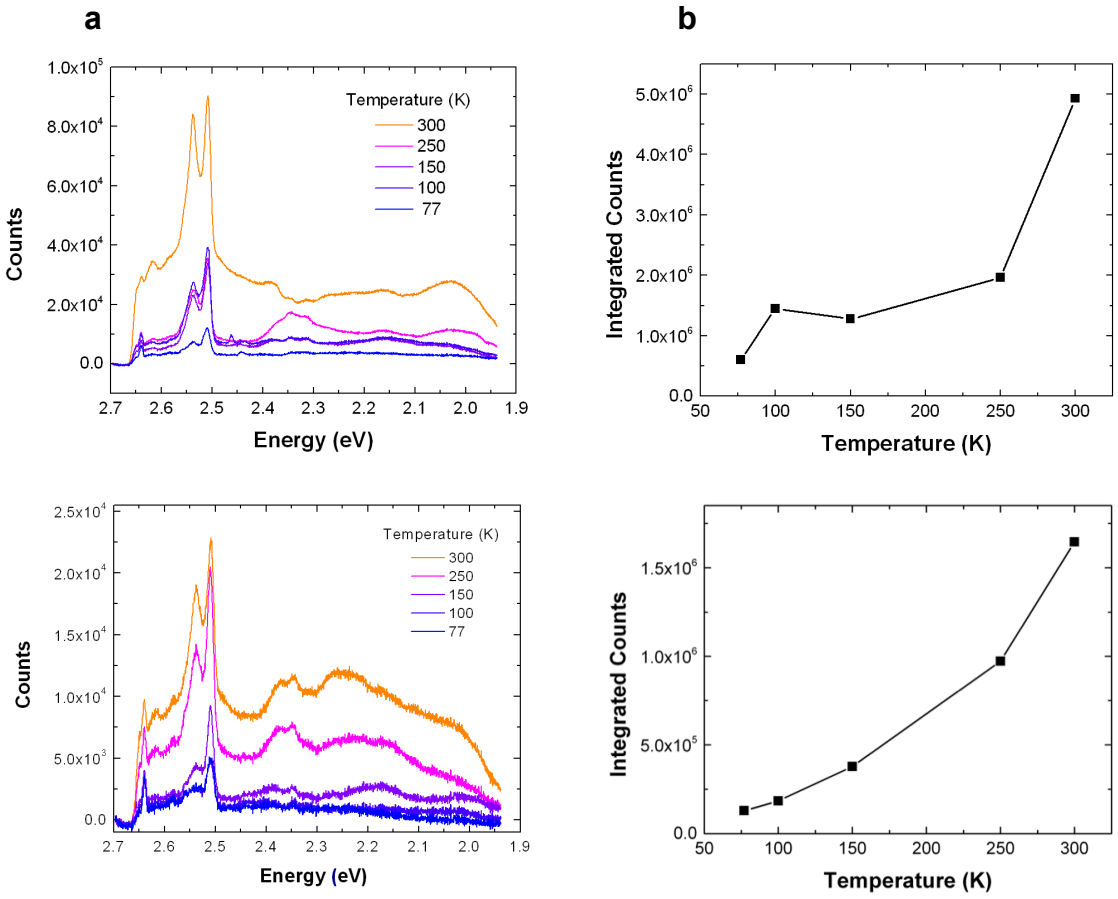

Figure 5.6 | a) Temperature dependent photoluminescence spectra of plasmonically-coupled silicon (for two different samples) in the range 77 K-300 K. Increase in overall emission intensity with temperature follows expected trend for hot-luminescence from an indirect bandgap material as the phonon population increases with increasing temperature. b) Plot of total integrated counts as a function of temperature for samples shown in (a).[17]

5.5.2: Quantification of Mean Emission Energy

As demonstrated in section 5.3, there is considerable scatter in the positions of individual peaks in the broad spectrum of plasmonically-coupled silicon, which changes as a function of both size and excitation energy (see discussion in section 5.3 and Figure 5.3). The observed modulation of individual peaks and spectral features as a function of excitation energy is in contrast to the resonant Raman spectrum of silicon, which demonstrates little or no variation in its spectral features as a function of excitation energy in either the visible[46] or infrared frequencies.[4] To further explore the variation of the many spectral features of plasmonically-coupled silicon as a function of excitation energy, we use the photoluminescence spectra to extract the mean emission energy of the spectrum and thus the mean energy shift of the spectrum from the exciting laser energy. The mean emission energy was calculated from the photoluminescence spectra via $\bar{\nu} = \frac{\int \nu N(\nu) d\nu}{\int N(\nu) d\nu}$ where $N(\nu)$ is the number of measured counts at a frequency ν.[47] The mean emission energy is then $h\bar{\nu}$.[48] Subtracting this value from the exciting laser energy results in a mean emission shift. Plotting the mean emission shift (of the spectrum) as a function of excitation energy (Figure 5.7), we observe significant variation in the mean emission energy of individual nanowire samples (>100 meV comparing 2.410 eV excitation with 2.708 eV excitation and > 25 meV between 2.410 eV and 2.541 eV), which is a consequence of the dependence of the emission on both cavity modes and electronic structure as discussed above. Moreover, there is clear size dependence in the mean emission shift where larger wires demonstrate greater mean emission shifts and thus,

stronger red shifting in the emission envelope. The red-shift of the emission envelope as a function of size is consistent with the previous discussion on size-dependent cavity modes (see section 5.4.2 and figure 5.5e), where lower energy modes (for larger nanowires) enhance scattering from lower energy states. We also note that carbon contamination, and thus Raman activity of carbon, can be an issue especially when combined with silver;[49] although it is unlikely that trace amounts of carbon can yield such bright white light emission (~10^5 peak counts, >10^6 integrated counts), that the broad emission envelope is very strongly dependent on the excitation energy, and that the peaks change their positions and intensities depending on a variety of parameters. These observations are in contrast to the Raman spectrum of silicon where the mean emission energy should show negligible dependence on the exciting laser in this range. It should be noted that Surface Enhanced Raman Spectroscopy (SERS) is known to lead to a broad background, which can depend on plasmon modes.[50] Still, measurements in the range 2.410 eV-2.541 eV include all TE plasmon modes (see Figure 5.4b) thus; we expect any possible SERS background to result in little or no net variation of the average emission energy or shift. Furthermore, SERS spectra retain the same Raman spectral features over a broad excitation range,[51] where the SERS enhancement is much more sensitive to resonance with electronic states than local field enhancement.[52]

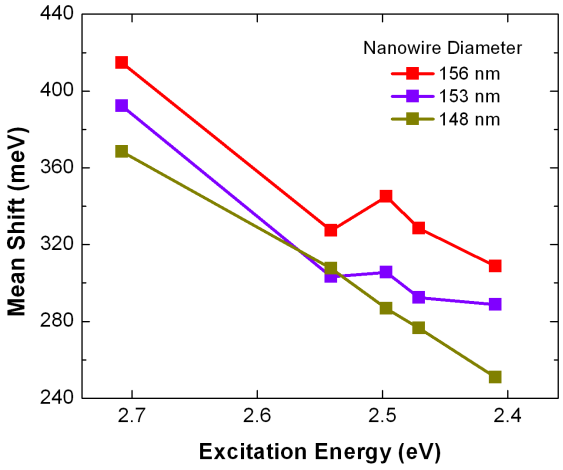

Figure 5.7 | Difference between the average emission energy and exciting laser energy (i.e. the mean emission shift) plotted against excitation energy. The large variation in mean emission energy as function of size and excitation energy highlight the role of both cavity modes and electronic structure in modulating the emission spectrum.[17]

5.6: Conclusions

In this chapter we demonstrated bright luminescence from silicon nanowires coupled with metal nanocavities supported by high order hybrid cavity-surface plasmon modes. Photoluminescence spectroscopy at variable excitation energies reveals that the electronic structure of silicon plays a key role in determining the emission intensity, while the individual sub-features of the spectrum are mediated by phonons in a hot-luminescence process. Finite difference time domain simulations elucidate the role of cavity modes in modulating the emission spectrum. Furthermore, temperature dependent spectroscopy reveals a temperature dependence of the measured intensity that is indicative of hot-luminescence and rules out the Resonant Raman process. It should also be noted that, in addition to this experimental work, extensive theoretical work is

necessary to analyze this highly complicated system featuring the interplay between phonons (bulk and interfacial for this hybrid system), plasmons, and charge carriers all of which play a role in the radiative recombination process. Finally, a direct measurement of the carrier lifetimes in plasmonically-coupled silicon would be highly desirable.

References

1 Cho, C.-H., Aspetti, C. O., Park, J. & Agarwal, R. Silicon coupled with plasmon nanocavities generates bright visible hot luminescence. *Nat Photon* **7**, 285-289 (2013).

2 Cho, C.-H., Aspetti, C. O., *et al.* Tailoring hot-exciton emission and lifetimes in semiconducting nanowires via whispering-gallery nanocavity plasmons. *Nat Mater* **10**, 669-675 (2011).

3 Permogorov, S. Hot Excitons in Semiconductors. *Phys Status Solidi B* **68**, 9-42, doi:Doi 10.1002/Pssb.2220680102 (1975).

4 Liang, D. & Bowers, J. E. Recent progress in lasers on silicon. *Nature Photonics* **4**, 511-517, doi:Doi 10.1038/Nphoton.2010.167 (2010).

5 Pavesi, L., Lockwood, D. J. & Alumni and Friends Memorial Book Fund. *Silicon photonics*. (Springer, 2004).

6 Cullis, A. G. & Canham, L. T. Visible-Light Emission Due to Quantum Size Effects in Highly Porous Crystalline Silicon. *Nature* **353**, 335-338, doi:Doi 10.1038/353335a0 (1991).

7 Wilson, W. L., Szajowski, P. F. & Brus, L. E. Quantum Confinement in Size-Selected, Surface-Oxidized Silicon Nanocrystals. *Science* **262**, 1242-1244, doi:Doi 10.1126/Science.262.5137.1242 (1993).

8 Hirschman, K. D., Tsybeskov, L., Duttagupta, S. P. & Fauchet, P. M. Silicon-based visible light-emitting devices integrated into microelectronic circuits. *Nature* **384**, 338-341, doi:Doi 10.1038/384338a0 (1996).

9 Walters, R. J., Bourianoff, G. I. & Atwater, H. A. Field-effect electroluminescence in silicon nanocrystals. *Nat Mater* **4**, 143-146, doi:Doi 10.1038/Nmat1307 (2005).

10 Park, N. M., Kim, T. S. & Park, S. J. Band gap engineering of amorphous silicon quantum dots for light-emitting diodes. *Applied Physics Letters* **78**, 2575-2577, doi:Doi 10.1063/1.1367277 (2001).

11 Trupke, T., Zhao, J. H., Wang, A. H., Corkish, R. & Green, M. A. Very efficient light emission from bulk crystalline silicon. *Appl Phys Lett* **82**, 2996-2998, doi:Doi 10.1063/1.1572473 (2003).

12 Wurfel, P. The Chemical-Potential of Radiation. *J Phys C Solid State* **15**, 3967-3985, doi:Doi 10.1088/0022-3719/15/18/012 (1982).

13 Green, M. A., Zhao, J. H., Wang, A. H., Reece, P. J. & Gal, M. Efficient silicon light-emitting diodes. *Nature* **412**, 805-808, doi:Doi 10.1038/35090539 (2001).

14 Wiesner, P. & Heim, U. Dynamics of Exciton-Polariton Recombination in Cds. *Physical Review B* **11**, 3071-3077, doi:Doi 10.1103/Physrevb.11.3071 (1975).

15 Matsusue, T. & Sakaki, H. Radiative Recombination Coefficient of Free-Carriers in Gaas-Aigaas Quantum-Wells and Its Dependence on Temperature. *Appl Phys Lett* **50**, 1429-1431, doi:Doi 10.1063/1.97844 (1987).

16 Anger, P., Bharadwaj, P. & Novotny, L. Enhancement and Quenching of Single-Molecule Fluorescence. *Physical Review Letters* **96**, 113002 (2006).

17 Aspetti, C. O., Cho, C.-H., Agarwal, R. & Agarwal, R. Studies of hot photoluminescence in plasmonically-coupled silicon via variable energy excitation and temperature dependent spectroscopy. *Nano Letters* **14**, 5413-5422 (2014).
18 Pankove, J. I. *Optical processes in semiconductors*. (Prentice-Hall, 1971).
19 Goldman, J. R. & Prybyla, J. A. Ultrafast Dynamics of Laser-Excited Electron Distributions in Silicon. *Physical Review Letters* **72**, 1364-1367, doi:Doi 10.1103/Physrevlett.72.1364 (1994).
20 Sabbah, A. J. & Riffe, D. M. Femtosecond pump-probe reflectivity study of silicon carrier dynamics. *Physical Review B* **66**, doi:Doi 10.1103/Physrevb.66.165217 (2002).
21 Prokofiev, A. A. *et al.* Direct Bandgap Optical Transitions in Si Nanocrystals. *Jetp Lett*+ **90**, 758-762, doi:Doi 10.1134/S0021364009240059 (2009).
22 Chelikowsky, J. R. & Cohen, M. L. Electronic-Structure of Silicon. *Physical Review B* **10**, 5095-5107, doi:Doi 10.1103/Physrevb.10.5095 (1974).
23 Hess, K. & Vogl, P. Remote Polar Phonon-Scattering in Silicon Inversion Layers. *Solid State Commun* **30**, 807-809 (1979).
24 Lu, J. Q. & Koch, F. Polar phonon scattering at the Si-SiO(2) interface. *Microelectron Eng* **48**, 95-99, doi:Doi 10.1016/S0167-9317(99)00346-9 (1999).
25 Yan, Y. X., Gamble, E. B. & Nelson, K. A. Impulsive Stimulated Scattering - General Importance in Femtosecond Laser-Pulse Interactions with Matter, and Spectroscopic Applications. *J Chem Phys* **83**, 5391-5399, doi:Doi 10.1063/1.449708 (1985).
26 Wei, S. Q. & Chou, M. Y. Phonon Dispersions of Silicon and Germanium from 1st-Principles Calculations. *Physical Review B* **50**, 2221-2226, doi:Doi 10.1103/Physrevb.50.2221 (1994).
27 Itoh, T. *et al.* Excitation laser energy dependence of surface-enhanced fluorescence showing plasmon-induced ultrafast electronic dynamics in dye molecules. *Physical Review B* **87**, doi:Doi 10.1103/Physrevb.87.235408 (2013).
28 Maier, S. A. *Plasmonics: Fundamentals and Applications*. (Springer, 2007).
29 Cao, L. Y. *et al.* Engineering light absorption in semiconductor nanowire devices. *Nat Mater* **8**, 643-647, doi:Doi 10.1038/Nmat2477 (2009).
30 Nobis, T., Kaidashev, E. M., Rahm, A., Lorenz, M. & Grundmann, M. Whispering gallery modes in nanosized dielectric resonators with hexagonal cross section. *Physical Review Letters* **93**, doi:Doi 10.1103/Physrevlett.93.103903 (2004).
31 Fan, P. Y. *et al.* An invisible metal-semiconductor photodetector. *Nat Photonics* **6**, 380-385, doi:Doi 10.1038/Nphoton.2012.108 (2012).
32 Oraevsky, A. N. Whispering-gallery waves. *Quantum Electron*+ **32**, 377-400, doi:Doi 10.1070/Qe2002v032n05abeh002205 (2002).
33 Matsko, A. B. & Ilchenko, V. S. Optical resonators with whispering-gallery modes - Part I: Basics. *Ieee J Sel Top Quant* **12**, 3-14, doi:Doi 10.1109/Jstqe.2005.862952 (2006).

34 Vernooy, D. W., Ilchenko, V. S., Mabuchi, H., Streed, E. W. & Kimble, H. J. High-Q measurements of fused-silica microspheres in the near infrared. *Opt Lett* **23**, 247-249, doi:Doi 10.1364/Ol.23.000247 (1998).
35 Min, B. K. *et al.* High-Q surface-plasmon-polariton whispering-gallery microcavity. *Nature* **457**, 455-U453, doi:Doi 10.1038/Nature07627 (2009).
36 Oulton, R. F., Sorger, V. J., Genov, D. A., Pile, D. F. P. & Zhang, X. A hybrid plasmonic waveguide for subwavelength confinement and long-range propagation. *Nat Photon* **2**, 496-500 (2008).
37 Khurgin, J. B. & Sun, G. Practicality of compensating the loss in the plasmonic waveguides using semiconductor gain medium. *Applied Physics Letters* **100**, doi:Doi 10.1063/1.3673849 (2012).
38 Oulton, R. F. Loss and gain. *Nature Photonics* **6**, 219-221, doi:Doi 10.1038/Nphoton.2012.72 (2012).
39 Venkateswarlu, K. Temperature Dependence of the Intensities of Raman Lines. *Nature* **159**, 96-97, doi:Doi 10.1038/159096b0 (1947).
40 Compaan, A. & Trodahl, H. J. Resonance Raman-Scattering in Si at Elevated-Temperatures. *Physical Review B* **29**, 793-801, doi:Doi 10.1103/Physrevb.29.793 (1984).
41 Compaan, A., Lee, M. C. & Trott, G. J. Phonon Populations by Nanosecond-Pulsed Raman-Scattering in Si. *Physical Review B* **32**, 6731-6741, doi:Doi 10.1103/Physrevb.32.6731 (1985).
42 Jiang, D. S., Jung, H. & Ploog, K. Temperature-Dependence of Photoluminescence from Gaas Single and Multiple Quantum-Well Heterostructures Grown by Molecular-Beam Epitaxy. *Journal of Applied Physics* **64**, 1371-1377, doi:Doi 10.1063/1.341862 (1988).
43 Hoang, T. B. *et al.* Temperature dependent photoluminescence of single CdS nanowires. *Applied Physics Letters* **89**, doi:Doi 10.1063/1.2357003 (2006).
44 Kwack, H. S., Sun, Y., Cho, Y. H., Park, N. M. & Park, S. J. Anomalous temperature dependence of optical emission in visible-light-emitting amorphous silicon quantum dots. *Applied Physics Letters* **83**, 2901-2903, doi:Doi 10.1063/1.1613993 (2003).
45 Weakliem, H. A. & Redfield, D. Temperature-Dependence of the Optical-Properties of Silicon. *J Appl Phys* **50**, 1491-1493, doi:Doi 10.1063/1.326135 (1979).
46 Piscanec, S. *et al.* Raman spectrum of silicon nanowires. *Mat Sci Eng C-Bio S* **23**, 931-934, doi:Doi 10.1016/J.Msec.2003.09.084 (2003).
47 Epstein, R. I. & Sheik-Bahae, M. *Optical refrigeration : science and applications of laser cooling of solids*. (Wiley-VCH, 2009).
48 Zhang, J., Li, D. H., Chen, R. J. & Xiong, Q. H. Laser cooling of a semiconductor by 40 kelvin. *Nature* **493**, 504-508, doi:Doi 10.1038/Nature11721 (2013).
49 Otto, A. Raman-Spectra of (Cn)- Adsorbed at a Silver Surface. *Surf Sci* **75**, L392-L396, doi:Doi 10.1016/0039-6028(78)90263-7 (1978).

50 Mahajan, S. *et al.* Understanding the Surface-Enhanced Raman Spectroscopy "Background". *J Phys Chem C* **114**, 7242-7250, doi:Doi 10.1021/Jp907197b (2010).
51 Jung, Y. M., Sato, H., Ikeda, T., Tashiro, H. & Ozaki, Y. Excitation wavelength dependent surface-enhanced Raman spectra of a dipping film of azobenzene-containing long-chain fatty acid on a silver mirror. *Spectrochim Acta A* **60**, 1941-1945, doi:Doi 10.1016/J.Saa.2003.10.010 (2004).
52 Yoon, I. *et al.* Single Nanowire on a Film as an Efficient SERS-Active Platform. *J Am Chem Soc* **131**, 758-762, doi:Doi 10.1021/Ja807455s (2009).

Chapter 6. Surface Plasmon Enhanced Laser Cooling of Semiconductors

6.1: Introduction

6.1.1: Motivation

Cooling of matter with lasers presents the possibility of a highly efficient cooling mechanism that would require no moving parts or cryogenic fluids,[1] but would rather rely strictly on the optical properties of matter. Laser cooling of matter may be broadly categorized into cooling of atomic systems, rare-earth ion-doped glasses, and semiconductors, which is the focus of this chapter. Laser cooling of atoms differs from laser cooling of solid state materials in that it is largely based on momentum transfer mediated by both incoming photons and spontaneously emitted photons, which slows the atom down.[2] As a testament to the impact of this field, two Nobel prizes in optical cooling were awarded, first in 1997 for the achievement of nanoKelvin temperatures[3] and optical trapping[4] (leading to the development of the most accurate atomic clocks ever created[5]) and in 2001 for the realization of a Bose-Einstein condensate in a system of ultra-cold atoms.[6]

Optical cooling in the solid state was predicted as far back as 1929 by Pringsheim et al.[7], and is based on the production of up-converted luminescence, where light is emitted at higher energy than the initial exciting laser via coupling to vibrational modes of the host material. In analogy to anti-Stokes Raman scattering, this upconverted

luminescence is often quoted as “anti-Stokes luminescence”. Optical cooling in the solid state has witnessed success in the cooling of rare-earth (RE) doped glasses such as fluorozirconate, ZBLANP: $Yb^{3+}$where Yb^{3+} is the RE dopant.[8] Glasses generally have a large bandgap due to their disordered structure, thus dopants are required to enable absorption at useful frequencies. Furthermore, fluoride crystals and glasses generally have low phonon energies, which limits non-radiative processes that are adverse to anti-Stokes luminescence (see section 6.1.2 on SBE theory). In RE doped glasses, anti-Stokes luminescence is achieved by exciting electrons of the ground state into a low energy excited state that is closely separated from a higher energy excited state (Figure 6.1, red curve). This is illustrated for a 4-level model system in Figure 6.1, where the electron is resonantly excited from the top of the ground state manifold to the lowest energy excited state. Both the ground and excited state manifolds will thermalize at the rates of w_1 and w_2 respectively, which includes a component at the lower energy ground state and higher energy excited states due to Boltzmann statistics. Note the distribution of excited electrons within discrete donor atoms may be approximated by classical (Boltzmann) statistics as they may be treated as distinguishable particles. More specifically, this is due to the low electron concentration, which leads to an electron-electron separation that is greater than the de Broglie wavelength of the electron.[9] For detailed description of the excitation and decay process the reader is referred to the review by Epstein and Bahae.[10] A key issue in the cooling of RE-doped solids is the width of the ground state manifold, i.e. the separation between states $|0\rangle$ and $|1\rangle$ in 6.1. As the temperature of the system lowers so will the population of the highest energy ground state which will in continually

limit the absorption of the material at a fixed excitation laser energy. As we will see in the following section, this places a limit on the cooling achievable in in RE-doped solids to ~T=100 K.

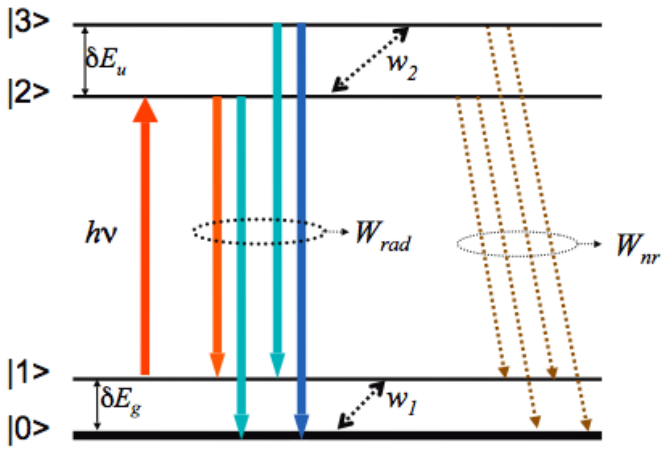

Figure 6.1 | Model of optical refrigeration for a 4-level system. $|0\rangle$ and $|1\rangle$ comprise the electronic states of the ground state manifold separated by energy δE_g. $|2\rangle$ and $|3\rangle$ comprise the excited state manifold separated by energy δE_u. W_{rad} and W_{nr} are the radiative and non-radiative decay rates respectively, while w_1 and w_2 correspond to the phonon-mediated thermalization rate of the ground state and excited state manifolds respectively.[10] [Adapted from reference 10]

Charge carriers in semiconductor materials on the other hand, reside in electronic bands and feature large electron concentrations. As such, they obey Fermi-Dirac statistics and do not suffer the same limitations as RE-doped glasses. In theory, semiconductor materials may be cooled to much lower temperatures of ~T=10 K,[11] yet unambiguous cooling of a semiconductor was not achieved until 2013, when Xiong et al. cooled nanobelts composed of Cadmium Sulfide by up to 40 K.[12] As we can intuit, optical cooling of semiconductor materials will have the largest impact on technological

development as these form the backbone of modern electronic and optical devices. In the next section, we will explore the prevailing theory behind optical cooling of solids and determine the difficulties and advantages of cooling with semiconductor materials.

6.1.2: Sheik-Bahae Epstein (SBE) Theory of Solid State Cooling

Under the right excitation conditions, when a sample is illuminated with laser light a portion of that power will go into cooling the sample. The ratio of cooling power to incident power can thus be considered the cooling efficiency, which would need to be > 0 in order to achieve any cooling. According to the Sheik-Bahae Epstein (SBE) theory of cooling of solids the cooling efficiency, η_C, may be expressed as:

$$\eta_C(\nu_L, T) = \eta_{exe}\eta_{abs}\frac{\langle \nu_{em} \rangle}{\nu_L} - 1 \qquad \text{Eq. 6.1}$$

where ν_L and T are the excitation laser frequency and sample temperature respectively. ν_{em}, η_{exe} and η_{abs} are the mean emission frequency, external quantum efficiency and absorption efficiency respectively. Thus, in order to achieve high cooling efficiencies we require materials that have external quantum and absorption efficiencies that are close to unity and which are excited at energies as far away from the emission energy as possible. We address each of these components individually below.

The external quantum yield is closely related to the internal quantum yield (QY) that measures the efficiency of radiative recombination within a material and which has been a focus of the previous chapters, namely:

$$QY = \frac{\gamma_r}{\gamma_r + \gamma_{nr}} \quad \text{Eq. 6.2}$$

where γ_r and γ_{nr} are the radiative and non-radiative decay rates respectively. Subsequently, the external quantum efficiency may be computed as:

$$\eta_{exe} = \frac{\eta_e \gamma_r}{\eta_e \gamma_r + \gamma_{nr}} \quad \text{Eq. 6.3}$$

where η_e is the extraction efficiency. The extraction efficiency is a measure of the ability of light to escape its immediate surroundings. Direct bandgap semiconductor materials such as GaAs or ZnO, are a natural choice due to their high quantum yields.[13] The extraction efficiency, on the other hand, is a detriment. As expounded in Chapter 1, semiconductor nanowires, which generally feature high refractive indices, are excellent optical cavities. In other words, they generally trap light potentially lowering the external quantum yield.

Non-radiative recombination is also an issue, which becomes explicit if we recast the external quantum efficiency in terms of the carrier density, *N*, via:

$$\eta_{exe} = \frac{\eta_e B N^2}{AN + \eta_e B N^2 + CN^3} \quad \text{Eq. 6.4}$$

where A, B, and C correspond to the coefficients for the non-radiative rate (AN), radiative rate (BN^2), and Auger processes (CN^3) respectively.[14] Optimizing the above expression for the carrier concentration, we obtain the following expression in terms of the A, B and C coefficients only:

$$\eta_{exe}(N_{optimal}) = 1 - 2\frac{\sqrt{AC}}{\eta_e B} \qquad \text{Eq. 6.5}$$

Though the C coefficient is mostly fixed, the A coefficient has a geometric dependence. Non-radiative recombination may occur in defect and trap states within the bulk as well as the material surface. As we know, the smaller the dimensions of the material, the higher the importance of the surface due to the ratio of surface to volume, which increases with decreasing dimensions. Furthermore, if the material is single crystalline, as is often the case with VLS grown nanostructures (see chapter 2), then non-radiative recombination should occur at the surface only. This property may be readily observed in the photoluminescence spectrum of the sample, which will only feature bulk free-exciton emission or emission from the band-edge if it is single crystalline.[15]

The non-radiative recombination at the surface, A_s, is related to sample dimensions via:

$$A_s = \frac{S}{t} \qquad \text{Eq. 6.6}$$

where S is the surface recombination velocity and t is the sample thickness (assuming a semi-infinite slab geometry).[15,16] Thus, the external quantum efficiency may be

significantly improved by using nanostructures with superior surface quality, a factor we will revisit in further sections. The absorption efficiency, η_{abs}, depends on both the electronic absorption of the semiconductor, $\alpha(\nu, T)$, which is itself a function of frequency and temperature and the background absorption α_b in the form:[10]

$$\eta_{abs} = [1 + \alpha_b/\alpha(\nu, T)]^{-1} \qquad \text{Eq. 6.7}$$

Optimization of the absorption efficiency, and therefore lowering of the background absorption, depends on many of the same factors as the η_{exe}; requiring highly pure crystalline samples with high quality surfaces that that are devoid of traps and other non-radiative centers.

Yet another strategy to achieve cooling, is to focus on the ratio between excitation energy and emission energy, $\frac{\langle \nu_{em} \rangle}{\nu_L}$, by exciting electrons into states below the conduction band edge. This strategy relies on the principle of the Urbach tail, which denotes that absorption in a material is not a discontinuity at the band gap, but has an appreciable tail of low energy states below the bandgap.[17] Excited electrons may interact with phonons from the lattice and absorb into the conduction band at which point radiative recombination may occur as per usual. This was proposed for as a method to facilitate cooling in GaAs, where longitudinal optical (LO) phonons may couple to excited carriers in GaAs to enable absorption from the bandtail.[18] Interestingly, from this point of view GaAs is not an optimal material for optical cooling. The strength of the coupling between LO phonons and electrons, the so called fröhlich coupling, is 0.068 in GaAs, but ~10 times higher (0.514) in CdS,[19] another direct bandgap material with high quantum yield

(see Chapter 3). This property was exploited to achieve the first ever realization of net cooling in a semiconductor, namely CdS.[12]

It should be noted that optical cooling still remains an incredibly challenging problem, and since 2013 we have seen no additional work on laser cooling of semiconductors by other research groups. This is expected as each photon that is contributes to the cooling process via anti-Stokes photoluminescence will withdraw about E_{LO} from the material (38 meV in the case of CdS[20]), yet a single photon that contributes to heating deposits energy equal to the laser energy. Furthermore, dimensions play a critical role in the cooling or heating process. If the material is too thick then light trapping becomes an issue and anti-Stokes photons are readily reabsorbed. On the other hand, if the material is too thin then recombination at the surface, a non-radiative process (see discussion above), plays a significant role in carrier recombination of the material.[21] In the case of CdS, it was found that a balance between these two properties yields ~100 nm as an optimal belt thickness.[15] Yet even additional considerations arise at the nanoscale, such as the dependence of emission from the band edge on sample dimensions even well above the quantum confinement regime, which will affect both absorption and the ratio of mean emission energy to excitation energy.[22] These observations point to the need for another technique of efficient optical cooling. Surface plasmon-enhanced laser cooling of semiconductors is one such approach and will be focus of this chapter.

6.1.3: Theory of Surface Plasmon Enhanced Laser Cooling of Semiconductors

The previous chapters have been largely dedicated to engineering the optical properties of semiconductor materials by interfacing them with surface plasmon (SP) modes. Increased spontaneous emission due to the highly Purcell enhanced radiative recombination rates (Chapters 1, 3 and 4) resulted in orders of magnitude faster light emission and increased quantum yields (Chapters 4 and 5). Naturally we would like to explore the potential of surface plasmon-enhanced spontaneous emission for enhancing laser cooling of semiconductors, which itself is based on efficient light emission and thus a high radiative recombination rate. The first clue pointing to surface plasmon enhanced cooling comes from the maximum cooling power density, which may be derived from SBE theory as:[1]

$$\frac{NkT}{\tau_{rad}} \qquad \text{Eq. 6.8}$$

where τ_{rad} is the radiative recombination lifetime (i.e. ${\gamma_{rad}}^{-1}$). This is often cited as an advantage to achieve cooling in semiconductor materials, which often feature higher radiative rates than RE-doped glasses.[10] As demonstrated in Chapters 3-5, with an appropriately designed plasmonic optical cavity, the spontaneous emission rate of materials may be enhanced by up to 10^3, meaning, all things being equal, cooling should be enhanced by a similar amount in a plasmonically-coupled system.

Framing the problem from another perspective, in order to avoid heating the sample in question, as opposed to cooling it, places a limit on the minimum allowable

non-radiative recombination rate, which detracts from radiative recombination. Quantitatively, we may recast the cooling efficiency from SBE theory in terms of the minimum allowable non-radiative recombination lifetime:

$$\tau_{nrad}^{(\min)} = \frac{\nu_L}{\eta_e(\eta_{abs}\nu_L - \nu_{em})}\frac{1}{\gamma_{rad}} \qquad \text{Eq. 6.9}$$

This is similar to the expression obtained by Khurgin,[23] who originally proposes SP-enhanced optical cooling, but which also takes into account the absorption efficiency of the system, η_{abs}. This minimum non-radiative recombination time is generally on the order of microseconds, which places a high demand on the quality of the materials produced. As we can observe from the expression above, this requirement is significantly relaxed by employing a Purcell enhanced radiative rate, which should facilitate laser cooling of the material.

The question then remains as to what happens with the photons emitted into the optical cavity. As has been expounded in previous chapters, these are plasmonic optical cavities, which lead to extreme confinement of the optical field. More to the point, the light extraction efficiency of light emitted using our previous two geometries, i.e. core-shell (Chapter 3) and Ω-architecture (Chapters 4 and 5) is generally ~0.1-1%[24,25] which would offset any gains from an increased radiative rate. The key is that the objective is not simply to extract anti-Stokes photons from the system, but rather to prevent them from being reabsorbed by the semiconductor. If the plasmonically-active material may be separated from the semiconductor by a thermal insulator, such as glass, then Purcell-

enhanced anti-Stokes photons should excite SPs within the metal and dissipate into the metal, which itself is generally a good heat sink. The remainder of this chapter is dedicated to experimental verification of this hypothesis. First, laser cooling is explored in CdS nanobelts, following the prescription set out by Xiong et al.[12] The CdS samples are then integrated with a metal cavity to explore the possibility of surface-plasmon enhanced cooling in CdS nanostructures.

6.1.3.1: Enhanced Phonon-Electron Coupling in Plasmonically-Coupled CdS

As has been true throughout this thesis work, there is always an interplay between cavity electrodynamics and the solid state physical properties of the material. The previous section established the benefits of surface plasmon enhanced optical cooling due to the increased light emission that stems from Purcell enhancement, and which we have employed to generate highly enhanced luminescence from various semiconductor materials (see Chapters 3-5). High values of electron-phonon (fröhlich) coupling are critical to facilitating absorption into the conduction band from the Urbach tail of the semiconductor, which is mediated by lattice phonons. CdS already has a particularly high fröhlich coupling constant which is ~10 times that of GaAs (see section 6.1.2), yet Purcell enhancement in plasmonically-coupled CdS leads to orders of magnitude fastercarlight emission from high energy (hot) electronic states which itself was mediated by LO phonon scattering. Based on this observation of hot photoluminescence which mediates the surface-plasmon aided Purcell enhancement, we expect even higher values of electron-phonon coupling in plasmonically-coupled CdS. In order to quantify the

fröhlich coupling in CdS, we may examine the ratio of Stokes to anti-Stokes Raman scattering. Stokes Raman scattering involves phonon generation whereas anti-Stokes Raman scattering results in phonon-annihilation, thus the amount of anti-Stokes Raman scattering is proportional to the strength of the electron phonon interaction. The ratio of stokes to anti-Stokes Raman scattering intensities for the 1st order process (involving a single LO phonon) may be written as:

$$\frac{I_S}{I_{AS}} = Ae^{\hbar\omega_0/kT} \qquad \text{Eq. 6.10}$$

where A is a geometric pre-factor which varies with the experimental setup and is generally >1 and ω_0 is the LO phonon energy.[26,27] We characterize the experimental prefactor in our Raman setup by using a standard piece of bulk silicon wafer (111), which yields A=0.93. Likewise, second order anti-Stokes scattering is generally lower than second order Stokes scattering intensity and may be expressed as:[12,26]

$$\frac{{I_S}^{2LO}}{{I_{AS}}^{2LO}} = \frac{2e^{2\hbar\omega_0/kT} - e^{\hbar\omega_0/kT}}{2 - e^{\hbar\omega_0/kT}} \qquad \text{Eq. 6.11}$$

Using the above expressions we calculate anti-Stokes/Stokes ratios of 0.25 and 0.076 for the 1LO and 2LO processes respectively, in line with previously reported values.[12] Due to Bose-Einstein statistics, anti-Stokes scattering is generally lower than the stokes scattering. Anti-Stokes scattering can be increased by exciting resonantly, in other words, when the exciting laser is some integer multiple of the LO phonon energy away

from excitonic emission, i.e. $E_L = E_{ex} - nE_{LO}$, where E_L, E_{ex}, and E_{LO} are the laser energy, spectral position of the excitonic emission and the LO phonon energy respectively. The 532 nm laser in our setup provides such resonant excitation, given the emission from our CdS sample is typically at 501-505 nm (2.45-2.47 eV), which is ~3LO phonons (each with a value of 38 meV) above the 532 nm laser line. We explore the effect of resonant excitation in both bare and plasmonically-coupled CdS below. The Raman spectrum of bare CdS nanowire with d~200 nm (66.2) demonstrates strong anti-Stokes photoluminescence centered around -1157 cm^{-1} (2.474 eV). We also observe Raman peaks at -2LO (stokes) +2LO (anti-Stokes) and +3LO where -/+ denotes stokes shift and anti-Stokes shift respectively. Note, we do not observe first order scattering due to the notch filter which blocks a range around the exciting 532 nm that also blocks the 1LO peak at 306 cm^{-1}. After subtracting the luminescence background (Figure 6.2b) we obtain an anti-Stokes/Stokes ratio of the -2LO and +2LO peaks of 0.39, which is ~5 times the theoretical relative anti-Stokes activity. This is expected due to the near resonant excitation and broad photoluminescence spectrum, which facilitates spectral overlap between the excitonic emission and Raman overtones. In order to examine electron-phonon coupling in plasmonically-coupled CdS, nanowires in the same size range were first deposited on a transparent glass substrate, coated with with 5 nm of SiO_2 via atomic layer deposition and metallized with 300 nm of Ag (see sections 6.3 and 6.4 for experimental details). The samples were then excited and measured through the transparent glass substrate (see Figure 6.7a). Examination of the plasmonically-coupled nanowire (Figure 6.3, green curves) yields a stokes/anti-Stokes ratio of 3.327 (Figure

6.3b), which is well above unity and x44 the theoretical ratio Furthermore, second order Raman activity dominates over the photoluminescence background. This is evidence of the potentially enhanced electron-phonon coupling in plasmonically-coupled CdS, which in combination with Purcell enhancement, may be exploited to promote laser cooling in CdS nanostructures.

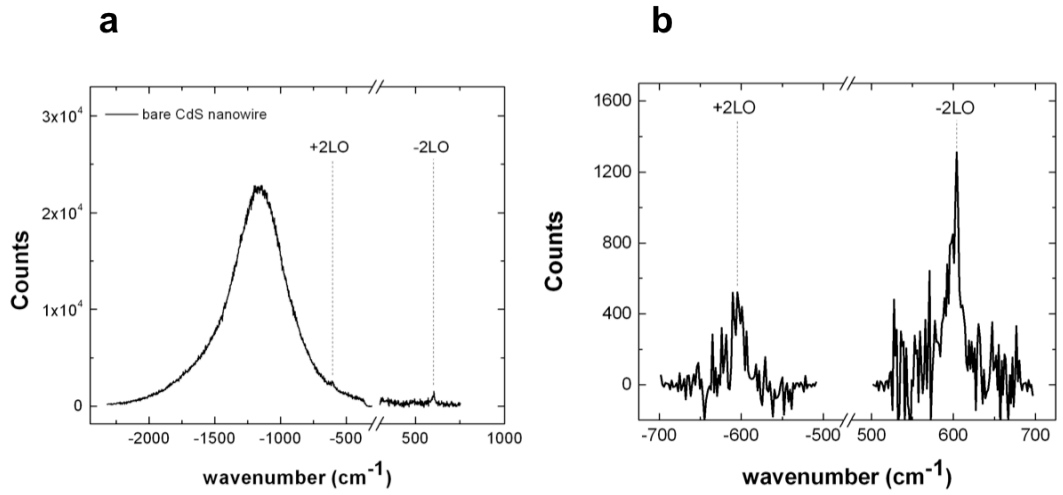

Figure 6.2 | Stokes and anti-Stokes Raman scattering for bare CdS nanowire (d~200 nm) with 5 nm conformal SiO_2 coating. a) Raman spectrum featuring broad photoluminescence peak centered at ~1157 cm-1 (2.474 eV) which is attributed to excitonic emission from CdS. b) Magnified view of region near 2LO Raman peaks in both the Stokes and anti Stokes region. Spectra have been baseline corrected to eliminate the photoluminescence background and provide accurate values of the Raman intensity.

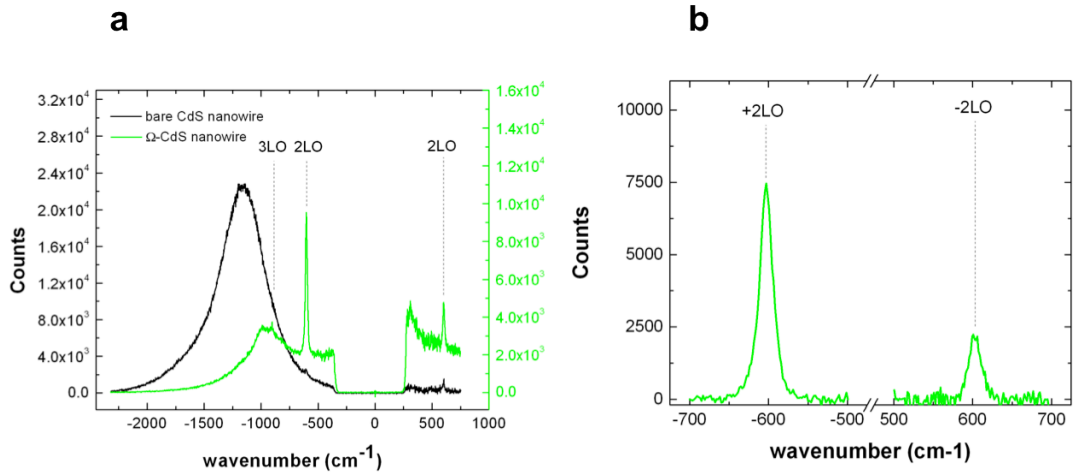

Figure 6.3 | Stokes and anti-Stokes Raman scattering for metal coated CdS nanowire with 5 nm conformal SiO_2 coating and 300 nm Ag metal shell (green curves). a) Raman spectrum featuring broad photoluminescence peak centered at ~980 cm^{-1} (2.452 eV) which is attributed to excitonic emission from CdS. The spectrum of a bare (non-metal coated) CdS nanowire is also plotted for comparison (black curve). b) Magnified view of region near 2LO Raman peaks in both the Stokes and anti Stokes region. Spectra have been baseline corrected to eliminate the photoluminescence background and provide accurate values of the Raman intensity.

6.2: Experimental

CdS nanobelts and nanowires were grown via the vapor liquid solid method as discussed in chapter 2. Atomic force microscopy revealed that the majority of samples have thickness, *d*, between 200 nm and 300 nm (Figure 6.4a and Figure 6.4b, cyan curve), which, as discussed in section 6.1.2, is too thick and will result in photon reabsorption, which hinders the optical cooling process. It was found that nanobelts and nanowires on the part of the growth substrate closest to the center of the furnace, that is generally at higher temperature and which sees precursor first, feature belts with thickness 70-110 nm (Figure 6.4b). These samples are appropriate for cooling and used in the remainder of this work, unless specified otherwise.

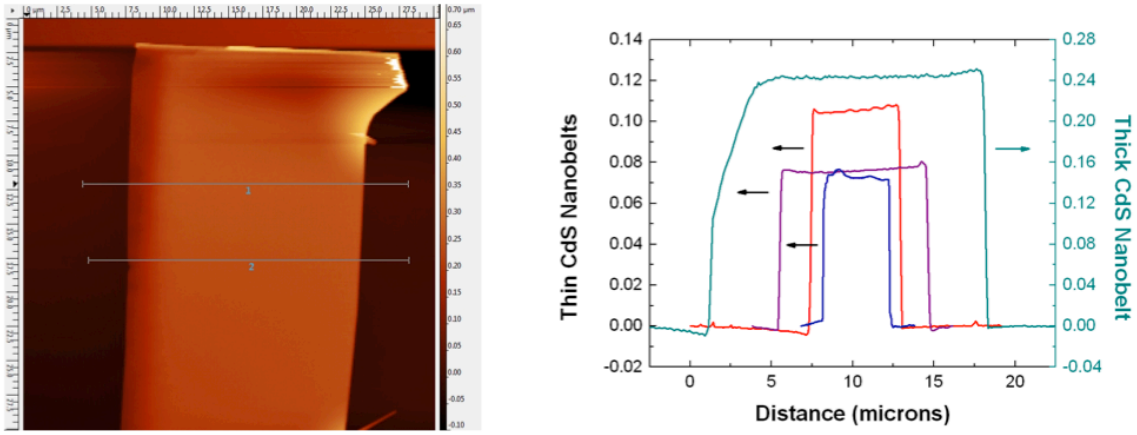

Figure 6.4 | Atomic force microscopy of CdS nanobelts. a) AFM image of typical thick CdS nanobelt with thickness of ~240 nm. b) AFM profiles of typical thick and thin CdS nanobelts as discussed in section 6.2.

Photoluminescence measurements were performed using a home-built laser-microscope-spectrometer setup depicted in Figure 6.5b. The probe laser is a solid-state diode laser operating at 473 nm, which is above the room-temperature band gap of CdS (~505 nm). The power is tuned to < 20 μW in order to avoid heating the sample. The probe laser beam is fed through a x60, 0.7 NA objective (Nikon) with a spatial resolution of 500 nm. The laser was focused to a spot size of ~1 micron. The resulting emission was collected using a spectrometer (Acton) with 0.1 nm resolution and a cooled CCD (Pixis 2K, Princeton Instruments). The 514.5 nm laser line of a continuous wave argon-ion laser (Coherent) was used as the pump beam (cooling laser) and focused through the same optics. A narrow-band holographic filter (Kaiser Optics) is used to filter out the 514.5 nm laser light leaving only the light emitted by the sample. Incident pump powers in the range 1-7 mW were used.

6.2.1: Differential Photoluminescence Thermometry

The sample temperature was monitored using Differential Luminescence Thermometry (DLT), a technique that monitors the shift in the photoluminescence spectra as a function of temperature.[10] The bandgap of semiconductors generally features a negative and quadratic dependence on temperature expressed by the empirical relation known as the Varshni formula.[19] The negative temperature dependence has been confirmed in CdS[28] and used to enable sub-Kelvin resolution during previous laser cooling experiments.[12] In our CdS nanobelts, the temperature dependence of the spectral position of the photoluminescence was measured by controlling the temperature the

sample stage and recording the peak position of the photoluminescence spectrum. First, the stage was cooled to 268 K and allowed to reach a steady state temperature within +/- 0.25 K. Photoluminescence was then excited at low power (see above) at several instances between 0-20 minutes (Figure 6.5a) which reveals that the sample thermalizes well under 10 minutes (a measurement which was further refined in section 6.3 below). In order to ensure complete thermalization of the sample, CdS belts were maintained at the set stage temperature for 10 minutes before recording the photoluminescence peak position. The temperature of the sample stage was then varied between 268 K and 312 K (under liquid nitrogen flow) in 4 K intervals (Figure 6.5b), which reveals a monotonic red shift of the photoluminescence spectrum with sample temperature. The change in temperature (with reference to 312 K) was plotted as a function of change in peak position (Figure 6.5c). In this narrow temperature range, the data is readily fit by a linear function, the slope of which agrees well with previous experimental investigation.[12] This curve is now used to extract the temperature of the sample from the shift in the spectral position of the photoluminescence.

At its most basic the DLT technique involves the use of two laser beams, a pump and a probe. The pump beam excites the sample above the bandgap (Figure 6.5d) and provides a base photoluminescence spectrum. The sample is then illuminated with the lower energy (but higher intensity) pump laser only; at an energy below the bandgap, which excites carriers into the Urbach tail of the semiconductor (see discussion above). The sub-bandgap excitation will cool the sample overtime, after which the pump is turned

off and the photoluminescence spectrum is taken with the probe beam only. If the sample is cooled then a net blue shift in the photoluminescence should be observed.

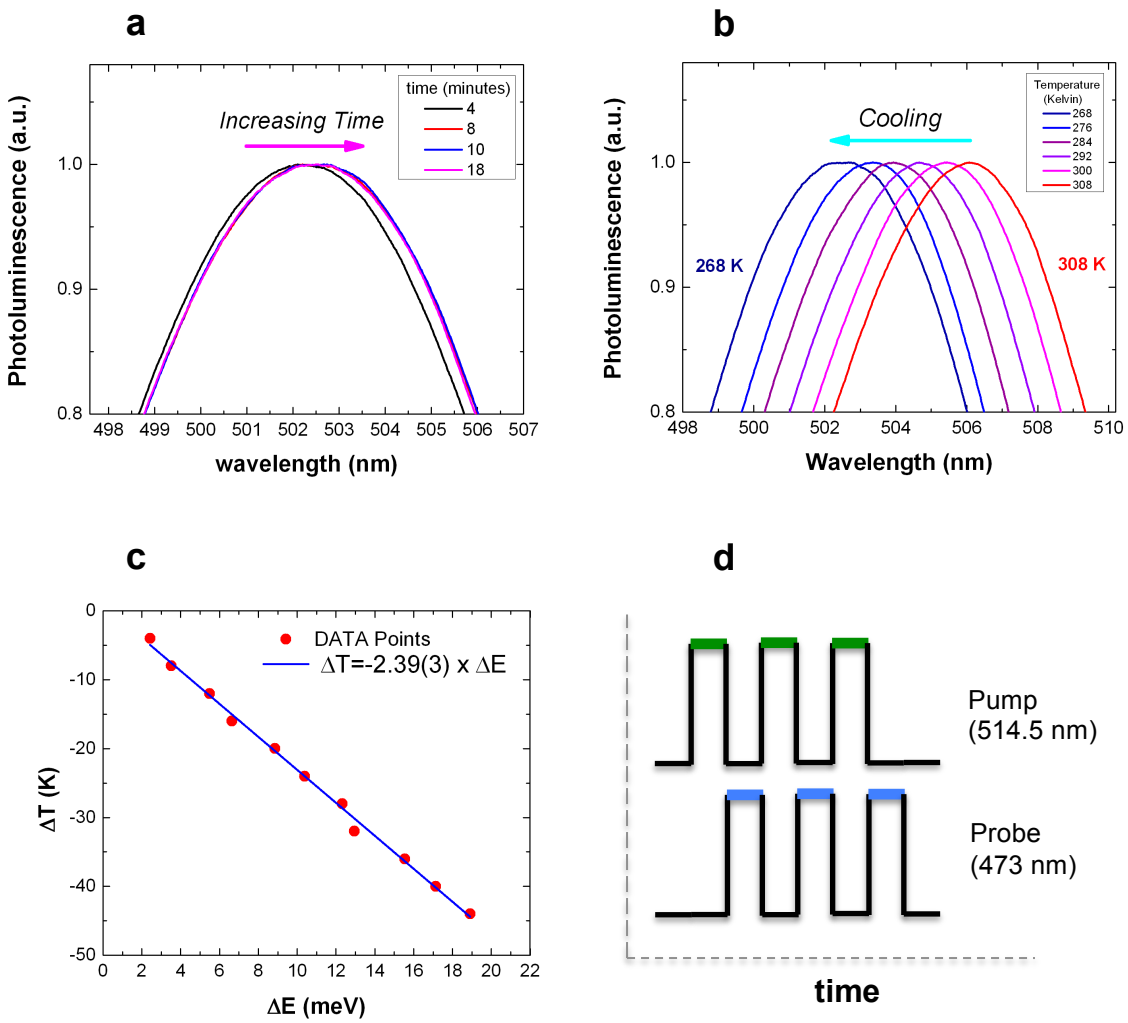

Figure 6.5 | Differential Luminescence Thermometry temperature calibration curve and schematic of measurement scheme. a) Photoluminescence at several times in the range 0-18 minutes for a CdS sample at a fixed temperature of 268 K. The photoluminescence peak position reaches a steady state within ten minutes of stabilization of the sample stage temperature. b) Photoluminescence spectra for a representative CdS samples at various temperatures in the range 268 K to 312 K (plotted at 8 K intervals for clarity). c) Plot of change in temperature, ΔT, vs. change in spectral peak position, ΔE, obtained from the photoluminescence data in (b). The blue line represents a linear fit to the data. d) schematic of measurement process using a pump laser (514.5 nm) for cooling and a low power probe laser (473 nm) for monitoring the shift in the photoluminescence spectrum.

In an ideal case, the sample to be cooled would be suspended in vacuum to avoid thermalization from the surroundings (which is essentially a large heat reservoir). In their previous work on cooling of CdS nanobelts, Xiong et al. suspended CdS nanobelts over ~3 μm x 3 μm pits on an SiO_2/Si substrate.[12] In this work, samples are suspended over a PMMA box pattern (Figure 6.6). The PMMA box pattern was constructed by spin-coating six layers of PMMA 950k A4 and exposing using an electron beam lithography (elionix) system. The trench box depth is ~1.7 μm as confirmed by atomic force microscopy. The PMMA box pattern was chosen as it promotes cooling from both geometric and materials science considerations. For a CdS nanowire over a hole, the thermal loss, P_{Loss}, into the substrate may be modeled via:[15]

$$P_{Loss} = -2kM\frac{\Delta T}{\Delta L} \qquad \text{Eq. 6.12}$$

where k, M, ΔT, and ΔL are the thermal conductivity of CdS, the cross sectional area of the nanobelt, the difference in temperature between the cooling point on the sample (area excited by pump laser spot) and substrate, and the distance between the sample cooling spot to the substrate wall. In the boxed cooling pattern we may often approximate ΔL in at least the lateral or longitudinal dimension as infinite. From a materials property point of view, the thermal conductivity of PMMA (0.167 – 0.250 W/mK) is ~10 times lower than that of thermally grown SiO_2 (1.4 W/mK)[29] and should aid in preventing thermalization to the substrate.

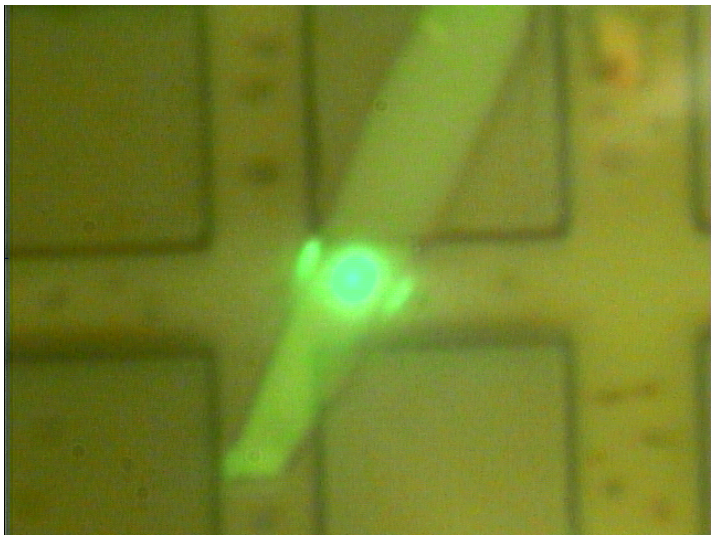

Figure 6.6 | Optical image of CdS nanobelt suspended over PMMA boxes (~9 μm x 9 μm) with a ~4 μm separation. The bright emission from the nanobelt is anti-Stokes photoluminescence resulting from excitation below the bandgap at (with the 514.5 nm pump laser).

6.3: Initial Results and Discussion

When pumped with the sub-bandgap 514.5 nm (pump) laser, CdS nanobelts typically feature bright emission at the band edge (Figure 6.7a). Before attempting to measure cooling in plasmonically-coupled CdS nanostructures, attempts were made to reproduce the results of Xiong et. al.[12] on CdS nanobelts. In order to avoid thermalization of the sample with the substrate, ideally the probe measurement would be made immediately after the pump laser is shut off. As a first order experiment, CdS nanobelts were excited below the band gap, with the pump laser beam, and the anti-Stokes spectrum was monitored as a function of time. In other words this is a single-beam experiment. Though in general it is preferable to monitor temperature with the shift in

probe beam as the temperature dependence of "Stokes" (or normal) photoluminescence is well documented,[19] we may still look for qualitative signs of cooling as the anti-Stokes photoluminescence should itself blue shift with time.

The anti Stokes spectrum of a CdS nanobelts with suboptimal dimensions (thickness *d*~200-300 nm) are shown in Figure 6.7, where these CdS nanobelts typically feature bright photoluminescence when excited with the pump laser below the band edge (Figure 6.7a). The majority of samples measured show no change in the spectral position of the emission peak as a function of time, which is expected given all of the considerations established above, yet two different samples demonstrated a monotonic blue shift as a function of time when illuminated for up to 1 hour with the pump (514.5 nm) laser at 2 mW (Figure 6.7b, c). Note, the samples were excited until the anti Stokes photoluminescence peak no longer moved, at which point the sample has reached saturation (cooling is offset by thermal loss to the surroundings and a cooling efficiency which is < 0), a feature which was also observed in previous experiments.[12] The total blue shift in the spectrum is still <1nm after 1 hour of pumping and certainly less than the ~4 nm blue shift measured by Xiong et al., which led to cooling by up to 40 K, but the results are still sufficient to justify pursuing further experimentation (i.e. pump-probe measurements).

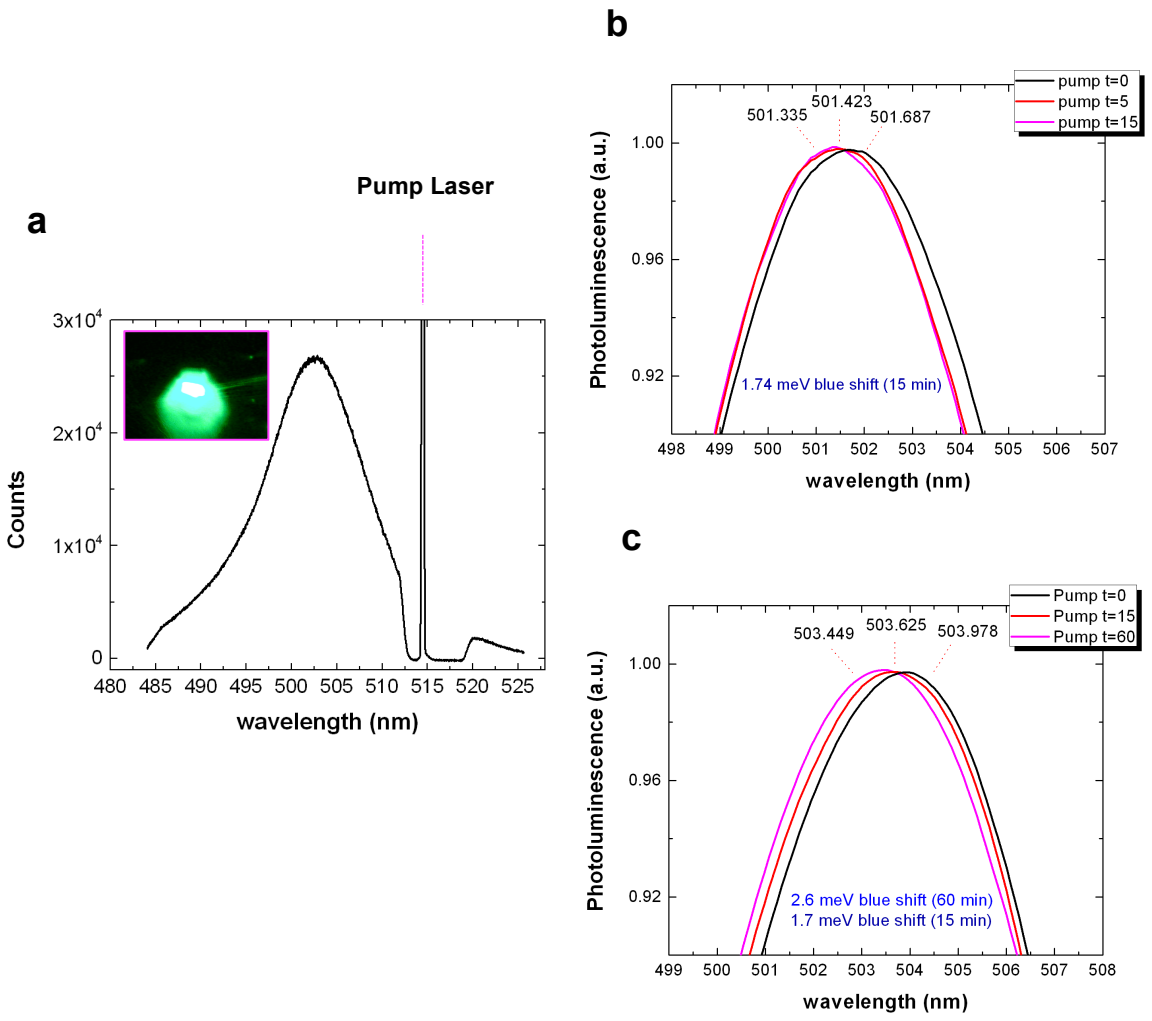

Figure 6.7 | Anti Stokes photoluminescence in bare CdS nanobelts with thickness *d*~200-300 nm. a) Photoluminescence in CdS nanobelt excited with the 514.5 nm line of a CW laser (inset: optical image of anti Stokes photoluminescence excited with pump laser). b) Magnified view of anti Stokes photoluminescence spectrum in CdS nanobelt featuring a blue shift of ~1.74 meV (~0.3 nm), which reaches a steady state after 15 minutes of excitation with the pump laser. c) Magnified view of anti Stokes photoluminescence spectrum in CdS nanobelt featuring a blue shift of 2.6 meV (~0.5 nm) after 1 hour of excitation with pump laser.

Pump-probe measurements were performed using the experimental conditions described in section 6.2, which closely resemble those used in previous CdS cooling experiments.[12] Figure 6.8 features a representative data set, where the photoluminescence (resulting from excitation with the probe laser) is taken at room temperature (Figure 6.8, black curves). The sample is then pumped for fifteen minutes and a second probe photoluminescence measurement is made immediately thereafter (Figure 6.8a, red curve). No shift in the photoluminescence spectra is observed. A more sensitive measure of the onset of cooling (or heating) is provided by plotting the difference between the initial spectrum and the spectrum after some time (DLT curve). Cooling, or a net blue shift in the spectrum will be appear as a peak followed by a dip in the DLT spectrum, due to greater activity in the blue part of the spectrum, whereas heating will appear as a valley followed by a peak. The DLT curve (figure 6.8a, magenta curve) reveals no such activity with a small dip in the middle due to noise in the probe spectrum, which is taken at low power (see section 6.2 for details).

In order to further promote cooling, CdS nanobelt samples were uniformly coated with a 5 nm layer of SiO_2 via atomic layer deposition, which is known to passivate the surface of CdS (see Chapter 2 for a discussion on the improved optical properties of surface-passivated CdS and Chapter 3, section 3.2 for the experimental details). Moreover, as discussed in section 6.1.2, in single crystalline CdS nanostructures the surface is the largest contributor to non-radiative recombination, the passivation of which results in improved free exciton radiative recombination.[28] As can be observed in Figure 6.8c, there is no further improvement in the cooling performance of these samples. This

observation is somewhat expected given the constraints on the cooling efficiency (discussed above) which require a quantum yield of near unity and almost no parasitic absorption. Furthermore, nanostructures need to be of the appropriate dimensions to avoid light trapping (and subsequent reabsorption) but also minimize surface effects (see section 6.1.2).

Still, given the initial positive results with single-beam measurements, we first examine the issue of thermalization to the substrate. As discussed during the initial measurements with a single laser beam and in section 6.2, this is an ever-present issue. In order to experimentally determine whether lack of cooling is due to the sample's surroundings, the entire sample stage was heated (a feature of the Janis ST-500 cryostat) by 3 K-5 K, where the instantaneous temperature was monitored as a function of time. The Stokes photoluminescence (due to excitation with the probe laser) was monitored concurrently. If the samples instantly thermalized with the surroundings then we would expect the change in the photoluminescence peak position to follow the change in stage temperature as a function of time and saturate (stop shifting) once the stage temperature reaches its steady state value. As observed in two separate measurements in different temperature ranges (Figure 6.9) this is not the case. The sample begins to thermalize after ~ 10 seconds and does not reach equilibrium with the environmental temperature until between 40 seconds (Figure 6.9a) and 20 seconds (Figure 6.9b) after the stage has reached equilibrium, which points to the effectiveness of the patterned-PMMA coated substrate for thermal isolation (see section 6.2) and excludes thermalization as a cause for lack of observable optical cooling in the pump-probe measurements.

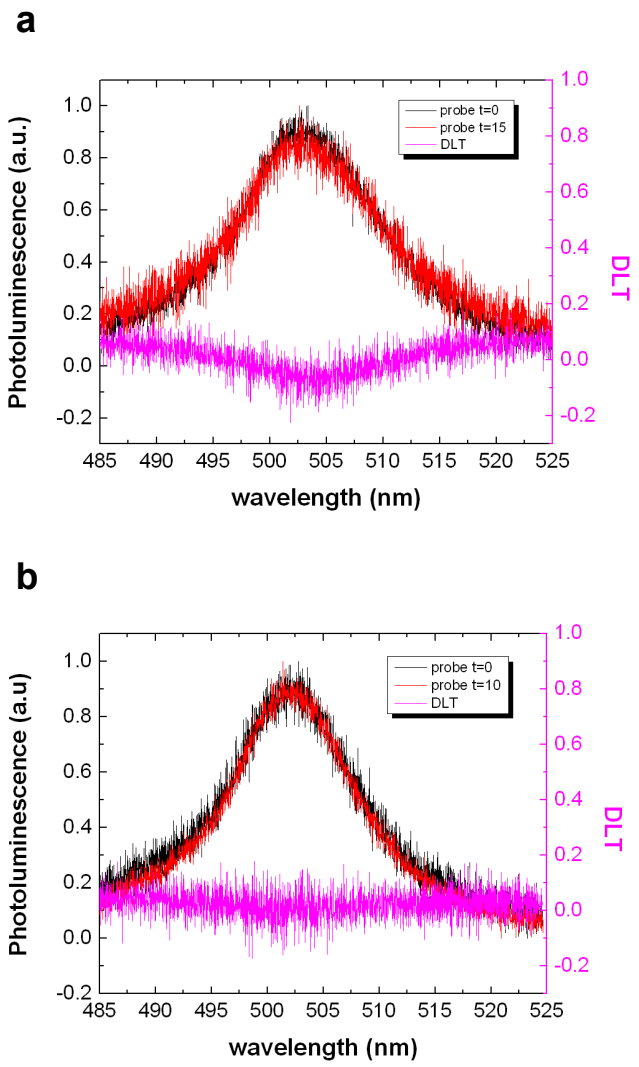

Figure 6.8 | Pump-probe differential luminescence thermometry of bare and passivated CdS nanobelts. a) Stokes Photoluminescence spectra of a CdS nanobelt featuring the spectrum at time t=0 (black curve) and t=15 min (after pump excitation; red curve). The difference spectrum (DLT curve) is plotted in magenta. c) Stokes Photoluminescence spectra of a CdS nanobelt passivated with SiO_2 featuring the spectrum at time t=0 (black curve) and t=10 min (red curve). The difference spectrum (DLT curve) is also plotted in magenta.

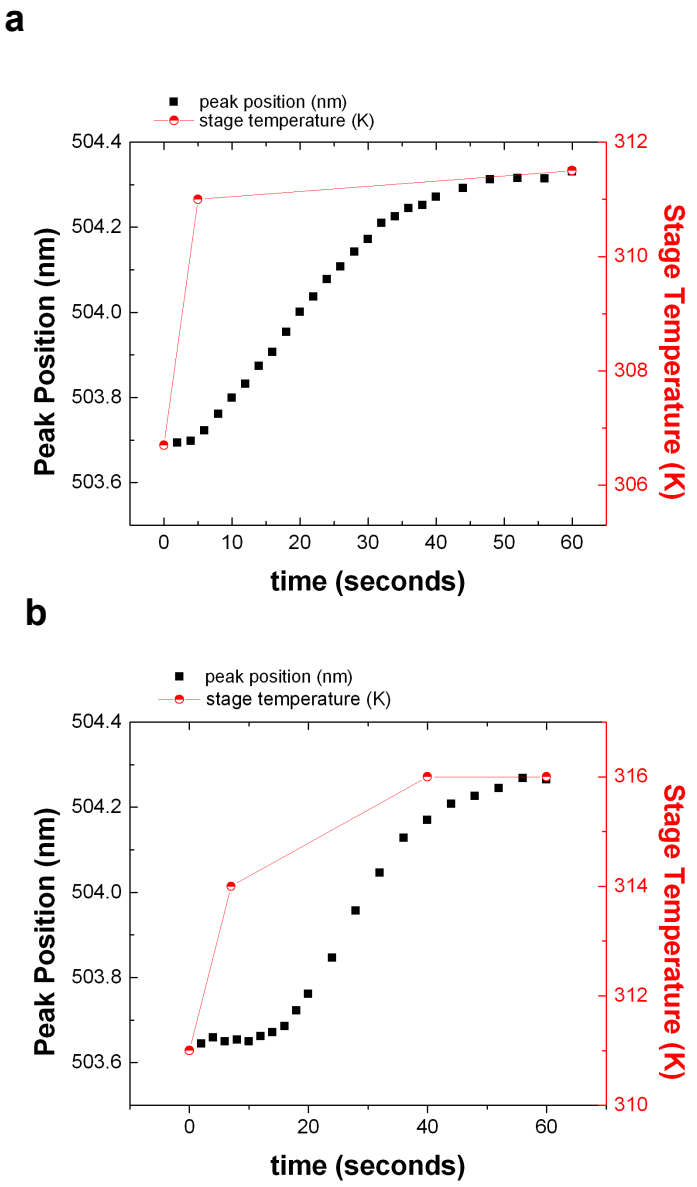

Figure 6.9 | Probe photoluminescence peak position and sample stage temperature vs. time for two bare CdS nanobelt samples in the temperature range a) 307 K-311 K and b) 311 K-316K.

Thus, the sensitive geometric and sample quality considerations discussed in previous sections are likely the most significant barrier to optical cooling. As postulated in section 6.1.3, coupling of carriers in CdS to surface plasmons may relax some of the aforementioned constraints through increased radiative recombination. Furthermore, the realization of highly Purcell-enhanced light emission has been a focus of this thesis. What follows is the first experimental pursuit, to the author's knowledge, of surface plasmon-enhanced optical cooling in a semiconductor system.

6.4: Cooling of Plasmonically-Coupled Cadmium Sulfide

In order to explore plasmonically-enhanced optical cooling, the CdS nanobelts discussed in the previous section were metallized with a thin (15 nm) layer of silver via electron-beam evaporation (Thermionics). The thin silver film enables laser excitation and measurement of the emission from the top (through the silver film) as depicted in Figure 6.10a. Interestingly, a modicum of cooling was observed in one of the samples (Figure 6.10b), which is confirmed via the DLT curve that features the characteristic peak followed by valley (see previous section). A magnified view near the spectral peak (Figure 6.10c) reveals a small shift (<1 nm, 0.7 meV) corresponding to a net cooling of ~1.7 K, which again, is significantly lower than the maximum cooling of 40 K achieved in previous work. Still, this is the only observation finite cooling using the pump-probe method compared to previous (and passivated) CdS nanobelts.

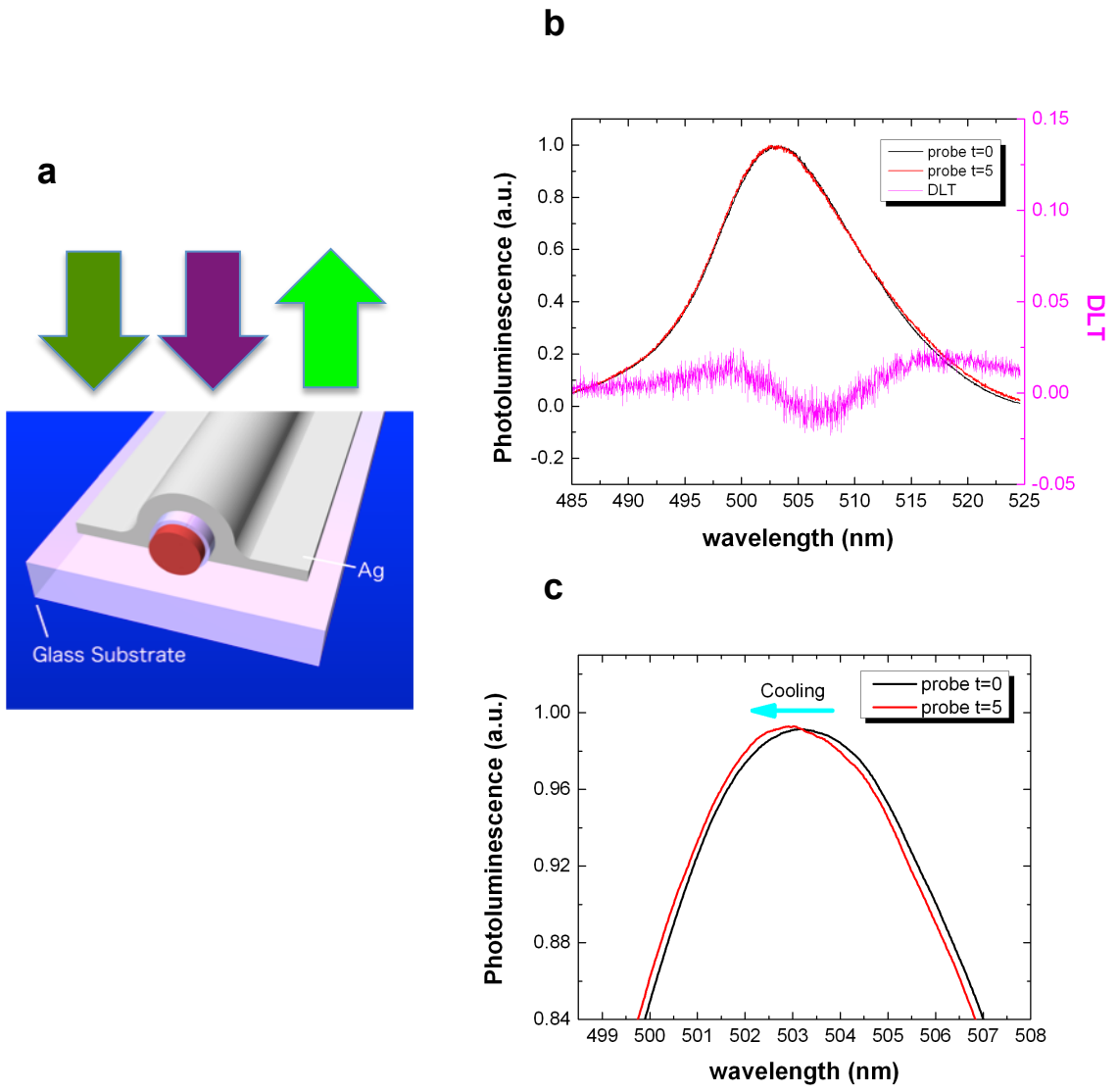

Figure 6.10 | Laser cooling of plasmonically-coupled CdS in geometry optimized for top-down excitation and measurement. a) Schematic of CdS integrated with a 15 nm thick Ag film. Excitation is performed through the Ag film as denoted by the dark green and purple arrows. Emission is also measured through the substrate (bright green arrow). b) Stokes Photoluminescence spectra of a CdS nanobelt featuring the spectrum at time t=0 (black curve) and t=15 min (after pump excitation; red curve). The difference spectrum (DLT curve) is plotted in magenta. c) Magnified view of anti-Stokes photoluminescence (excited with probe laser) of data presented in (b).

In order to promote SP-enhanced cooling, first a thicker silver film (300 nm) is deposited. A thicker film of metal will ensure continuity of the film and lead to lower optical losses. In addition, and perhaps more importantly, a thicker metal film should serve as a superior heat sink for dissipation of heat generated from surface plasmon oscillations. On the other hand, a thick metal film, which is greater than the skin depth of silver at optical frequency (~15 nm), will prohibit excitation from the top surface. Thus, the entire sample was constructed on a transparent glass slide (Fisher Scientific, 150 μm thick), which enabled excitation and detection from the bottom surface (through the substrate) as detailed in Figure 6.11a. Measurement of the samples following the same experimental conditions described above did not reveal any cooling of the sample. In order to further promote cooling, the same measurements were repeated under resonant excitation, by previously tuning the sample temperature to enable light emission at an energy which is an integer of the LO phonon energy, nE_{LO}, away from the excitation laser. In order to resonantly excite the sample at 1LO phonon energy away from the laser the stage temperature was increased to 319K to tune the photoluminescence peak to Energy, $E=E_{Laser}+E_{LO}$ = 2.414 eV+0.038 eV corresponding to ~506 nm. Interestingly, cooling was only observed at 2LO resonant excitation corresponding to a sample temperature of 229K and sample emission at ~498.5 nm (Figure 6.11b-c). As can be observed the probe photoluminescence spectrum blue shifts after 10 minutes of excitation with the pump laser (6.11b), before returning to its original position after 5 minutes without pumping (Figure 6.11c). Still, < 1 meV of shift is observed (0.8 meV)

corresponding to ~2 K of cooling, a far cry from the 40K of cooling achieved by the Xiong group with bare CdS nanobelts.[12] It should be noted that no cooling was observed for bare nanowires under similar conditions.

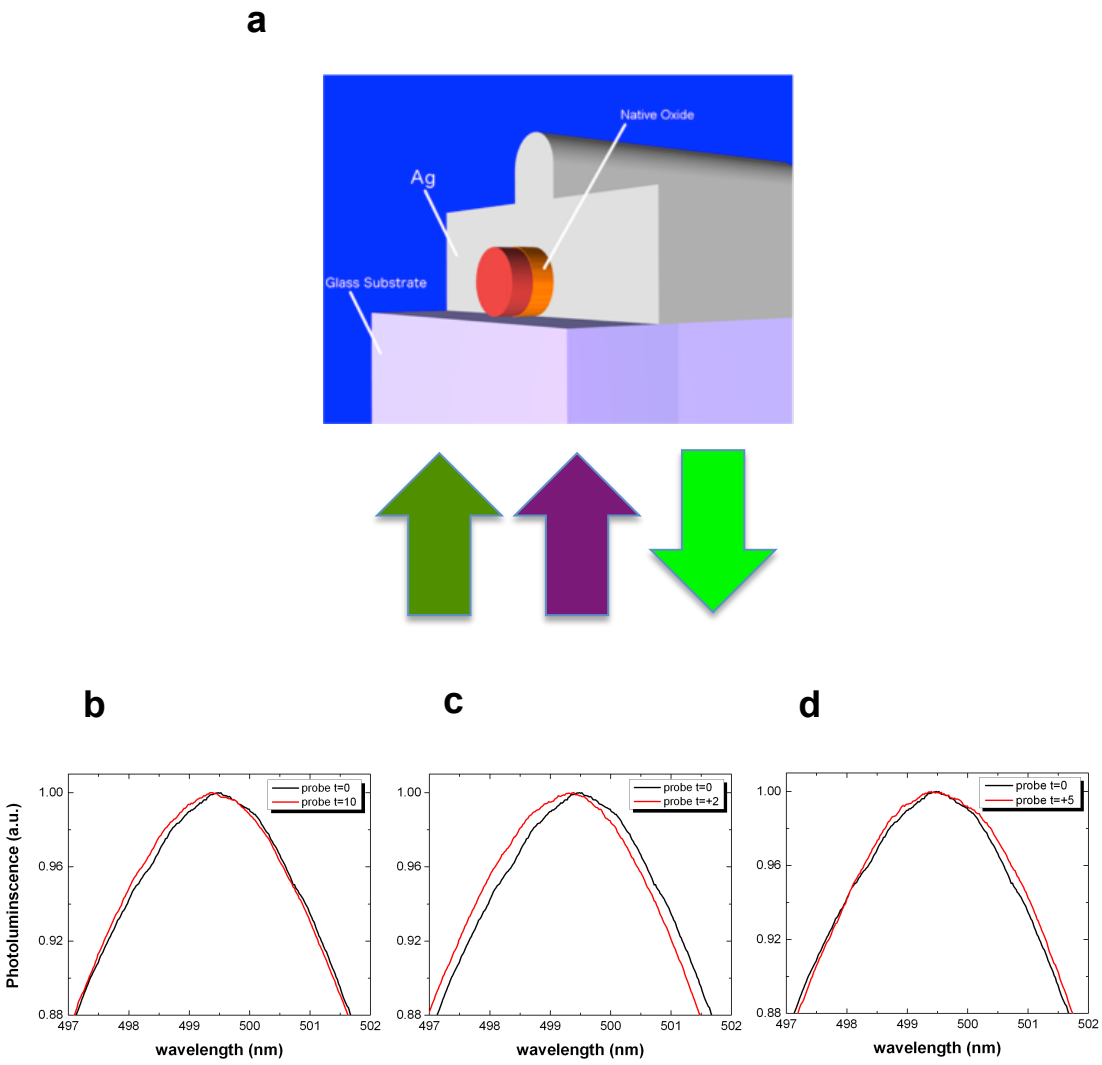

Figure 6.11 | Laser cooling of plasmonically-coupled CdS using inverted geometry. a) Schematic of CdS integrated with a 300 nm thick silver film. Excitation is performed through the substrate as denoted by the dark green and purple arrows. Emission is also measured through the substrate (bright green arrow). b-d) Magnified view of Anti-Stokes photoluminescence (excited with probe laser) b) after 10 minutes of cooling, c) after 2 minutes of warm up time (after excitation with pump laser has ceased) and d) 5 minutes of warm up time. The original probe photoluminescence spectrum at t=0 is plotted in black in all three plots as a reference point.

6.5: Conclusions and Future Work

By coupling CdS nanobelts to surface plasmons sustained within a metal shell we were able to show improvements in the optical cooling performance of CdS over its uncoupled (bare) counterpart. Several geometries were explored during the optimization process, which highlights the extreme sensitivity of optical cooling to sample growth conditions, sample geometry, and material properties. Still, significant additional work is required to (1) improve the cooling performance of these plasmonically-coupled structures and (2) elucidate the role of surface plasmons in mediating anti-Stokes photoluminescence. In order to improve cooling performance, a thickness dependent study of the insulating (SiO_2) spacer layer is essential. Whereby, increasing thermal isolation will be balanced with decreased efficiency of surface plasmon excitation. Details of this potential study are expounded in Chapter 7, future work. (3) Resonant excitation must also carefully explored as it will be sensitively dependent on both laser excitation energy as well as the mean emission energy which itself is sensitive to sample dimensions at the nanoscale (see section 6.1.2) and temperature. Finally, the role of surface plasmons in plasmonically-coupled CdS nanobelts must be clarified and will require Purcell factor as well quantum yield calculations, which may be performed using the finite difference time domain analysis techniques that have been developed in previous chapters.

References

1 Sheik-Bahae, M. & Epstein, R. I. Optical refrigeration. *Nature Photonics* **1**, 693-699, doi:Doi 10.1038/Nphoton.2067.244 (2007).

2 Hecht, E. *Optics*. 4th edn, (Addison-Wesley, 2001).

3 Phillips, W. D. (Nobel Media AB 2013, Nobelprize.org, 1997).

4 Chu, S. (Nobel Media AB 2013, Nobelprize.org, 1997).

5 Cohen-Tannoudji, C. (Nobel Media AB 2013, Nobelprize.org, 1997).

6 Eric A. Cornell, W. K., Carl E. Wieman. (Nobel Media AB 2013, Nobelprize.org, 2001).

7 Pringsheim, P. Zwei Bemerkungen über den Unterschied von Lumineszenz- und Temperaturstrahlung. *Zeitschrift für Physik* **57**, 739-746 (1929).

8 Epstein, R. I., Buchwald, M. I., Edwards, B. C., Gosnell, T. R. & Mungan, C. E. Observation of Laser-Induced Fluorescent Cooling of a Solid. *Nature* **377**, 500-503, doi:Doi 10.1038/377500a0 (1995).

9 Reif, F. *Fundamentals of statistical and thermal physics*. (McGraw-Hill, 1965).

10 Sheik-Bahae, M. & Epstein, R. I. Laser cooling of solids. *Laser Photonics Rev* **3**, 67-84, doi:Doi 10.1002/Lpor.200810038 (2009).

11 Sheik-Bahae, M. & Epstein, R. I. Can laser light cool semiconductors? *Physical Review Letters* **92**, doi:Doi 10.1103/Physrevlett.92.247403 (2004).

12 Zhang, J., Li, D. H., Chen, R. J. & Xiong, Q. H. Laser cooling of a semiconductor by 40 kelvin. *Nature* **493**, 504-508, doi:Doi 10.1038/Nature11721 (2013).

13 Adachi, S. *Properties of Group-IV, III-V and II-VI Semiconductors*. (Wiley, 2005).

14 Sheik-Bahae, M., Imangholi, B., Hasselbeck, M. P., Epstein, R. I. & Kurtz, S. 611518-611518-611513.

15 Li, D. H., Zhang, J. & Xiong, Q. H. Laser cooling of CdS nanobelts: Thickness matters. *Optics Express* **21**, 19302-19310, doi:Doi 10.1364/Oe.21.019302 (2013).

16 Thooft, G. W. & Vanopdorp, C. Determination of Bulk Minority-Carrier Lifetime and Surface-Interface Recombination Velocity from Photoluminescence Decay of a Semi-Infinite Semiconductor Slab. *Journal of Applied Physics* **60**, 1065-1070, doi:Doi 10.1063/1.337399 (1986).

17 Klingshirn, C. F. *Semiconductor Optics*. 3 edn, (Springer-Verlag, 2007).

18 Khurgin, J. B. Role of bandtail states in laser cooling of semiconductors. *Physical Review B* **77**, doi:Doi 10.1103/Physrevb.77.235206 (2008).

19 Adachi, S. *Properties of Group-IV, III-V and II-VI Semiconductors*. (Wiley, 2005).

20 Gross, E., Permogor.S, Travniko.V & Selkin, A. Hot Excitons and Exciton Excitation Spectra. *Journal of Physics and Chemistry of Solids* **31**, 2595-&, doi:Doi 10.1016/0022-3697(70)90254-4 (1970).

21 Liu, X. F., Zhang, Q., Xing, G. C., Xiong, Q. H. & Sum, T. C. Size-Dependent Exciton Recombination Dynamics in Single CdS Nanowires beyond the Quantum Confinement Regime. *J Phys Chem C* **117**, 10716-10722, doi:Doi 10.1021/Jp312850w (2013).

22 Li, D. H., Zhang, J. & Xiong, Q. H. Surface Depletion Induced Quantum Confinement in CdS Nanobelts. *ACS Nano* **6**, 5283-5290, doi:Doi 10.1021/Nn301053r (2012).
23 Khurgin, J. B. Surface plasmon-assisted laser cooling of solids. *Physical Review Letters* **98**, doi:Doi 10.1103/Physrevlett.98.177401 (2007).
24 Cho, C.-H., Aspetti, C. O., *et al.* Tailoring hot-exciton emission and lifetimes in semiconducting nanowires via whispering-gallery nanocavity plasmons. *Nat Mater* **10**, 669-675 (2011).
25 Cho, C.-H., Aspetti, C. O., Park, J. & Agarwal, R. Silicon coupled with plasmon nanocavities generates bright visible hot luminescence. *Nat Photon* **7**, 285-289 (2013).
26 Cardona, M. & Guntherodt, G. Light-Scattering in Solids II: Basic Concepts and Instrumentation. *Top Appl Phys* **50** (1982).
27 Jellison, G. E., Lowndes, D. H. & Wood, R. F. Importance of Temperature-Dependent Optical-Properties for Raman Temperature-Measurements for Silicon. *Physical Review B* **28**, 3272-3276, doi:Doi 10.1103/Physrevb.28.3272 (1983).
28 van Vugt, L. K. *et al.* Variable Temperature Spectroscopy of As-Grown and Passivated CdS Nanowire Optical Waveguide Cavities. *The Journal of Physical Chemistry A* **115**, 3827-3833, doi:10.1021/jp108167t (2011).
29 *MIT Material Properties Database*.

Chapter. 7 Conclusions

7.1: Future Work

In order to confirm the generality of surface plasmon induced hot photoluminescence, we would like to apply this method to other material systems and in a different spectral range. Of particular interest would be germanium, again a dark material normally used for electronic applications. With its low bandgap of 0.67 eV,[1] we may extend hot luminescence to the NIR range and, in particular, enable operation near the technologically relevant telecommunications wavelength (1.55 μm). Furthermore, this will allow other plasmonically-active materials to be incorporated, such as highly doped semiconductors and oxides, which may be more compatible with modern electronic fabrication techniques and which are more amenable to tuning of their plasmon resonance based on carrier doping.[2]

Though much work has been performed on the characterization of hot luminescence in silicon, time resolved measurements could potentially provide yet another way of differentiating between different hot emission pathways which depend on both electronic and phonon structure of the material (see Chapters 4 and 5). Time resolved photoluminescence spectroscopy involves a pulsed excitation source and a high-intensity gate beam that is used to induce transient birefringence on the Kerr medium (see section Chapter 3, section 3.6.1). In general, there is a broad luminescence background in the visible range due to auto fluorescence from the Kerr medium, thus, the intensity of

the photoluminescence signal from the sample must be maximized in order to enable the time resolved measurement.[3] This may be accomplished by making ensemble measurements, a technique which proved successful in measuring the spontaneous emission lifetime of plasmonically-coupled CdS in Chapter 3.[4]

Attempts to perform these measurements on an ensemble of plasmonically-coated Si nanowires with sizes in the range d=40 nm-80 nm (as used in Chapter 4)[5] were unsuccessful due to the low quantum yield of the samples. This is expected as the quantum yield of indirect bandgap semiconductors is generally low and estimated to be 1.4% for the plasmonically-coupled Si nanowires. Furthermore, emission was found to be highly sensitive to the size of the sample, where the previously mentioned quantum yield only applies to "resonantly" sized plasmonically coupled Si nanowires. It would be beneficial to attempt these measurements on "large" plasmonically-coupled Si nanowire samples, such as those used in Chapter 5, with diameters in the vicinity of d~150 nm. These nanowires should generally feature a higher external quantum yield as incoupling and outcoupling of light is facilitated in a larger structure. Furthermore, when comparing the d=150 nm nanowire to d=70 nm nanowire the amount of active material is increased ~4.6 fold in volume. Pulsed excitation can also present some difficulty in excitation of hot photoluminescence, as the exciting laser pulse is only pseudo-monochromatic with a width of ~50 nm in the frequency domain. In order to examine the possibility of exciting hot photoluminescence in plasmonically coupled silicon under pulsed excitation, a plasmonically-coupled sample with d~150 nm was excited with a continuous-wave Ar+ laser operating at 457.9 nm with a 2 mW output and the 140 fs pulse of a Ti:Sapphire

laser tuned to 458 nm and also operating at 2 mW time-averaged power. A broad hot luminescence signal was effectively generated from the plasmonically-coupled sample (Figure 7.1, magenta curve), albeit at lower counts for the previously mentioned reasons.

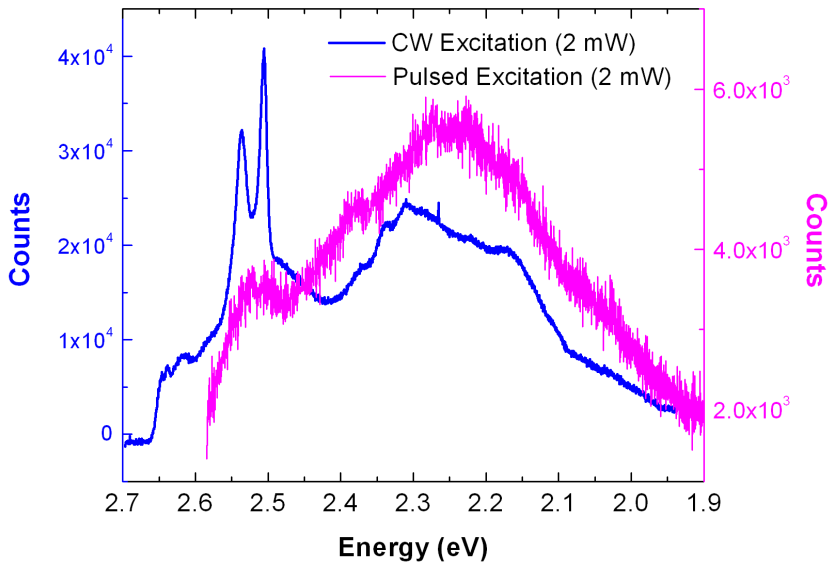

Figure 7.1 | Photoluminescence of plasmonically-coupled Si nanowire (*d*~150 nm) excited with the 457.8 nm laser line of an Argon-ion laser (continuous wave, blue curve) and Ti:Sapphire laser (pulse width 140 fs, 80 MHz repetition rate) tuned to 458 nm (magenta curve).

With regards to surface-plasmon enhanced optical cooling of CdS, a critical parameter is the separation of the metal cavity from the active CdS core. As expounded in the original theoretical treatment by Khurgin et. al., ideally, the spacer between the metal and semiconductor would be a vacuum.[6] This would serve to both generate the high intensity surface plasmon fields which have been shown to appear in high index semiconductor-insulator-metal systems[4,7,8] while thermally isolating the metal from the

semiconductor and allowing heat dissipation to occur in the metal. Interestingly, the SiO_2 used as the insulating spacer layer, which is deposited via atomic layer deposition (see Chapter 2 and Chapter 3, section 3.2) is not the ideal material here. From an experimental point of view, perhaps a more adequate material would be highly porous SiO_2, which would maintain its low index character, while behaving as a superior thermal insulator. Nanoporous silica thin films, with nanopores in the range 5-10 nm have been produced via solution methods[9] where the sample and porous SiO_2 film and substrate are interfaced via dip-coating, a method that is amenable to VLS grown CdS samples on a growth substrate (see Chapter 2). Furthermore, the distance between the emitter (in this case CdS) and plasmonically-active material (i.e. Ag) is critical in determining the efficiency of light emission[10] where the optimal distance will depend on both geometry and refractive index. Thus, a detailed study with variable-thickness porous SiO_2 should be conducted.

7.2: Concluding Remarks

This thesis was dedicated to the integration of semiconductor nanowires with plasmonic optical cavities (i.e. optical antennas) to achieve unprecedented levels of enhancement in their optical properties, with a focus on light emission. The groundwork for surface-plasmon enhanced photoluminescence in semiconductors was established in Chapter 3, where CdS, a direct bandgap semiconductor, was interfaced with silver in a core-shell geometry. Though the nanocavity plasmon modes hosted by the system have moderate quality factors (~50), the mode volumes are on the order of 10^{-4}. In other

words, light in this hybrid-semiconductor/plasmon system is 10^4 times more confined than in free space. The high Q/V_m values led to Purcell factors on the order of 1000, that is spontaneous emission from excited charge carriers is 1000 times faster in this system than in the bulk. Such high radiative recombination rates, which are a result of the electromagnetics of the optical cavity, significantly altered the photoluminescence spectrum of CdS, enabling light emission from charge carriers in the excited state before they have time to relax to the ground state, the so called "hot"-photoluminescence. Furthermore, this process was shown to be mediated by optical phonons in CdS, which highlights the interplay between optical physics and solid-state physics that is prevalent throughout this thesis.

In the latter part of Chapter 3, plasmonic cavity modes in the core-shell architecture were used in the reciprocal process, to enable broadband enhancement of light absorption in a computational study of plasmonically-coupled Ge and CdSe nanowires. Interestingly by placing what is essentially a mirror around the nanowires, but of the appropriate dimensions for plasmonic modes, nanowires were shown to absorb more light than their bare counterparts with straightforward applications in nanowire based photodetector and solar cell design.

In Chapter 4, the lessons learned about hot carrier luminescence in plasmonically-coupled CdS, a light emitting material, were applied to Si, a dark material. In Si, due to its indirect band structure, excess energy is converted to heat much more readily than to emitted photons, a system that is starkly different than CdS. The implications of light

emitting Si are substantial noting Si is ubiquitous in modern electronics. As expounded in Chapter 4, there is a significant push from industry to explore Si as an optoelectronic material where a Si light source would represent a significant milestone. Hot photoluminescence via coupling to high Q/V_m plasmonic modes led to broadband hot-photoluminescence with a quantum yield of ~1.4%, a substantial increase compared to the 10^{-4}-10^{-6} typically reported for bulk Si. Moreover, this was achieved in non-quantum confined silicon, with dimensions that are amenable to modern electronic device fabrication.

Chapter 5 was dedicated to a comprehensive experimental study of hot photoluminescence in silicon cavities in a larger size range, which highlights the applicability of this technique across various dimensions. Variable energy excitation photoluminescence measurements reveal the role of the electronic structure of silicon in determining the spectral range of the photoluminescence spectrum, while the individual peaks were demonstrated to depend on phonon modes. Finite Difference Time Domain simulations elucidate the role of cavity modes in determining the broad features in the photoluminescence spectrum and also reveal interesting electromagnetic properties germane to plasmonic cavities which host high order, whispering gallery-type modes. Finally, though resonant-Raman scattering and hot photoluminescence show similar spectral characteristics, temperature dependent photoluminescence spectroscopy presents clear evidence for a hot photoluminescence process, where the temperature dependence is opposite that of Stokes resonant-Raman scattering.

The lessons learned in previous chapters were then applied to a phenomenon that would benefit from highly enhanced light emission; optical cooling of semiconductors. Chapter 6 lays out the theoretical foundations of optical cooling of semiconductors based on literature review and examines each component separately with regards to optical cooling in CdS. The many difficulties, which prevent the widespread use of optical cooling in semiconductors, are highlighted here and surface plasmon enhanced cooling is proposed as a solution. The potential benefits of cooling via surface plasmon enhanced light emission are then posed in terms of both cavity electromagnetics (enhanced emission quantum yield) and solid-state physics i.e. enhanced electron-phonon coupling in plasmonically-coupled CdS, where experimental evidence is presented. Finally, we embark on the first experimental exploration, to the author's knowledge, of surface-plasmon enhanced optical cooling in semiconductors, where we demonstrate promising results and clearly outline subsequent steps for its optimization.

It is the author's hope that the investigations presented here serve to motivate the use of plasmonics in modern semiconductor technology, as plasmonics (i.e. photonics at the nanoscale) presents the potential for ever smaller and faster devices.[11] From the physics point of view, it is encouraging that the investigations performed here have sparked further avenues for research. In this case, the exploration of surface plasmon enhanced light emission reveals an interplay between charge carriers, phonons, and plasmons, where the exact luminescence mechanism, particularly in the case of Si, has yet to be determined. This opens the door for a significant amount of theoretical work,

which when combined with experiment, presents the opportunity for further scientific (and technological) endeavor.

References

1 Adachi, S. *Properties of Group-IV, III-V and II-VI Semiconductors*. (Wiley, 2005).

2 Naik, G. V., Shalaev, V. M. & Boltasseva, A. Alternative Plasmonic Materials: Beyond Gold and Silver. *Advanced Materials* **25**, 3264-3294, doi:Doi 10.1002/Adma.201205076 (2013).

3 Fleming, G. R. *Chemical applications of ultrafast spectroscopy*. (Oxford University Press, 1986).

4 Cho, C.-H., Aspetti, C. O., *et al.* Tailoring hot-exciton emission and lifetimes in semiconducting nanowires via whispering-gallery nanocavity plasmons. *Nat Mater* **10**, 669-675 (2011).

5 Cho, C.-H., Aspetti, C. O., Park, J. & Agarwal, R. Silicon coupled with plasmon nanocavities generates bright visible hot luminescence. *Nat Photon* **7**, 285-289 (2013).

6 Khurgin, J. B. Surface plasmon-assisted laser cooling of solids. *Physical Review Letters* **98**, doi:Doi 10.1103/Physrevlett.98.177401 (2007).

7 Oulton, R. F., Sorger, V. J., Genov, D. A., Pile, D. F. P. & Zhang, X. A hybrid plasmonic waveguide for subwavelength confinement and long-range propagation. *Nat Photon* **2**, 496-500 (2008).

8 Oulton, R. F. *et al.* Plasmon lasers at deep subwavelength scale. *Nature* **461**, 629-632 (2009).

9 Al-Harbi, T., Al-Hazmi, F. & Mahmoud, W. E. Synthesis and characterization of nanoporous silica film via non-surfactant template sol-gel technique. *Superlattice Microst* **52**, 643-647, doi:Doi 10.1016/J.Spmi.2012.06.025 (2012).

10 Anger, P., Bharadwaj, P. & Novotny, L. Enhancement and Quenching of Single-Molecule Fluorescence. *Physical Review Letters* **96** (2006).

11 Brongersma, M. L. & Shalaev, V. M. The Case for Plasmonics. *Science* **328**, 440-441, doi:10.1126/science.1186905 (2010).